

# Dissertation

submitted to

the Combined Faculties of the Natural Sciences and Mathematics  
of the Ruperto-Carola-University of Heidelberg, Germany,  
for the degree of Doctor of Natural Sciences

Put forward by

Stefan A. Brünner

born in Fürstenfeld, Austria

Oral examination on 05 July 2017



# **Mitigation of $^{222}\text{Rn}$ induced background in the XENON1T dark matter experiment**

Referees:

Prof. Dr. Dr. h.c. Manfred Lindner

Juniorprofessorin Dr. Loredana Gastaldo



### **Mitigation of $^{222}\text{Rn}$ induced background in the XENON1T dark matter experiment**

$^{222}\text{Rn}$  is a major source of background in many rare-event experiments such as the XENON1T dark matter search. The noble gas radon is created by radioactive decay inside all detector materials and emanates into the sensitive liquid xenon target disabling any detector shielding. Subsequent beta-decays of radon progenies are the dominant source of background in the XENON1T experiment. In order to mitigate radon induced background the detector's construction materials have been selected according to dedicated  $^{222}\text{Rn}$  emanation measurements. In the first part of this thesis, we summarize the results of the XENON1T radon screening campaign and present the measurement of the integral radon emanation rate of the fully assembled detector. The development of a radon removal system which continuously purifies the liquid xenon target from the emanated radon is the topic of the second part of this thesis. In order to demonstrate the suitability of cryogenic distillation as a technique to separate radon from xenon, we developed an experimental setup to measure the depletion of radon in xenon boil-off gas after a single distillation step. In the last part of the thesis, we demonstrate the operation of a radon removal system for the XENON100 experiment. For this first test employing a running dark matter detector, we integrated a multiple stage, cryogenic distillation column in the XENON100 gas purification loop. From the evolution of the radon concentration in XENON100, we investigate the distillation column's radon removal capability and discuss the design and application of a radon removal system for XENON1T and the upcoming XENONnT experiment.

**Reduktion des  $^{222}\text{Rn}$  induzierten Untergrundes im XENON1T Dunkle Materie Experiment.** Für viele Experimente auf der Suche nach seltenen Signal-Ereignissen stellt  $^{222}\text{Rn}$  eine entscheidende Quelle für Untergrund dar. Radon entsteht durch radioaktiven Zerfall in den Detektormaterialien und kann, begünstigt durch seine Eigenschaften als Edelgas, in das sensitive Flüssig-Xenon Target gelangen. Die nachfolgenden Beta-Zerfälle sind die Hauptursache für Untergrundereignisse in XENON1T. Um diese zu reduzieren, werden nur Materialien mit niedriger Radon-Emanations-Rate ausgewählt und für die Detektorkonstruktion verwendet. Im ersten Teil dieser Arbeit werden die Ergebnisse der XENON1T Emanationsmessungen zusammengefasst. Außerdem wird die integrale Emanationsrate des fertiggestellten Detektors gemessen und diskutiert. Inhalt des zweiten Teils ist die Demonstration eines Radon-Reinigung-Systems für flüssig Xenon Detektoren im laufenden Betrieb. Dabei soll in einem Reinigungskreislauf Radon mittels kryogener Destillation vom Xenon getrennt werden. Dazu wurde zunächst die Radonreduktion in Xenongas nach einer einfachen Destillationsstufe gemessen um diese Trennungsmethode auch bei niedrigsten Radonkonzentrationen nachzuweisen. Im letzten Teil der Arbeit, wird der Einsatz eines Radon-Reinigungs-System am laufenden XENON100 Detektor präsentiert. Dabei wurde eine mehrstufige Destillationssäule adaptiert und in die bestehende Gasreinigung des Detektors integriert. Aus der Evolution der Radon Konzentration in XENON100 wird das Trennvermögen der Destillationssäule bestimmt. Abschließend wird die Entwicklung und der Einsatz eines Radon-Reinigungs-Systems für XENON1T und den zukünftigen XENONnT Detektor diskutiert.

# Contents

<b>1. Direct dark matter detection with XENON</b>	<b>1</b>
1.1. The search for dark matter . . . . .	1
1.1.1. Evidences for dark matter . . . . .	2
1.1.2. Dark matter candidates . . . . .	4
1.1.3. Dark matter detection strategies . . . . .	5
1.1.4. Direct detection event rates and detection techniques . . . . .	6
1.1.5. Current status of dark matter direct detection . . . . .	8
1.2. The XENON dark matter experiments . . . . .	9
1.2.1. Principle of the XENON two-phase TPC . . . . .	9
1.2.2. The XENON100 detector . . . . .	11
1.2.3. The XENON1T detector . . . . .	17
<b>2. Radon mitigation in the XENON1T experiment</b>	<b>23</b>
2.1. Intrinsic $^{222}\text{Rn}$ background in XENON1T . . . . .	23
2.2. XENON1T radon screening campaign . . . . .	25
2.2.1. Screening procedure . . . . .	25
2.2.2. Emanation results . . . . .	26
2.3. Integral emanation measurement of the XENON1T detector . . . . .	28
2.3.1. Electrostatic collection radon monitors for $^{222}\text{Rn}$ detection . . . . .	28
2.3.2. Setup and measuring process . . . . .	36
2.3.3. Data analysis and results . . . . .	37
2.4. Concept of an on-line radon removal system for liquid xenon detectors . .	41
2.4.1. Impact of a radon removal system . . . . .	41
2.4.2. Radon-xenon separation techniques . . . . .	43
2.5. Summary and conclusions . . . . .	46
<b>3. Radon depletion in xenon boil-off gas</b>	<b>47</b>
3.1. The Heidelberg Xenon (HeXe) setup . . . . .	48
3.1.1. HeXe cryostat . . . . .	48
3.1.2. Gas system . . . . .	50

3.2. Process of measuring . . . . .	50
3.2.1. Preparation of radon enriched xenon . . . . .	51
3.2.2. Measurement of boil-off reduction . . . . .	52
3.3. Data analysis . . . . .	53
3.3.1. Dynamic reduction analysis . . . . .	54
3.3.2. Constant reduction fit . . . . .	56
3.4. Results boil-off reduction . . . . .	57
3.4.1. Static measurements . . . . .	58
3.4.2. Recuperation measurements . . . . .	61
3.4.3. Argon measurements . . . . .	69
3.5. On the vapor pressure of radon . . . . .	71
3.6. Summary and conclusions . . . . .	72
<b>4. Operation of a distillation based radon removal system at XENON100</b>	<b>75</b>
4.1. Data analysis . . . . .	76
4.1.1. Analysis using $\alpha$ -decays . . . . .	76
4.1.2. BiPo analysis . . . . .	79
4.1.3. $^{210}\text{Po}$ events in XENON100 . . . . .	81
4.2. Experimental setup . . . . .	84
4.3. Radon removal in XENON100 . . . . .	86
4.3.1. Overview of the distillation campaign . . . . .	87
4.3.2. Evolution of the $^{222}\text{Rn}$ activity concentration . . . . .	88
4.3.3. On the distribution of radon in XENON100 . . . . .	90
4.3.4. Radon contribution from ambient air . . . . .	93
4.4. The radon removal capability of the distillation column . . . . .	96
4.4.1. 2nd distillation run . . . . .	97
4.4.2. 1st distillation run . . . . .	100
4.5. Radon removal system for XENON1T . . . . .	101
4.6. Summary and conclusions . . . . .	106
<b>5. Summary and conclusions</b>	<b>107</b>
<b>Appendices</b>	<b>111</b>
<b>A. Gas analytics for radon monitor measurements</b>	<b>111</b>
<b>B. Derivation of the boil-off reduction factor from Raoult's law</b>	<b>112</b>
<b>Bibliography</b>	<b>115</b>
<b>List of Figures</b>	<b>123</b>
<b>List of Tables</b>	<b>125</b>



# Chapter 1

## Direct dark matter detection with XENON

The framework of this thesis is the quest for dark matter. Not being described by the Standard Model of Particle Physics, the identity and nature of dark matter is one of the biggest questions in modern particle physics.

We want to start this work by giving an introduction to the concept of dark matter. In section 1.1, we will discuss a selection of outstanding evidences which strengthened our picture of the existence of this additional, non-baryonic type of matter beyond standard physics and cosmology. Different theoretical models came up with a 'zoo' of possible dark matter candidates. In this introduction, we will only describe the most popular ones. After a short outline of the different dark matter detection strategies, we will focus on the XENON direct detection experiments in section 1.2. Both, the XENON100 and the XENON1T detectors are used in this work and a detailed description of their working principle and experimental setup is thus necessary.

We want to emphasize that this chapter shouldn't be understood as a comprehensive introduction to the field of dark matter research. For the interested reader, we want to refer to more detailed reviews, e.g., to [1], focusing on dark matter direct detection, or [2, 3] for a more general overview.

### 1.1. The search for dark matter

From several astrophysical and cosmological observations, we conclude that the majority of the gravitating matter in our Universe is assigned to dark matter: a non-luminous, non-baryonic type of matter beyond the Standard Model of Particle Physics. From the  $\Lambda$ CDM model<sup>1</sup>, the standard model of cosmology, we derive that cold (i.e., non relativistic) dark matter (CDM) is about five times more abundant than ordinary matter. In this section, we want to describe dark matter evidences and will introduce several particle candidates. Then, we will describe the experimental strategies in order to detect and describe its properties.

---

<sup>1</sup>This standard model of cosmology has the cosmological constant  $\Lambda$  and cold (i.e., non relativistic) dark matter (CDM) as its main constituents.  $\Lambda$  parameterizes the accelerated expansion of the Universe.

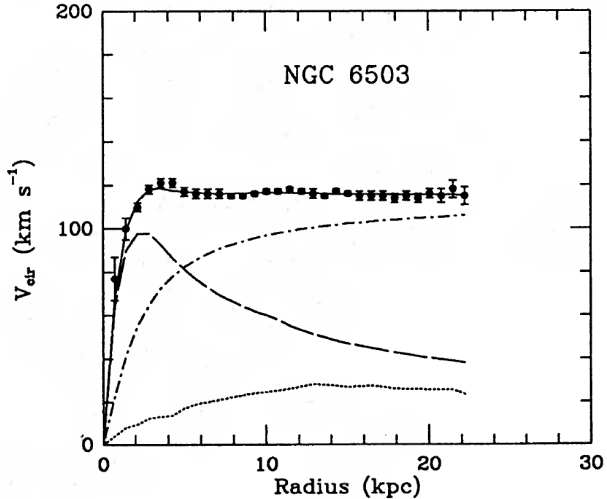


**Figure 1.1.:** Rotation curve of the spiral galaxy NGC 6503. The observed flat curve is decomposed into luminous matter (dashed curve), the dark halo (dash-dot curve) and the galactic gas (dotted curve). Figure taken from [5].

### 1.1.1. Evidences for dark matter

A strong argument pointing to dark matter being a particle, in contrast to modifications of the gravitation itself (see, e.g., MOND [4]), are the observational evidences found at all scales: from the galactic scale until the description of the structure of the entire universe.

A famous example for the evidence of dark matter in spiral galaxies comes from the observation of the rotation speed of stars around the galactic center, referred to as rotation curves. In [6], it was described for the first time that the majority of spiral galaxies have an approximately flat rotation curve at distances larger than  $r = 4$  kpc from the galactic center. As an example, the rotation curve of the galaxy NGC 6503 is shown in Figure 1.1 [5]. The linear increase of the velocity of the stars, referred to as  $v_{cir}$ , at low radii is expected from a Newtonian motion. The dashed curve describing the visible matter of the galaxy, shows then the expected decline of  $v_{cir} \propto r^{-1/2}$  at about  $r = 3$  kpc. In order to explain the observed flat behavior of  $v_{cir}$ , a dark halo (dash-dotted curve) is introduced, i.e., the galaxy is embedded in a halo of non-luminous dark matter.

Another observational evidence comes from gravitational lensing [7]. Light from far distant astronomical objects gets distorted when passing through a large gravitational potential caused, e.g., by galaxies or galaxy clusters. By measuring the deflection of the light, the total mass of the object causing the distortion can be determined. In Figure 1.2 (Left), the total mass of a galaxy, expressed by the shear-profile  $\Delta\Sigma$ , is decomposed into subcomponents [8]. While at low distances  $R$  the galactic center is dominated by baryonic mass, Figure 1.2 (Left) confirms our picture of galaxies being embedded in a dark matter halo (NFW profile) which dominates at larger distances. This is in agreement with earlier results discussed in [10].

Gravitational lensing is also used to study the collision of two galaxy clusters, e.g., the famous 'Bullet Cluster' [9]. The green contours in Figure 1.2 (Right) show the mass centers of two galaxy clusters obtained by means of gravitational lensing. The overlaid

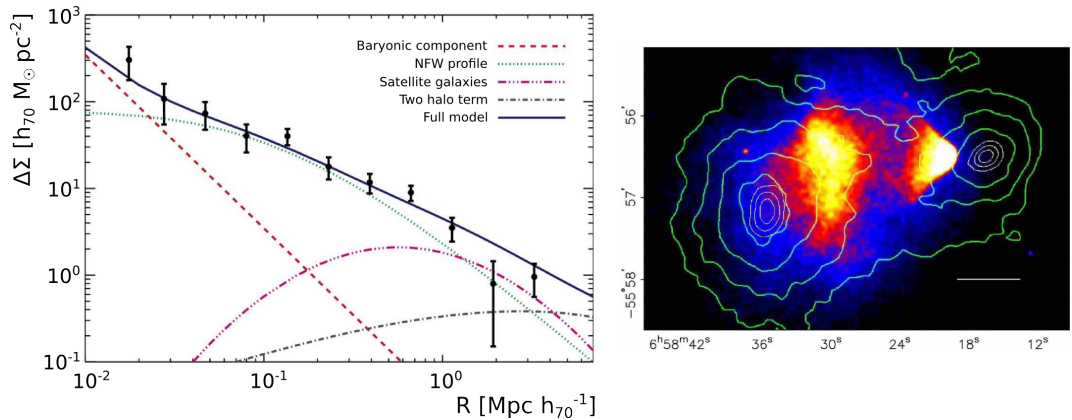


**Figure 1.2.:** (Left) Decomposition of the different shear profiles of an elliptical galaxy as a function of the distance from the galactic center [8]. The luminous matter (baryonic component) is embedded in a halo of dark matter (NFW profile). (Right) X-ray emission in the Bullet cluster (colored features) [9]. The green contours show the mass centers of the two colliding galaxy clusters clearly separated from the X-ray sources.

colored feature (from blue to red) is the X-ray emission originating from hot intergalactic gas clouds, which are clearly separated from the mass centers. This observation is explained by the fact that in both galaxy clusters dark matter contributes most to the total mass. During the collision process, the two dark matter mass centers could penetrate each other staying unaffected. This allows to set limits on the dark matter self-interaction cross-section [11, 12]. The intergalactical gas of the clusters, on the other hand, interacted strongly and was thus effectively slowed down. For a review of studying dark matter by means of gravitational lensing see, e.g., [13].

The last evidence we want to discuss comes from cosmology and the analysis of the Cosmic Microwave Background (CMB). Tiny temperature anisotropies at the level of hundreds of  $\mu\text{K}$  have been measured by the WMAP collaboration [14] and most recently by the Planck satellite [15]. In standard cosmology, these anisotropies arise from quantum fluctuations which magnified to macroscopic scales during the Universe's inflation epoch (see, e.g., [17]). They gave rise to matter density perturbations and eventually to structure formation. The temperature fluctuations in the CMB, shown in Figure 1.3 (Left), correspond to the matter density distribution  $\sim 400\,000$  years after the Big Bang, at the time when the Universe became transparent for optical photons. For analysis, the averaged temperature difference between two points on the sphere is determined as a function of their angular distance. The result is shown, expanded in spherical harmonics, as the power spectrum in Figure 1.3 (Right) as obtained by the Planck collaboration [15]. Small values of the multipole moment  $l$  translate to large angular distances. The characteristic acoustic peaks in the power spectrum are described within the six-parameters  $\Lambda\text{CDM}$  model which allows us to fit the densities of dark matter ( $\Omega_{DM}$ ), baryonic matter ( $\Omega_b$ ) and dark energy ( $\Omega_\Lambda$ ). As quoted in the most recent analysis of the CMB (data

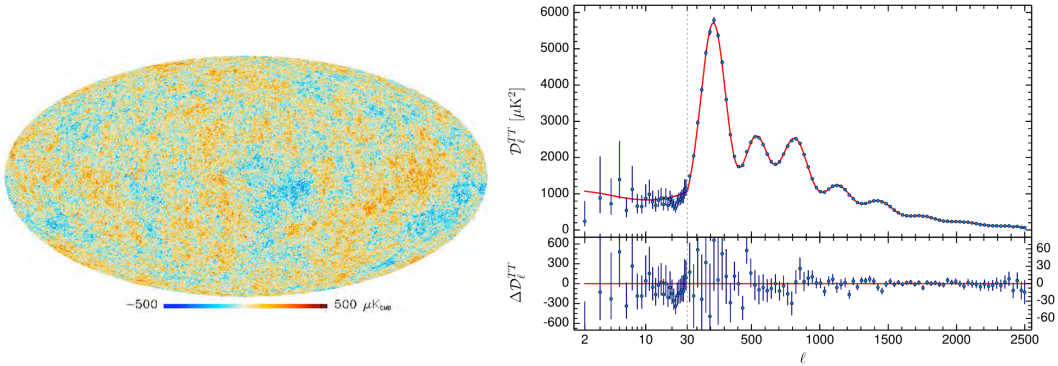


**Figure 1.3.:** (Left) Temperature fluctuations as found by the Planck satellite [16]. (Right) The temperature anisotropies are analyzed as a function of angular distance. Expressed by spherical harmonics this gives a power spectrum which can be fit by the  $\Lambda$ CDM model. Figure taken from [15].

from Planck 2015 [15]), the total energy density of our Universe is decomposed as:

$$\Omega_{DM} = 0.265 \quad \Omega_b = 0.049 \quad \Omega_\Lambda = 0.686 \quad .$$

Thus, the Standard Model of Particle Physics describes only about 5% of our Universe while the rest is assigned to the so-called dark sector. This picture is supported by results coming from Big-Bang nucleosynthesis (BBN) which constrains the baryon density to about  $\Omega_b = 0.04$  [18], in agreement with the  $\Lambda$ CDM model.

### 1.1.2. Dark matter candidates

Motivated by the astronomical and cosmological evidences, a particle nature of dark matter is favored. We can, however, set further constraints for this new type of particle (or particles). N-body simulations of the galaxy structure formation require massive, non-relativistic dark matter [19]. From the analysis of the CMB and from BBN, we know that the vast majority of dark matter needs to be non-baryonic. Objects like neutron stars, black holes or brown dwarfs are dark matter candidates but baryonic. Furthermore, extensive searches by means of gravitational lensing showed that on galactic scales this so-called massive halo objects (MACHOS) are ruled out at 95% confidence level to make up for the galaxy's entire dark matter content [20]. Since we observe the gravitational effects of dark matter from the early Universe on until today, a dark matter candidate needs to be stable, or, if unstable, its lifetime must be long with respect to the age of the Universe. Finally, the self-interaction of a dark matter candidate needs to be, if at all, very weak (see remarks concerning the Bullet Cluster). This is true also for electromagnetic interactions of dark matter with so-called standard model particles (i.e., particles described by the Standard Model of Particle Physics).

Several extensions of the Standard Model of Particle Physics, addressed to different physical problems, naturally provide a dark matter candidate. Examples are axions,

originating from the solution of the so-called strong CP-problem [21], or sterile neutrinos, introduced to explain the smallness of neutrino masses [22]. Another dark matter candidate are so-called weakly interacting massive particles (WIMPs). This general term categorizes massive particles which additionally interact via the weak interaction. Possible candidates arise again from extensions of the Standard Model of Particle Physics like the neutralino, i.e., the lightest supersymmetric particle [23], or the lightest Kaluza particle [24].

The thermal freeze-out is a standard production mechanism for WIMPs [25]. In the early Universe, dark matter is considered to be in thermal equilibrium with the thermal plasma, i.e., the creation and annihilation processes of WIMPs were equally efficient. As the Universe expanded, the plasma cooled down making the WIMP creation process less likely (Boltzmann suppression). On the other hand, the expanding Universe caused a dilution of the particle density which causes a suppression of the annihilation process. At the moment when the annihilation rate became smaller than the expansion rate, annihilation stopped and the WIMP-density was frozen to its relic density [23, 25]

$$\Omega_{DM} \approx \frac{3 \cdot 10^{-27} \text{ cm}^3 \text{s}^{-1}}{\langle \sigma_{ann} \cdot v \rangle \cdot h^2} . \quad (1.1)$$

Thereby,  $\langle \sigma_{ann} \cdot v \rangle$  is the thermal averaged annihilation cross-section before the freeze-out and  $h^2$  the dimensionless Hubble parameter. It is a remarkable coincidence that the relic density in Eq. (1.1) is consistent with the constraints from, e.g., the CMB if one considers a cross-section of the order of the weak interaction scale. In the following, we will consider dark matter to be described as a WIMP.

### 1.1.3. Dark matter detection strategies

We distinguish three general dark matter detection strategies according to the coupling of WIMPs to ordinary matter. Indirect dark matter detection refers to the annihilation of WIMPs into standard model particles. Experiments following this detection strategy are typically looking for  $\gamma$ -rays, neutrinos or anti-particles (e.g., positrons) produced in the annihilation process. A compendious review for indirect dark matter detection can be found in [26].

Another strategy is the dark matter production in the collision of standard model particles in accelerators like the Large Hadron Collider (LHC). Since WIMPs are considered to be stable and having a very small cross-section, they will most likely escape the accelerator without interaction. Thus, their presence must be reconstructed via missing energy and momentum (see, e.g., [27]).

The third detection strategy is the so-called direct detection. The goal is the direct proof of the scattering process of a WIMP particle off ordinary matter, e.g., an atomic nucleus. Since this thesis has been written in the framework of direct dark matter detection, we will have a closer look into different direct detection techniques.

#### 1.1.4. Direct detection event rates and detection techniques

The most important quantity in direct dark matter detection is the differential event rate, describing the WIMP-nuclei scattering rate per transferred nuclear recoil energy  $E$ . It is given by [28]

$$\frac{dR}{dE}(E, t) = N_N \frac{\rho_\chi}{m_\chi} \int_{v_{min}} \frac{d\sigma}{dE}(v, E) v f(v, t) dv . \quad (1.2)$$

Equation 1.2 points out the dependencies of the event rate on both WIMP-physics and detector properties. The parameter  $N_N$  is the number of target nuclei and is thus depending on the size of the detector. The ratio of the averaged local<sup>2</sup> WIMP density,  $\rho_\chi = (0.39 \pm 0.03) \text{ GeV/cm}^3$  [29], and the WIMP-mass  $m_\chi$  (model dependent), gives the dark matter number density. Another model dependent quantity is the WIMP velocity distribution  $f(v, t)$ . For the event rate, we integrate over all velocities, starting from the experiment's lowest detectable velocity  $v_{min}$  given a certain differential WIMP-nuclei interaction cross-section  $d\sigma/dE$ . For the latter, one can write

$$\frac{d\sigma}{dE} \propto \underbrace{\sigma_0^{SI} \cdot F_{SI}^2(E)}_{\propto \sigma_{SI}(E)} + \underbrace{\sigma_0^{SD} \cdot F_{SD}^2(E)}_{\propto \sigma_{SD}(E)} , \quad (1.3)$$

i.e., the cross-section is proportional to the sum of spin-independent (SI) and spin-dependent (SD) contributions. The parameters  $\sigma_0$  and  $F(E)$  in Eq. (1.3) refer to the WIMP-nuclei cross-sections at zero momentum transfer and the form factors, respectively. Thus, direct detection experiments are in principle able to probe both SI and SD cross-sections. For the SI cross-section at zero momentum transfer we find

$$\sigma_0^{SI} \propto (Z \cdot f^p + (A - Z) \cdot f^n)^2 , \quad (1.4)$$

where  $Z$  and  $A$  are respectively the atomic number and the mass number of the target nucleus and  $f^{p,n}$  are the SI WIMP-proton and WIMP-neutron couplings. The assumption  $f^p = f^n$  is commonly used, which shows, inserted in relation 1.4, a cross-section proportional to  $A^2$  of the target nucleus. Therefore, many direct detection experiments prefer target atoms with a high atomic mass such as xenon or germanium.

In the spin-dependent case, the cross-section in the limit of zero momentum transfer depends on the nucleus' total spin content  $J$  [23]

$$\sigma_0^{SD} \propto \frac{(J+1)}{J} \cdot [a_p \langle S_p \rangle + a_n \langle S_n \rangle] . \quad (1.5)$$

Therein, we split the cross-section into the contribution of protons and neutrons.  $\langle S_{p,n} \rangle$  is the corresponding expectation value of the spin content of protons and neutrons in the nucleus. The effective WIMP-proton and WIMP-neutron couplings are referred to as  $a_{p,n}$ . Since natural xenon contains the isotopes  $^{129}\text{Xe}$  (26% abundance) and  $^{131}\text{Xe}$

---

<sup>2</sup>Local means: at any point one solar-distance away from our galactic center.

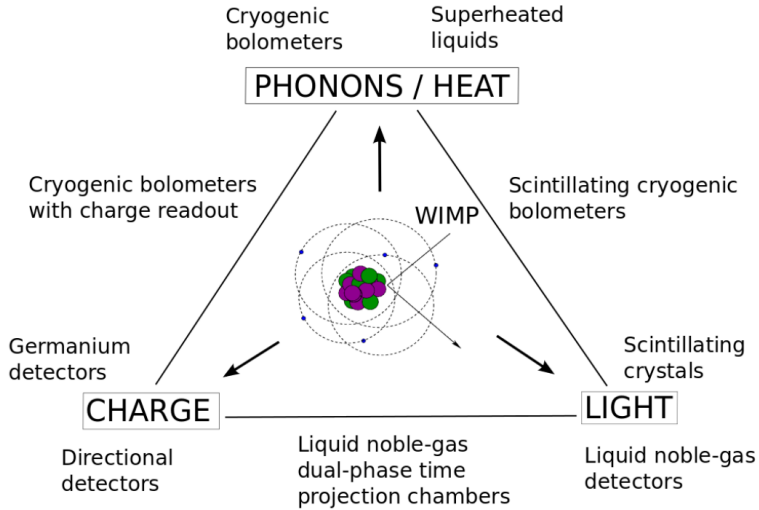


**Figure 1.4.:** Detection strategies used in direct detection experiments. Figure taken from [1].

(21% abundance), both nuclei are having a non-zero spin, the XENON experiments are also sensitive to SD WIMP interactions.

Typical differential event rates for current experiments are in the range of  $10^{-6}$  to  $10^{-4}$  events/(kg · d · keV), depending on their target nuclei (see, e.g., figure 2 in [1]). The crucial task in direct detection is to transform the rare and in general low energetic WIMP interaction events into a measurable detector signal. In Figure 1.4, the different detection strategies in use are sketched [1]. The energy transferred in the WIMP-nucleus scatter can be transformed into heat (e.g., phonon excitation in a crystal), a charge signal (e.g., ionization of the target nuclei) or scintillation light (e.g., noble gas scintillation). Current direct detection experiments make use of one or at most two of this signal channels according to the properties of their target material. In liquid noble gas dual-phase time projection chambers, for example, the recoil energy is transformed into scintillation light but also into a charge signal which are both used for WIMP detection. Since the XENON detectors are of this type, we will introduce the underlying detection strategy in section 1.2. For a more detailed discussion of experiments looking for other signal channels, we want to refer again to [1].

In order to identify a dark matter signal, direct detection experiments usually define some quality criteria a WIMP event needs to fulfill<sup>3</sup>. Then, an excess is searched for in the event rate above the background. The bare detection signal is in itself independent from any dark matter models. However, in order to conclude on WIMP properties such as its mass and cross-section, we need to assume for example a certain local dark matter density and velocity distribution (see Eq. (1.2)) but also an interaction model (e.g., SI or

<sup>3</sup>One example is the single scatter criteria. The WIMP-nucleus cross-section is so low that a single WIMP can scatter only once when penetrating the detector. So-called multiple scatter events are thus rejected.

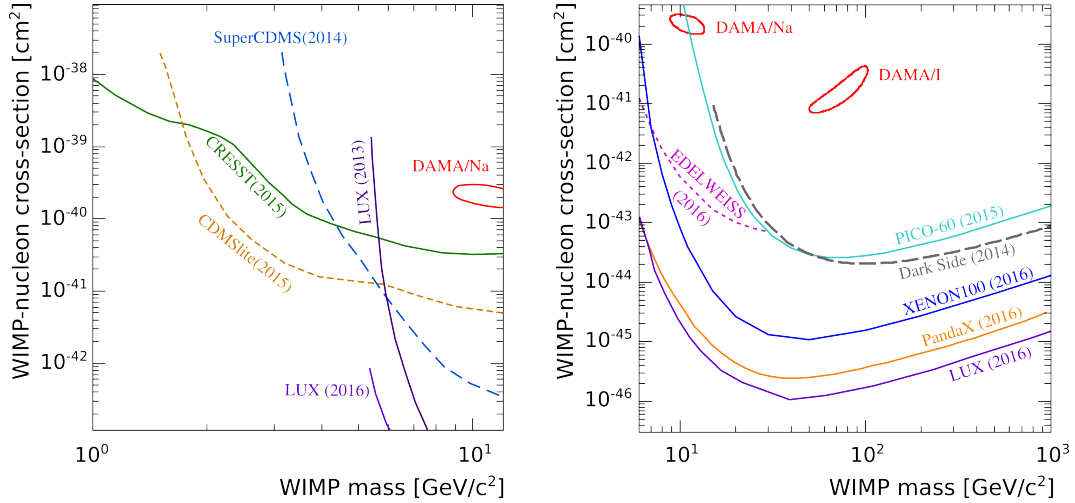


**Figure 1.5.:** Status of direct dark matter detection searches assuming a spin-independent (SI) WIMP-nucleon cross-section. The left and the right figures show recently published exclusion limits of different experiments for low and high WIMP masses, respectively. The red circles mark the dark matter signal claimed by the DAMA collaboration [33].

SD). Some experiments make also use of a predicted annual modulation of the WIMP-nucleus interaction rate. Due to the movement of the Earth around the Sun, the relative WIMP velocity and consequently also the event rate is expected to oscillate, having its maximum at the beginning of June and its minimum in December [30]. Direct detection experiments can thus also look for this specific rate modulation in their detector signals.

### 1.1.5. Current status of dark matter direct detection

For an outline of the status of WIMP direct detection, we selected in Figure 1.5 the most recent spin-independent (SI) results from different experiments. For convenience, we plot the low mass regime (left panel) separately from high WIMP masses (right panel). In order to conclude on the SI WIMP-nucleon cross-section the local dark matter density is set to  $\rho_\chi = 0.3 \text{ GeV/cm}^3$  [31] and we assume a standard Maxwellian velocity distribution  $f(v)$  (see Eq. (1.2)). Furthermore, we assume a pure SI interaction and use the Helm form factor [32] in Eq. (1.3).

Most of the experiments only published limits for the SI WIMP-nucleus cross-section, excluding the parameter space above their individual exclusion curves. Thus, these experiments did not detect a conclusive signal yet. At lowest masses, the most stringent limit is quoted by the CRESST-II collaboration [34], which operates a detector based on CaWO<sub>4</sub> single crystals cooled down to mK temperatures. The latest published limit from the CDMS Low Ionization Threshold Experiment (CDMSlite) [35], using cryogenic germanium detectors, is the lowest for WIMP masses between 2 to 5 GeV/c<sup>2</sup>. In the broad high mass regime in Figure 1.5 (Right), mainly detectors based on liquid xenon dual-phase time projection chambers dominate. The most stringent exclusion limit is currently quoted by the LUX collaboration [36] followed by the PandaX experiment [37]

and the XENON100 experiment [38].

The red circles in Figure 1.5 (Right) are claims for a dark matter signal by the DAMA collaboration. They have published the detection of an annual modulation signal with a significance of  $9.3\sigma$  [33]. The DAMA detector is based on NaI(Tl) crystal scintillators. Depending on the target nucleus (Na or I), the signal is transferred into a specific signal-region in the parameter space shown in Figure 1.5 (Right). The dark matter claim published by DAMA is in tension with many other direct detection experiments such as LUX and XENON100 as they didn't detect a WIMP signal above their background even though reaching a higher sensitivity. A dedicated analysis looking for an annual modulation signal in four years of XENON100 data excludes the DAMA signal with a  $5.7\sigma$  significance [39].

## 1.2. The XENON dark matter experiments

The XENON dark matter experiments are examples for direct detection experiments using liquid xenon dual-phase time projection chambers (see section 1.2.1). In 2006, the XENON collaboration started the XENON10 detector, which employed a liquid xenon target of about 10 kg to search for elastic WIMP-nucleus scattering events [40]. The successor experiment, the XENON100 detector [41], started taking science data in 2009. It was operated with an increased liquid xenon mass of about 160 kg, and enabled to set the most stringent limits for SI and SD WIMP-nucleon cross-sections at that time [38]. The last science run of XENON100 ended in January 2014. Then, the detector was used for research and development activities for the next detector generation. Similar as its precursors, the XENON1T [42] experiment is located in the underground facilities of the INFN Laboratori Nazionali del Gran Sasso (LNGS) and is currently taking science data since end of 2016. It employs a total liquid xenon mass of 3.5 t and aims at increasing the sensitivity of current direct detection experiments by an order of magnitude. The research presented in this thesis has been done in the framework of the XENON100 and the XENON1T experiments. Thus, we want to introduce both detectors and their setups in more detail, starting with an introduction to dual-phase time projection chambers, the principle all XENON detectors are based on.

### 1.2.1. Principle of the XENON two-phase TPC

The dual-phase time projection chamber (TPC) as it is used in the XENON experiments is of cylindrical shape and contains the sensitive liquid xenon target. As indicated in Figure 1.6, the TPC houses also a gaseous xenon volume at the top (hence dual-phase). Light sensors, so-called photo-multiplier tubes (PMTs), are arranged in arrays covering most of the TPC's upper and lower surface. While the bottom PMT array is immersed in liquid xenon (LXe), the top PMT's are surrounded by xenon gas (GXe). In case of a WIMP scatter off a nucleus in the liquid target, the transferred energy results in the excitation ( $\text{Xe}^*$ ) and ionization ( $\text{Xe}^+$ ) of xenon atoms. As described in [43], the exciton

## 1. Direct dark matter detection with XENON

---

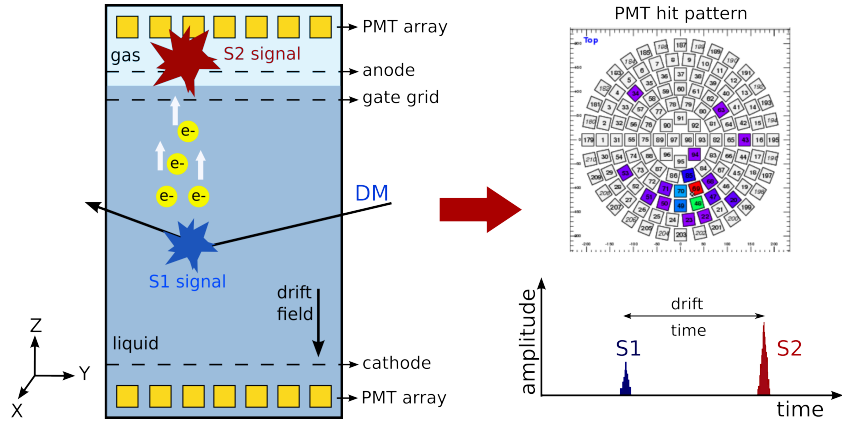


**Figure 1.6.:** Working principle of a liquid xenon dual-phase time projection chamber (TPC). (Left) Interaction energy is transformed into direct scintillation light (S1) and free electrons due to ionization. The latter are drifted upwards and produce a secondary scintillation light (S2) after extraction into the gas phase. (Right) From the PMT hit pattern the X/Y-position of the interaction is reconstructed. The drift-time of the electrons is determined from the time window between the S1 and S2 signals and proportional to the Z-coordinate of the event.

$\text{Xe}^*$  goes back to the ground level via



where  $\text{Xe}_2^*$  is an excited dimer and  $h\nu$  the energy released as vacuum ultraviolet (VUV) scintillation light with a mean wavelength of 178 nm. The ionized xenon atoms also cause scintillation via recombination with an electron [43]:



Then, the single exciton  $\text{Xe}^*$  continues as shown in Eq. (1.6). The scintillation light originating from excitation and recombination of ionized xenon is referred to the prompt scintillation light S1. It is immediately detected by the PMTs (due to light reflection at the liquid-gas interface mostly by the bottom PMTs).

An electric drift field, applied between the cathode and a gate grid, ensures that not all electrons recombine. Instead, a fraction is drifted towards the liquid xenon surface. Another stronger field (between gate grid and anode) extracts the drifted electrons into the gas phase. In this process, a second proportional scintillation signal, referred to as S2, is produced by means of electroluminescence [44]. Due to the homogeneous drift fields, the X/Y-position of the WIMP interaction inside the TPC can be reconstructed from the hit pattern detected by the top PMT array for the corresponding S2 signal. An example from the XENON100 detector is shown in Figure 1.6 at the top right. While the

S1 signal is produced promptly, it takes some time until the electrons have been drifted to the top of the TPC. Thus, the time difference between the S1 and the S2 signals gives access to the depth (i.e., the Z-coordinate) of an event assuming a constant electron drift velocity. Combining both the PMT hit pattern and the electron drift time, we obtain a 3D position reconstruction of any interaction inside the TPC. As we will point out in the following section, this enables us to fiducialize, i.e., to use only the innermost part of the TPC for the WIMP search. Events happening at the edges are usually rejected as they are most likely induced by radioactive decays in the detector materials.

### 1.2.2. The XENON100 detector

The XENON100 detector is described in details in [41, 45]. Here, we will thus focus on (technical) aspects which are important for our research results presented in the following chapters. A short introduction to data analysis and a summary of scientific results is given at the end of this section.

#### Cryostat, TPC and detector shielding

The XENON100 experiment is located in the Laboratori Nazionali del Gran Sasso (LNGS) underground laboratory in Italy. Shielded by about 1400 m of rock overburden (i.e., 3700 m water equivalent) it provides an effective protection from cosmic rays. The vertical muon intensity, e.g., is reduced by about 6 orders of magnitude with respect to the surface [46].

The cryostat is a cylindrical, vacuum insulated stainless steel vessel having a diameter of about 40 cm and a height of about 80 cm. It houses the total 160 kg liquid xenon target including the TPC. As shown in Figure 1.7 (Right), the cryostat is surrounded by different layers of passive shielding materials. The first layer of water and hydrogen-rich polyethylene (PE) stops neutrons which mostly originate from muon interactions in the rock or other surrounding materials. Then, two layers of lead and low radioactivity lead ( $^{210}\text{Pb}$  depleted) shield environmental radiation. The inner most layer is built up by PE and a high purity copper cavity which houses the cryostat. It is permanently flushed with boil-off nitrogen gas in order to mitigate  $^{222}\text{Rn}$  from ambient air.

A detailed drawing of the cryostat containing the TPC is shown in Figure 1.7 (Left). It has been built according to a diving bell design. The entire TPC, centered in the cryostat, is immersed in LXe. It separates the LXe reservoir into the active volume, i.e., the LXe enclosed by the TPC, and the surrounding so called active veto. During operation, gaseous xenon coming from the gas purification loop (described later in this section), is flushed into the diving bell. As a consequence, the LXe surface is pushed downwards and the gaseous xenon phase arises, needed for the operation of the TPC. In order to keep the liquid level constant, a so-called bleeding tube (see Figure 1.8) releases pressure into the LXe active veto. The bleeding tube can be moved vertically and was meant to adjust the liquid level, allowing for some independence from the amount of gaseous xenon pushed into the diving bell. Nevertheless, the liquid level in XENON100 was found to change with the circulation flow through the gas purification loop.

## 1. Direct dark matter detection with XENON

---

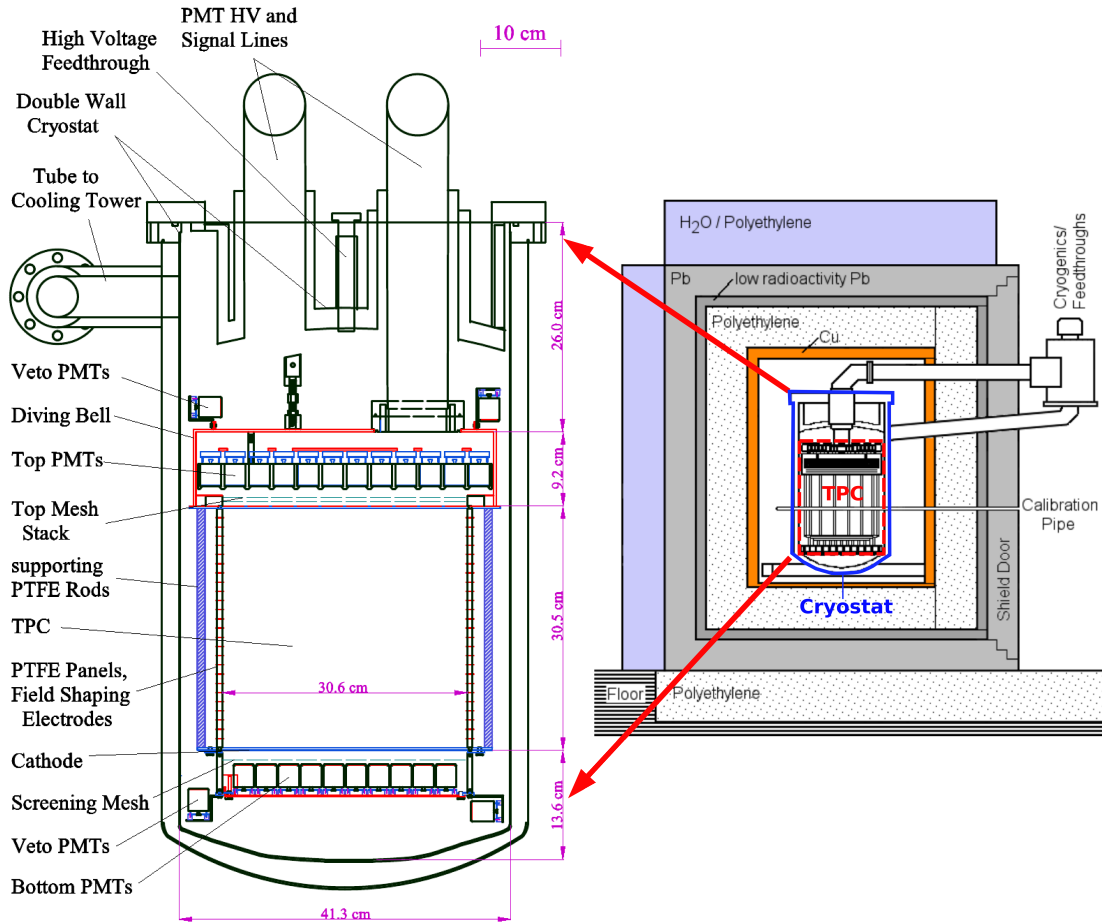


**Figure 1.7.:** (Left) Technical drawing of the XENON100 TPC pointing out important parts which are described in the text. (Right) The XENON100 detector is shielded by layers of water, lead and polyethylene. Figures taken from [41] and modified.

The housing of the TPC is made out of interlocking polytetrafluorethylen (PTFE, teflon) panels which are directly connected to the diving bell. Teflon has been selected since it is radio-pure and a good reflector of the scintillation light [47]. The housing is opaque, but LXe is exchanged between the TPC and the active veto region. In order to guarantee a homogeneous drift field, the PTFE panels are interspersed with field-shaping electrodes made out of copper. The drift field is created between the cathode, usually at  $-16\text{ kV}$ , and a grounded mesh at the top of the TPC (the lowest mesh out of three in the 'Top Mesh Stack' in Figure 1.7). For the extraction of the drifted electrons into the gas phase, a potential of usually  $4.5\text{ kV}$  is applied between the anode and a grounded gate mesh (the middle and top mesh in the 'Top Mesh Stack' in Figure 1.7, respectively).

The top PMT array in the gas phase consists of 98 sensors, arranged in concentric circles. They cover 43.9% of the TPC cross-section area [41]. The bottom array is located below the cathode and includes 80 PMTs. Here, the coverage is 52%. Both PMT arrays are protected from the electric fields (drift and extraction fields) by grounded screening meshes. The active veto is equipped with 64 additional so-called veto PMTs which are observing events that happen in the LXe surrounding the TPC. Penetrating radiation has a high probability to interact in the veto region first before it enters the TPC. Thus, signals which happened simultaneously with events detected in the veto region are rejected for the WIMP analysis. The HV supply and the signal cables of all PMTs are guided through two pipes and electrical feedthroughs to the outside of the cryostat and the shielding. The analog PMT signals are amplified and then individually digitized by means of VME Flash ADCs (analog-digital converters) [41].

### Gas purification and cryogenic system

Electronegative impurities, e.g., oxygen or water, reduce the average electron-lifetime in the LXe target. Thus, in order to drift electrons towards the LXe surface and eventually produce S2 signals, a high xenon purity is required [48]. Due to the permanent outgassing of those impurities from detector materials, a continuous purification of the LXe target is required. As shown in Figure 1.8 (Left), xenon is therefore extracted from the active veto region (green pipe). It evaporates and is recirculated through a purification loop sketched in Figure 1.8 (Right). The recirculation flow, usually 5.0 standard liters per minute (slpm), is driven by a gas recirculation pump (KNF double diaphragm pump) located after a buffer volume. A mass flow controller (MFC) guarantees a stable xenon flow. The central element of the purification loop is the high temperature zirconium getter which chemically binds electronegative impurities. As mentioned before, the clean xenon gas is then pushed back into the diving bell in order to achieve the TPC's xenon gas phase. The heat input of the circulated gas needs to be compensated by the cryogenic system displayed in Figure 1.8 (Left). It consists of a pulse tube refrigerator (PTR) providing a cooling power of about  $200\text{ W}$  at  $170\text{ K}$  and is driven by a helium compressor. The PTR is connected to a copper block which is in contact with the detector's boil-off xenon and acts as a cold finger, i.e., xenon gets liquefied at the copper block. The so-called heater is inserted between the PTR and the cold finger. It is also made out of copper and equipped with temperature sensors and electrical heaters. The latter are used to

## 1. Direct dark matter detection with XENON

---

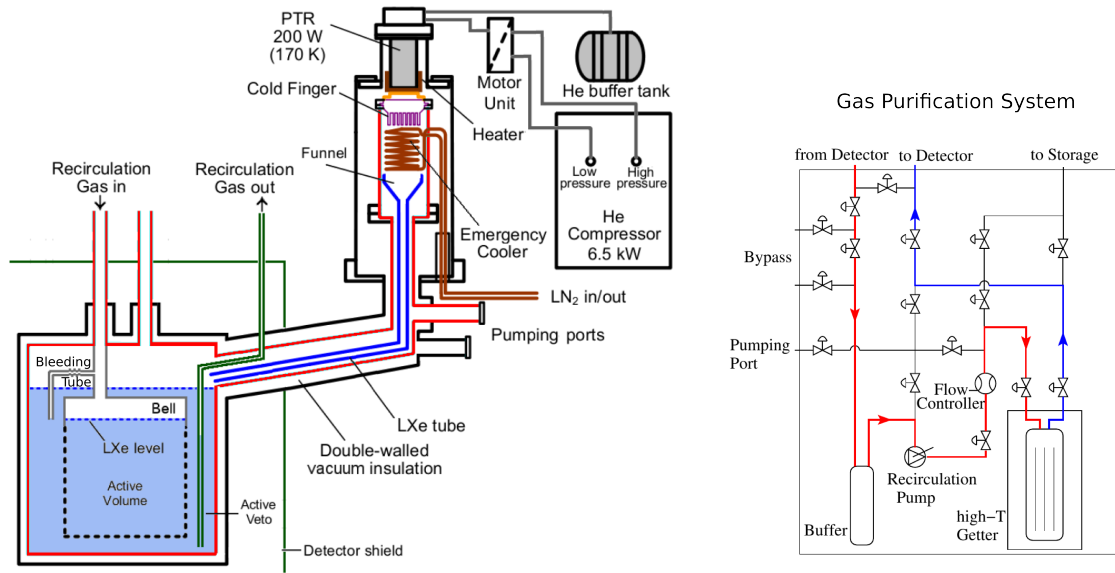


**Figure 1.8.:** (Left) The cryogenic system of the XENON100 experiment. (Right) Schematics of the gas purification system. Figures taken from [41].

partially compensate the PTR's cooling power and to adjust a stable temperature at the cold finger. After liquefaction, the xenon drops are collected by a funnel. Since the cryogenic system is installed outside the detector shielding, a LXe tube guides the xenon back into the detector.

### Data analysis and scientific results

In this section we want to give a simplified outline of the dark matter analysis used in XENON100. The interested reader is referred to [49] for a detailed discussion of the analysis methods.

A precise knowledge of the detector's response to WIMP signals but also to background events is essential. As will be discussed in chapter 2, most of the background is due to electronic recoils (ER). This event category refers to interactions with the electron shell of the xenon atoms and are typically induced by  $\beta$ - and  $\gamma$ -radiation. In order to study the detector's response to ERs,  $^{137}\text{Cs}$ ,  $^{57}\text{Co}$ ,  $^{60}\text{Co}$  and  $^{232}\text{Th}$  calibration sources are used. By means of a calibration pipe, shown in Figure 1.7 (Right), these sources are brought through the shielding close to the detector. WIMPs are not electromagnetically active and are thus expected to interact via nuclear-recoils (NR). For calibration, WIMP signals are mimicked using neutron calibration sources such as a  $^{214}\text{AmBe}$  ( $\alpha, n$ ) source. Calibration data of both ER and NR events, is shown in Figure 1.9 (Left). There, the parameter<sup>4</sup>  $\log_{10}(S_{2b}/S_1)$  is shown as a function of the transferred energy quantified by the S1 signal strength in photo-electrons (PE). The conversion from PE into keV is

<sup>4</sup>The subscript 'b' in  $\log_{10}(S_{2b}/S_1)$  indicates that only the light detected by the bottom PMT array was used for the S2-signal.

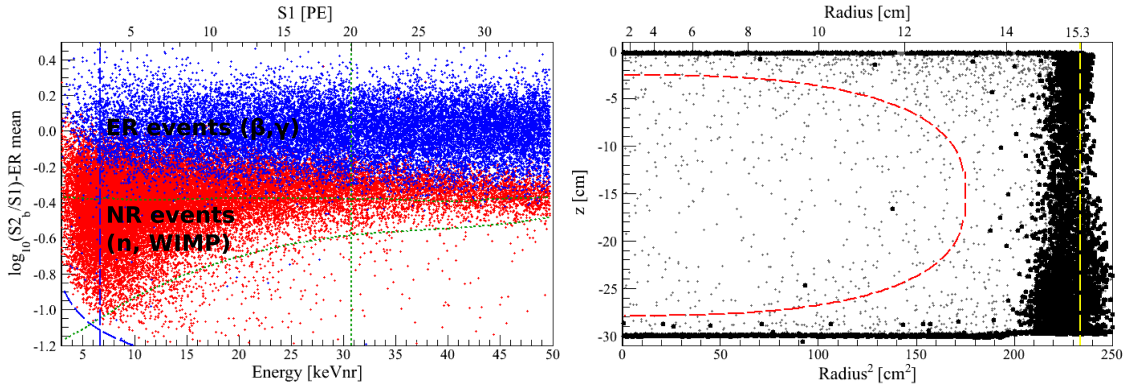


**Figure 1.9.:** (Left) Separation of electronic recoil (ER) events and nuclear recoil (NR) events in the discrimination parameter  $\log_{10}(S2_b/S1)$ . Figure courtesy of the XENON collaboration. (Right) Events happen at the edges of the TPC (dashed yellow line) are most likely background. Therefore, only interactions in the fiducial volume (dashed red line) are taken for analysis. Figure taken from [50].

discussed in [49], and depends also on detector parameters such as the light-yield  $L_y$  (for S1 conversion) and the charge-yield  $L_q$  (for S2 conversion). We observe that the S2/S1 ratio is different for NR and ER events. The latter are distributed in a band (ER-band) at significantly higher values of  $\log_{10}(S2_b/S1)$ . For the analysis, we define a benchmark region for WIMP search confined by the green and blue lines in Figure 1.9 (Left). The horizontal line (green dotted) is chosen to reject 99.75% of the ER recoils while minimizing at the same time the losses in the acceptance for NR events. The limit band towards low  $\log_{10}(S2_b/S1)$  values (green dotted) is here given by the 97% quantile of the NR event distribution. The vertical blue and green lines restrict the benchmark region to recoil energies corresponding to  $(6.6 - 30.5) \text{ keV}_{nr}$ . In the so-called *cut-based analysis*, we blind the benchmark region in our data during the time of data taking. From calibration data, we define certain criteria (quality cuts) which need to be fulfilled by a dark matter candidate event. One example is the so-called single scatter requirement. It demands that a dark matter candidate should scatter only once inside the detector in contrast to, e.g., gammas which likely undergo multiple scatters when penetrating the liquid xenon. Another requirement is that the events should happen in the so-called fiducial volume used for the analysis. Figure 1.9 (Right) shows the distribution of events inside the XENON100 TPC. Only the big dots fulfill the single scatter requirement and are thus used for our dark matter analysis. One can see that those events are accumulated at the TPC's walls (dashed yellow line), as well as at the liquid surface ( $Z = 0 \text{ cm}$ ) and at the bottom of the TPC ( $Z = -30 \text{ cm}$ ). We identify them as background events originating mostly from radioactive decays happen in the detector materials. The inner part of the TPC, on the other hand, is protected due to the self-shielding properties of liquid xenon. Therefore, only a fiducial volume (dashed red line) is used for dark matter analysis. Based on our background model, our quality cuts and our calibration data, we have an expectation for the number of events in the region of interest at the end of a science

## 1. Direct dark matter detection with XENON

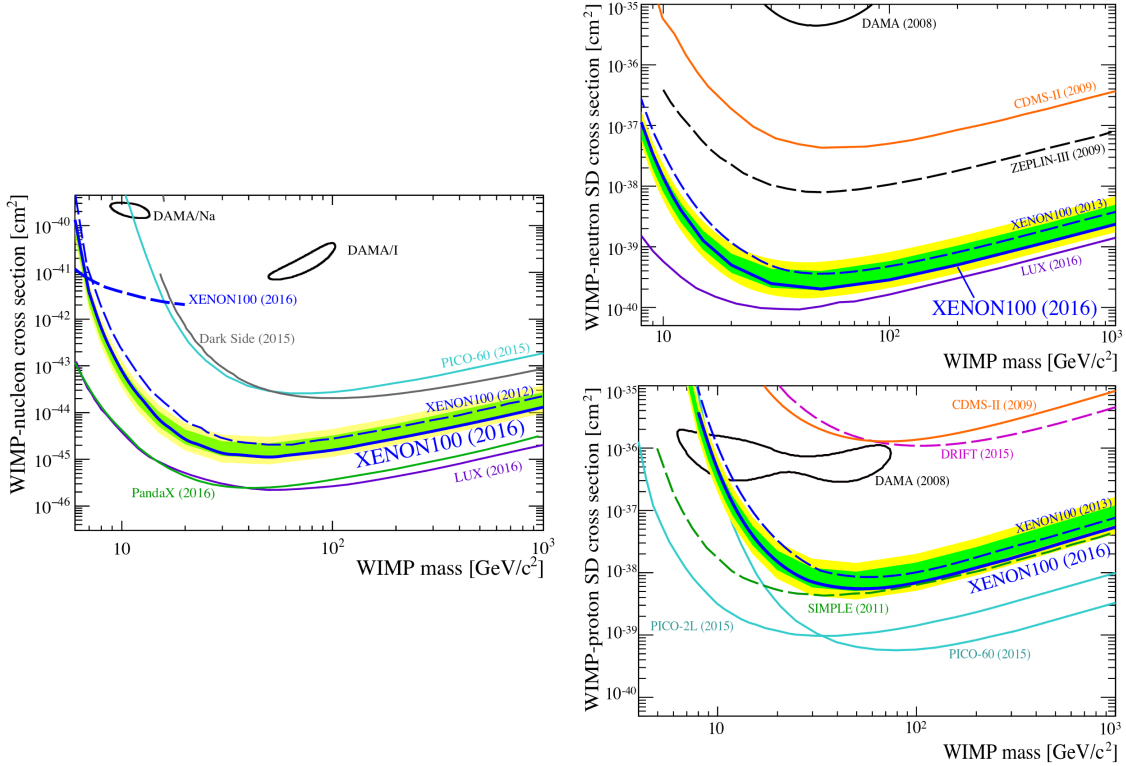


**Figure 1.10.:** (Left) Exclusion limit for the SI WIMP-nucleon cross-section. (Right) XENON100 results for the SD cross-section of WIMP-neutron (top) and WIMP-proton (bottom) interaction. Figures taken from [38].

run. A significant excess of events above the expectation would be interpreted as a dark matter signal. In parallel, we perform a profile likelihood (PL) analysis of our data [49]. The XENON100 collaboration published three science runs covering in total 477 live days of dark matter search. The combined result of all runs has been published in [38]. The exclusion limit for the spin-independent WIMP-nucleon cross sections as a function of the WIMP mass is shown in Figure 1.10 (Left). Already in section 1.1.5 we discussed this result and its tension with the dark matter claim published by DAMA. Figure 1.10 (Right) shows the status for spin-dependent WIMP-nucleon interactions. As we introduced in Eq. (1.5), it is common to distinguish between the proton and neutron contribution. The plot at the top gives the obtained exclusion limit assuming the WIMPs only couple to neutrons, i.e.,  $a_p = 0$  in Eq. (1.5). Reaching a sensitivity down to  $\sigma_n^{SD} = 2 \cdot 10^{-40} \text{ cm}^2$ , XENON100 stated one of the most stringent limits on the WIMP-neutron SD cross-section. The result for the WIMP-proton SD cross-section (assuming  $a_n = 0$  in Eq. (1.5)) is weaker and shown in Figure 1.10 (Right, bottom). Besides the search for WIMPs, the XENON100 collaboration also published constraints for axion-like particles, an alternative dark matter candidate [51] or leptophilic dark matter models [52].

### 1.2.3. The XENON1T detector

A dedicated paper describing the XENON1T detector in detail is in preparation. After a commissioning phase, the detector started taking science data in December 2016. As XENON100, the experiment is located in the INFN Laboratori Nazionali del Gran Sasso (LNGS). It is operated with a liquid xenon mass of about 3.5 t in total, enhancing the target mass for WIMP analysis by more than an order of magnitude with respect to XENON100. At the same time, the background rate is reduced by an order of magnitude down to  $(1.80 \pm 0.15) \cdot 10^{-4} (\text{kg}\cdot\text{day}\cdot\text{keV})^{-1}$  [42]. Thus, XENON1T is expected to reach a sensitivity of  $\sigma = 1.6 \cdot 10^{-47} \text{ cm}^2$  for the SI WIMP-nucleon cross-section at a WIMP mass of  $m = 50 \text{ GeV}$  [42].

In this section, we give a short introduction to the XENON1T experimental setup. This will be important for the following chapter 2, where we will discuss radon emanation measurements of the different detector subsystems.

#### Cryostat, TPC and muon-veto

As indicated in Figure 1.11 (Left), the XENON1T experiment is a double-walled, stainless steel vessel providing an insulation vacuum between outer and inner cryostat. The inner cryostat houses the 3.5 t liquid xenon reservoir and the experiment’s TPC. The latter has a total length of about 1 m and an equally large diameter. In total, the TPC houses about 2 t of liquid xenon used for dark matter searches. The residual xenon surrounds the TPC and contributes to the detector’s shielding. Similarly to the XENON100 experiment, the TPC of XENON1T has been built according to a diving bell design. The top PMT array is made up from 127 tubes, the bottom array from 121 (3" Hamamatsu R11410-21). These photosensors have been developed for their use in dark matter direct detection experiments and are highly radio-pure [53]. The walls of the TPC are made out of PTFE panels which guarantee a high reflectivity, needed for the scintillation signals. For the electron drift field voltages up to  $-100 \text{ kV}$  can be applied to the cathode. As shown in Figure 1.11 (Right), the outside of the TPC is enclosed into copper field shaping rings which are needed to provide a homogeneous drift field.

In order to achieve the required low background environment, all detector materials have been selected according to their radioactive contamination [54] and their  $^{222}\text{Rn}$  emanation rate (see chapter 2). Muon induced background is mitigated by means of a muon-veto based on a water Cherenkov detector [55]. Figure 1.12 shows a picture of the experimental site. The 10 m high water tank is overlaid by a schematic drawing which indicates the position of the cryostat and its support structure. When a muon penetrates the water tank, Cherenkov light is produced and is detected by PMTs installed in the water tank. A reflecting foil, covering the walls of the water tank, increases the detection efficiency. Monte Carlo simulations showed that the muon veto is able to detect more than 99.5% of the penetrating muons and more than 70% of secondary particle showers originating from muon interactions in the rock [55]. Time coincident events detected in the TPC can then be rejected.

For ER calibration, we use  $^{220}\text{Rn}$  and  $^{83m}\text{Kr}$  as so-called internal calibration sources. Both sources are flushed via the purification loop directly into the liquid xenon target.

## 1. Direct dark matter detection with XENON

---

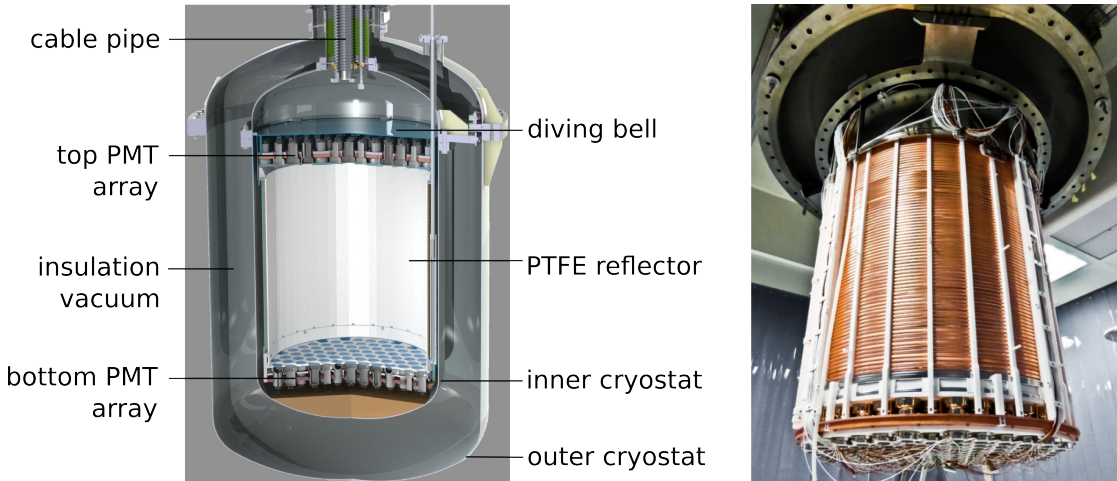


**Figure 1.11.:** (Left) Schematics of the XENON1T cryostat. The outer and inner cryostat are separated by an insulation vacuum. The inner cryostat houses the liquid xenon reservoir and the TPC. (Right) Picture of XENON1T's TPC during assembly before it got enclosed by the inner cryostat. The copper field shaping rings and the bottom PMT array are clearly visible.

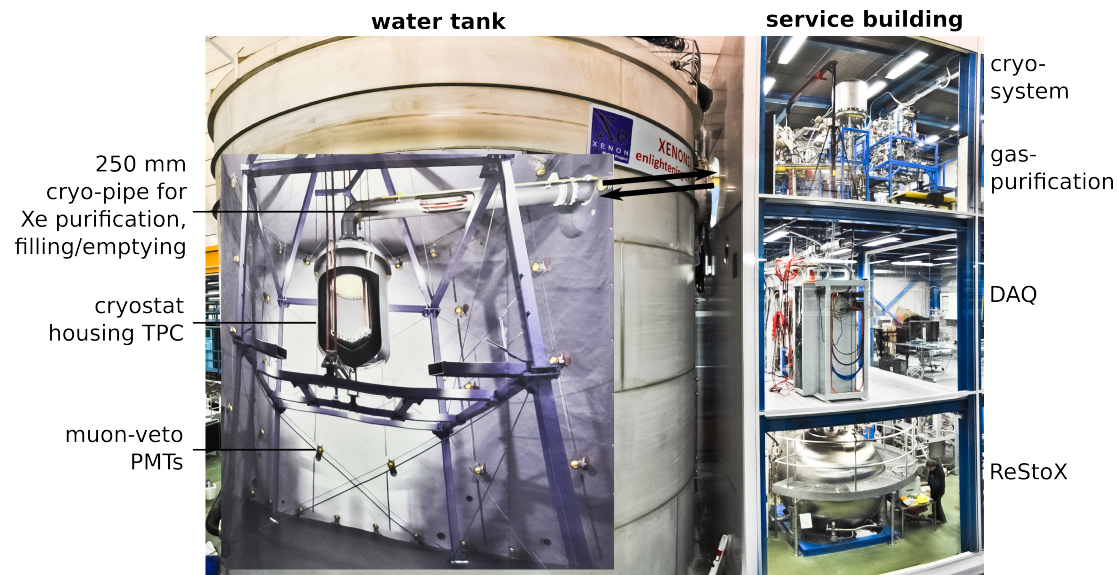


**Figure 1.12.:** Picture of the XENON1T experimental site. The cryostat is placed in a water tank which is acting as an active Cherenkov muon veto. The cryogenic system and the gas purification system are located at the top floor of the service building. The DAQ system and the ReStoX are located in the second floor and ground floor, respectively.

This guarantees a homogeneous calibration in the TPC with respect to external gamma sources which get shielded by the xenon target itself. Since  $^{220}\text{Rn}$  and  $^{83m}\text{Kr}$  don't have any long-lived progenies their background contribution entirely decays away after the calibration measurement. For neutron calibration, an  $^{214}\text{AmBe}$  ( $\alpha, n$ ) source and a neutron generator are used as external sources. Both can be mounted to a belt system which drives the sources into the water tank close to the cryostat.

### Gas purification, cryogenic system and inner piping

As shown in Figure 1.12, the cryostat is connected to the service building via a piping system. Figure 1.13 shows a schematics of the experimental setup including also the detector's inner structure. The *250 mm cryo-pipe*<sup>5</sup> provides the connection from the TPC and the cryostat to the infrastructure outside the water tank (also visible in Figure 1.12). It is vacuum insulated and houses several other pipes such as the *100 mm pipe*, a pipe which guides the signal cables and HV cables of the PMTs of the TPC to several electric feedthroughs located at the so-called *porcupine* vessel (see also Figure 1.13). The XENON1T experiment is equipped with a gas purification system in order to remove electronegative impurities from the xenon target. By means of recirculation pumps (fabricated by QDrive), liquid xenon is sucked from the inner cryostat into the *heat exchanger* (orange line in Figure 1.13). There, the xenon gets evaporated by the heat input of back streaming gaseous xenon. At the purification system, the gas stream gets split and is guided into two parallel purification units. Each consists of the afore mentioned recirculation pump and a hot metal gas purifier, so-called *getter*, which removes electronegative impurities. Thereafter, the combined xenon stream is circulated back into the heat exchanger where it gets liquefied (blue line in Figure 1.13). The purified xenon flows through a pipe back into the cryostat where it finally drops into a funnel located above the TPC. Another pipe injects the liquid xenon directly into the TPC. The gas circulation speed is about 50 slpm and controlled by means of mass flow controllers (MFCs). A *halo monitor* is used to measure traces of water in the gaseous xenon and is used to indicate potential leaks. Just before the purified xenon reenters the heat exchanger, a fraction of about 5 slpm gaseous xenon is separated from the main loop (dashed blue line). Via the *bell pipe*, the xenon is flushed directly into the diving bell in order to regulate the liquid level inside the TPC.

The XENON1T detector is equipped with two PTR *cold heads*<sup>6</sup> located in the *cryo-system*. In standard operation, these cold heads need to compensate the heat input into the system, e.g., from the gaseous xenon flowing directly into the bell. Xenon liquefies and drops into a funnel below each cold head. Being collected by a bigger funnel, which is located in the center of the cryo-system, the xenon is guided from both cold-heads into the inner cryostat. In case of a failure of the PTRs, the cryo-system is equipped with an additional cold-head (*emergency cooling*) which is cooled down with liquid nitrogen.

---

<sup>5</sup>The numbers in millimeter in the pipes names denote their diameters.

<sup>6</sup>Same working principle as we introduced in section 1.2.2 for the XENON100 detector.

# XENON1T Detector Setup

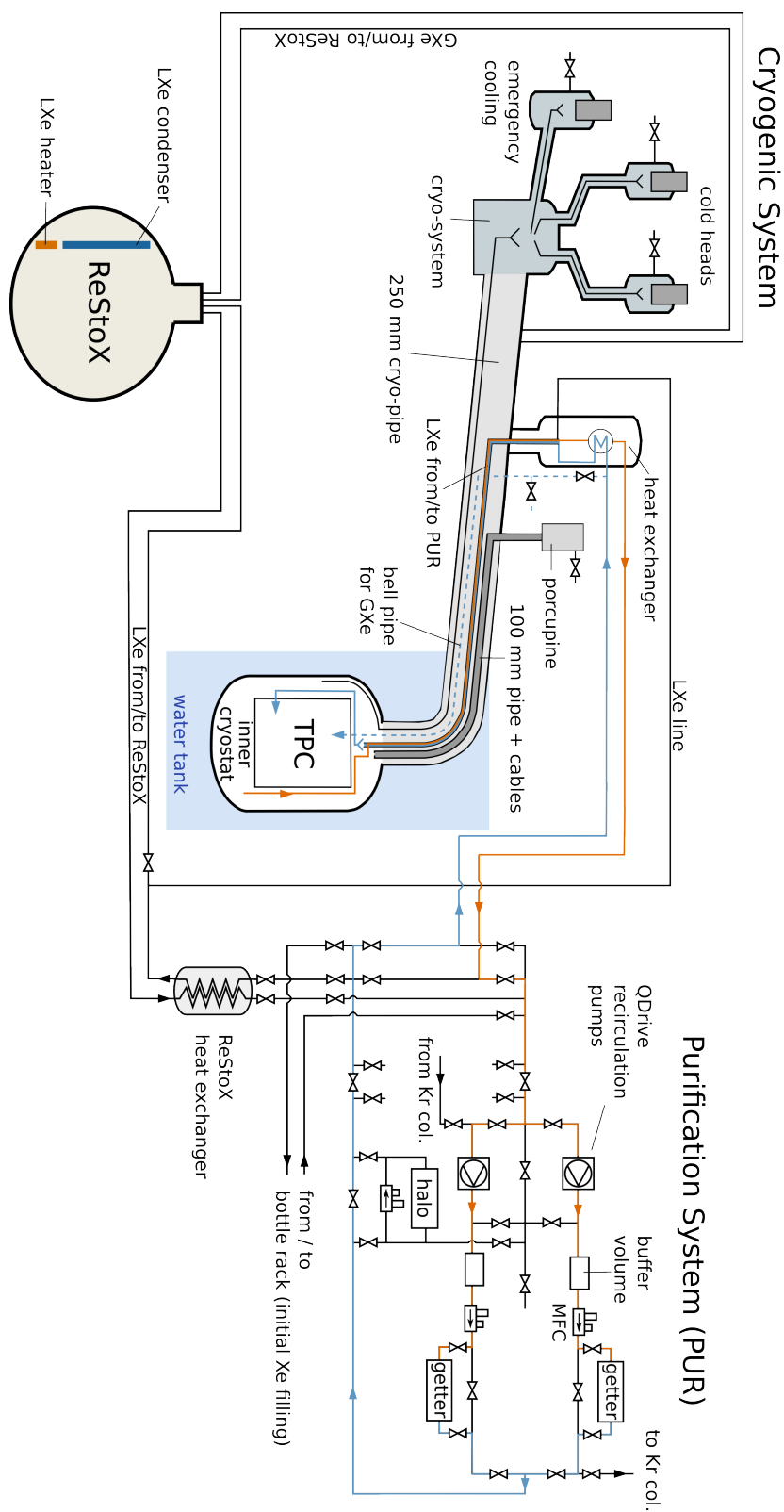


Figure 1.13: Schematics of the XENON1T detector and its subsystems. The single components which are important in the course of the thesis are discussed in the text.

### Xenon storage, bottle rack and cryogenic distillation column

The XENON1T experiment is equipped with a system for recovery and storage of xenon, the so-called *ReStoX*. This stainless steel sphere with an inner diameter of 2.1 m is able to store up to 7.6 t of xenon and is located at the ground floor of the service building (see Figure 1.12). ReStoX provides a cooling power of more than 3 kW by means of nitrogen cooling but is equipped also with an electrical heater. It is designed to stand pressures up to 72 bar and thus can safely store the xenon even in case of a cooling failure. In order to fill the detector with xenon, liquid xenon is flushed from ReStoX into the *ReStoX heat exchanger* (see Figure 1.12) where it evaporates. The gaseous xenon is then circulated through the purification system before it reenters the ReStoX heat exchanger. Again liquefied, the purified xenon is flushed into the XENON1T cryostat after the detector's heat exchanger. In case of an emergency, the same pipe can be used for a so-called fast recovery of the xenon from the cryostat directly into ReStoX.

The so-called *bottle rack*, located at the bottom floor of the service building, provides an interface to connect standard gas cylinders to the XENON1T gas system and was used, e.g., for the initial filling of xenon into ReStoX. As described in [56], the bottle rack also enables to pursue gas analytics to ensure only gas of a certain purity gets filled into the detector.

The anthropogenic krypton isotope  $^{85}\text{Kr}$  is a crucial source of background [42]. It can be found in any commercially available xenon. In order to reduce the  $^{85}\text{Kr}$  contamination, a cryogenic distillation column is used [57]. It is connected via the purification system and enables to purify the xenon before being filled into the detector but also on-line during the experiment's operation.

### Projected sensitivities of XENON1T and XENONnT

At the time of writing this thesis, the XENON1T detector is acquiring science data for a first publication. A projected sensitivity on the WIMP-nucleon cross-section based on Monte Carlo Simulations has been published in [42]. Figure 1.14 shows the updated results in context of other direct dark matter experiments. We expect to increase the sensitivity by two orders of magnitude with respect to XENON100, reaching a sensitivity of  $\sigma = 1.6 \cdot 10^{-47} \text{ cm}^2$  for the SI WIMP-nucleon cross-section at a WIMP mass of  $m = 50 \text{ GeV}$  and an exposure of 20 t·y.

The XENON1T experiment is designed to enable an easy upgrade to its successor, the XENONnT experiment, operated with a total liquid xenon mass of about 7 t. The cryo-system, the inner piping and the outer cryostat of XENON1T can be reused without any changes. Furthermore, signal cables and HV cables for additional PMTs, needed for the larger XENONnT TPC, are already installed. The start of XENONnT is planned in 2019. Due to its larger target mass, it is expected to increase the sensitivity to the range of  $\sigma = 1 \cdot 10^{-48} \text{ cm}^2$  for the SI WIMP-nucleon cross-section (see Figure 1.14).

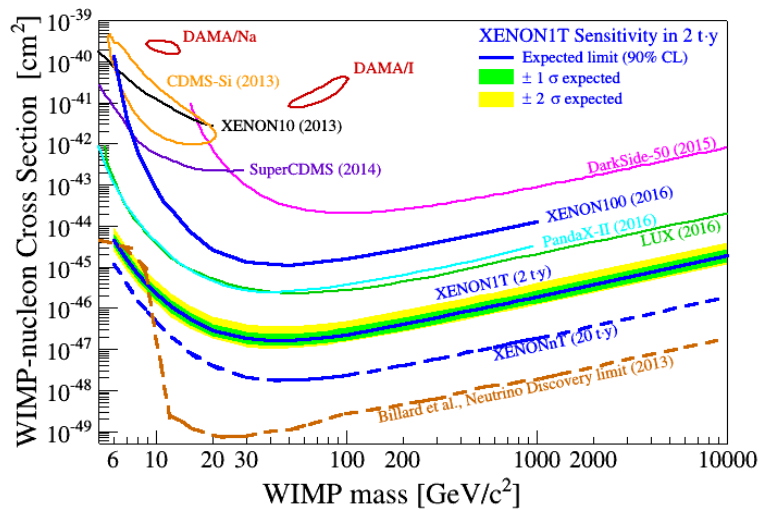


**Figure 1.14.:** Projected sensitivity on the SI WIMP-nucleon cross-section reached by XENON1T and its successor, the XENONnT experiment. Figure courtesy of the XENON collaboration.

# Chapter 2

## Radon mitigation in the XENON1T experiment

Radon is expected to be the dominating source of background in XENON1T due to permanent emanation from detector materials (section 2.1). Its reduction and the analysis of the radon induced background are crucial for reaching the aimed sensitivities of the XENON1T/XENONnT detectors. Careful selection of the detector materials is of essential importance in order to mitigate  $^{222}\text{Rn}$ . As we will introduce in section 2.2, an extensive radon screening campaign was performed in preparation of the XENON1T experiment. The final measurement of the  $^{222}\text{Rn}$  emanation of the fully assembled detector is part of this thesis and will be discussed in section 2.3.

Besides material selection, an alternative approach in order to mitigate  $^{222}\text{Rn}$  induced background is to develop an on-line operated radon removal system. This concept is discussed in section 2.4.1 together with a model describing its purification power for a realistic, liquid xenon based detector system. In the subsequent chapters of this thesis, we will investigate cryogenic distillation as a potential technique to be used in an on-line radon removal system.

### 2.1. Intrinsic $^{222}\text{Rn}$ background in XENON1T

Among the four natural abundant radon isotopes, only  $^{222}\text{Rn}$  (radon) and  $^{220}\text{Rn}$  (thoron) are potential sources of background for the XENON experiments. The two other isotopes,  $^{218}\text{Rn}$  and  $^{219}\text{Rn}$ , are too rare and have too short half lives so that their contribution can be neglected. Radon and thoron belong to the uranium and the thorium decay series, respectively. Since traces of both parent isotopes are abundant in every material,  $^{222}\text{Rn}$  and  $^{220}\text{Rn}$  are permanently produced by disintegration inside construction materials in the detector. These noble gases can reach the liquid xenon reservoir due to the recoil energy transferred in the decay process or by diffusion. The subsequent decays of radon and thoron, see Figure 2.1, are one source of so-called intrinsic background in the xenon target. In order to analyze the contribution of the radon/thoron daughter isotopes, we have simulated their induced background in a simplified toy-model of the XENON1T detector using the GEANT4 toolkit [59]. For more details on the toy-model

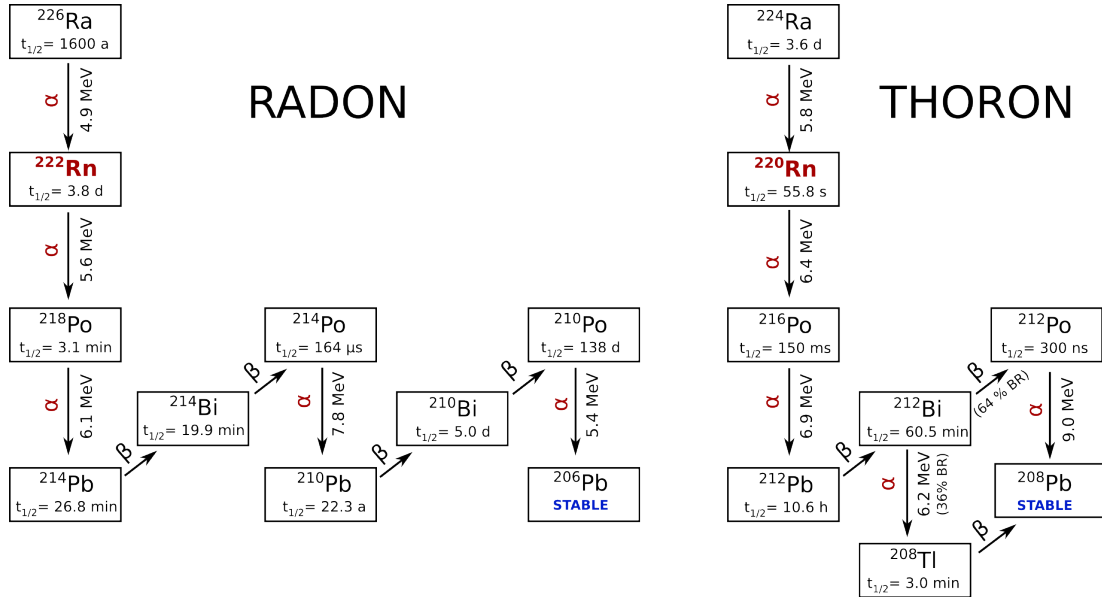


**Figure 2.1.:** Decay chains of  $^{222}\text{Rn}$  (radon) and  $^{220}\text{Rn}$  (thoron) starting from the respective radium mother isotope. These two most abundant radon isotopes are part of the uranium ( $^{222}\text{Rn}$ ) and thorium ( $^{220}\text{Rn}$ ) decay series, respectively. Data taken from [58].

we want to reference to [60] where it has been developed. The results, assuming a homogeneous radon/thoron contamination of  $10 \mu\text{Bq}/\text{kg}$  in the liquid xenon target, can be seen in Figure 2.2. It should be noted that for  $^{222}\text{Rn}$  we neglect  $^{210}\text{Pb}$  and the subsequent  $^{210}\text{Bi}$  decay. This is justified due to the long half-life of  $^{210}\text{Pb}$  of 22.3 y and expected plate-out effects which ensure that metals such as polonium and lead get stucked to the detector walls. In the simulation,  $^{212}\text{Pb}$  and  $^{212}\text{Bi}$ , both from the thoron-chain, dominate the electronic-recoil background in the crucial low-energy region. The expected background rate in the energy region of  $1 - 40 \text{ keV}$  is about  $4 \cdot 10^{-4} (\text{kg} \cdot \text{day} \cdot \text{keV})^{-1}$ . In chapter 4, we will see that the  $^{220}\text{Rn}$  activity measured in the XENON100 experiment is only about 3% of the rate measured for  $^{222}\text{Rn}$ . This observation is supported by previous studies presented in [61]. One explanation is the shorter half-life which prevents thoron to reach the innermost volume of the detector. The expected activity concentrations of  $^{222}\text{Rn}$  and  $^{220}\text{Rn}$  in the liquid xenon target of the XENON1T experiment are  $10 \mu\text{Bq}/\text{kg}$  and  $< 0.1 \mu\text{Bq}/\text{kg}$  respectively [42] based on the results obtained for XENON100. Thus, the contribution of thoron to the internal background source can be neglected.

From our toy-simulation shown in Figure 2.2, we obtain a  $^{222}\text{Rn}$  induced, internal background rate of about  $1.4 \cdot 10^{-4} (\text{kg} \cdot \text{day} \cdot \text{keV})^{-1}$ , in good approximation constant at low energies until 40 keV. This is agreement with the result of dedicated Monte-Carlo-simulations of the XENON1T background where a rate of  $(1.54 \pm 0.15) \cdot 10^{-4} (\text{kg} \cdot \text{day} \cdot \text{keV})^{-1}$  ( $1 - 12 \text{ keV}$ ) has been found [42]. From the simulations they conclude that  $^{222}\text{Rn}$ , homogeneously distributed in the LXe target, is expected to be the dominating background source for the XENON1T experiment.

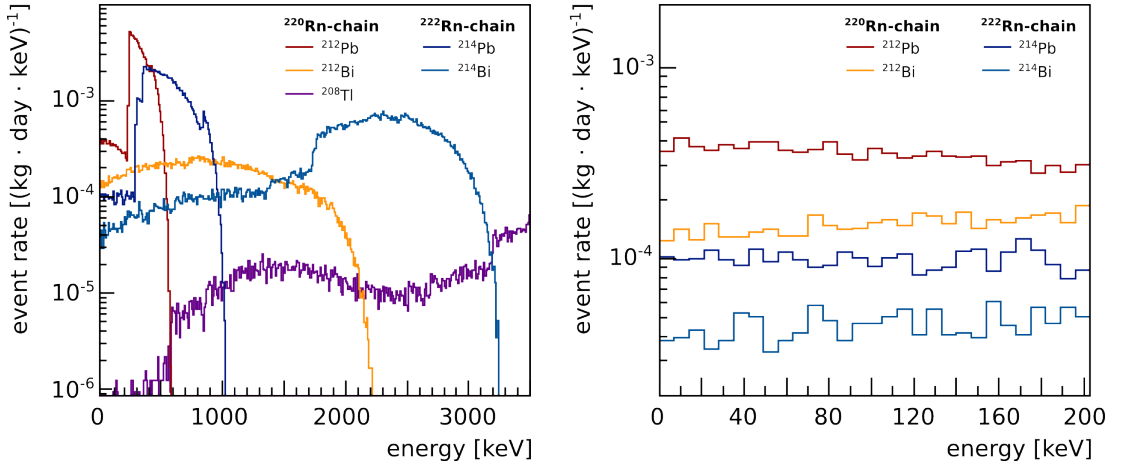


**Figure 2.2.:** (Left)  $^{220}\text{Rn}$  and  $^{222}\text{Rn}$  induced background rates assuming a homogeneous contamination of  $10\,\mu\text{Bq}/\text{kg}$  for both isotopes. (Right) Zoom into the low energy region crucial for dark matter search.

## 2.2. XENON1T radon screening campaign

In order to mitigate the radon induced background, the  $^{222}\text{Rn}$  emanation of all detector materials in contact with liquid xenon have been measured in an extensive screening campaign. Only the cleanest samples have been used for the construction of the XENON1T detector and its gas-system. In this work, we will give only a short introduction to the standard screening procedure, followed by a summary of the most important results obtained for XENON1T. For a detailed discussion of the radon emanation measurement facilities, we want to refer to [62]. After the final assembly of the XENON1T detector, an integral emanation measurement was done of the complete detector system. Since this measurement differs essentially from our standard procedure, it is discussed separately in section 2.3.

### 2.2.1. Screening procedure

The screening procedure follows a sequence of three steps: sample preparation - sample extraction - detector filling. For preparation, we put the sample into a vessel (emanation vessel) with a known  $^{222}\text{Rn}$  emanation rate (background). It should be noted that the emanation vessel itself also can be the investigated sample. This is the case when measuring the emanation from e.g. the XENON1T cryostat. The vessel is closed vacuum tight and all air is pumped out. Then, it is filled with a radon free carrier gas (most cases helium) which was purified by a cooled activated carbon trap. The vessel is filled to a slight overpressure. Radon emanates from the sample into the carrier gas until a constant activity concentration is reached (i.e. emanation equilibrium).

For the sample extraction, the radon enriched carrier gas is pumped slowly from the vessel through an activated carbon trap immersed in liquid nitrogen or liquid argon.

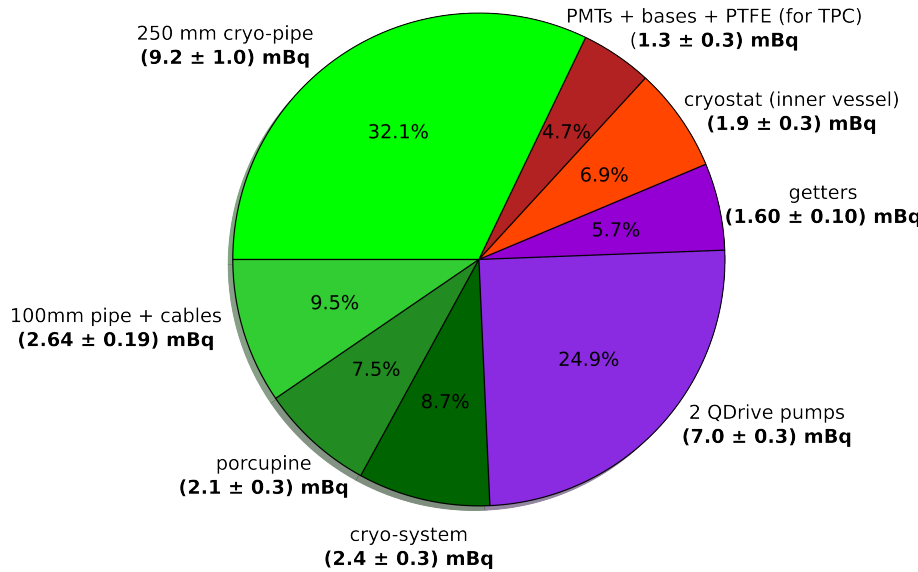


**Figure 2.3.:** XENON1T radon screening results. The different detector components are introduced in chapter 1. For more details on the measuring process, we want to refer to [64]. Figure courtesy of Sebastian Lindemann.

While the carrier gas passes the trap with low resistance, radon gets adsorbed by the activated carbon. At the end of this step, all emanated  $^{222}\text{Rn}$  from the sample is collected inside the trap.

We use miniaturized proportional counters as radon detectors which have been originally developed for the GALLEX/GNO solar neutrino experiment [63]. These highly sensitive devices have an averaged background rate for  $\alpha$ -decays of 0.5 – 1 counts/day and thus reach a sensitivity of  $20\text{ }\mu\text{Bq}$   $^{222}\text{Rn}$  activity. The transfer of the radon, trapped in the activated carbon trap, into the proportional counters requires a dedicated counter filling facility (gas-line). In different operations, the radon is flushed from the trap into the gas-line and separated from traces of other gas impurities. After mixing with the counting gas (9:1 argon/methane mixture), it is pushed by a Toepler-pump into the proportional counter.

### 2.2.2. Emanation results

In Figure 2.3, a summary of the XENON1T radon screening results is given. The individual components are labeled according to the description of the XENON1T detector given in chapter 1. For a detailed discussion of the single emanation measurements, we want to refer to [64].

Summing up the results obtained for the single components, we find a total  $^{222}\text{Rn}$  emanation rate of  $(28.1 \pm 1.2)$  mBq. This corresponds to an activity concentration of about  $10\text{ }\mu\text{Bq}/\text{kg}$  in a 3.3 t liquid xenon target, similar to our assumptions in section 2.1. However, we want to emphasize that our emanation measurements have been performed at room temperature and using helium as a carrier gas. The effect of the sample's

	emanation rate [mBq]
TPC excluded	(14.5 ± 0.7)
TPC included	(19.3 ± 2.1)
XENON1T TPC	(4.8 ± 2.2)

**Table 2.1.:** Radon emanation results for the XENON1T detector (purification system excluded). From the difference of both measurements we infer the emanation rate of the fully assembled TPC.

temperature and the presence of xenon gas on the radon emanation rate is still under investigation. For later purposes we want to separate the contribution from the purification system, i.e. QDrive pumps and getter (violet), from the other emanation sources in the detector system. The latter is dominating with  $(19.5 \pm 1.2)$  mBq while the purification system adds up to  $(8.6 \pm 0.3)$  mBq. From Figure 2.3, we identify the 250 mm cryo-pipe and the QDrive pumps as the main contributors to the total  $^{222}\text{Rn}$  emanation of XENON1T.

During XENON1T’s construction a combined radon emanation measurement of several detector sub-systems has been performed [64]. The measurement included the cryostat (inner vessel), the 250 mm cryo-pipe, the 100 mm pipe and cables, the porcupine and the cryo-system (without TPC). From two consistent measurements a radon emanation rate of  $(14.5 \pm 0.7)$  mBq was determined. That is significantly lower than the expectation from the individual emanation measurements of the sub-systems which sum up to  $(18.2 \pm 1.1)$  mBq (see Figure 2.3). One explanation given in [64] is that due to the complexity of the system, especially due to dead-ended pipes, not all radon has been extracted during the measurement. On the other hand, we know that there have been minor changes at some of the sub-systems after their individual emanation measurements. Furthermore, after assembly the system underwent a cleaning procedure including nitrogen purging followed by several days of vacuum pumping in order to perform a leak test for the detector. Both, the changes of the setup and the cleaning procedure, might be an explanation for an actual lower combined radon emanation rate. After the emanation measurement, the detector was opened again in order to install the TPC. The integral measurements of the fully assembled XENON1T detector, including the TPC, is the topic of the following section 2.3. In order to complete our discussion, we want to anticipate the final result of  $(19.3 \pm 2.1)$  mBq from Table 2.5 (purification system excluded). From the difference between the combined measurement excluding the TPC and the integral measurement we determine an emanation rate of  $(4.5 \pm 2.1)$  mBq for the entire XENON1T TPC (see Table 2.1). From individual measurements of PMTs, PMT bases and PTFE plates used to built up the TPC’s walls, we predicted an emanation rate of  $(1.3 \pm 0.3)$  mBq for the entire TPC (see Figure 2.3). This result, however, neglects possible contributions from further TPC components such as field-shaping rings or level-meter sensors which explains our higher emanation rate inferred in Table 2.1.

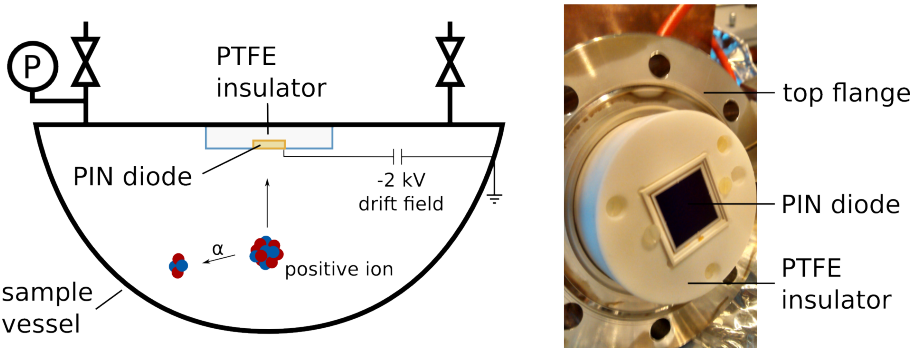


**Figure 2.4.:** (Left) Schematic drawing of the radon monitor. A Si PIN diode is used as an  $\alpha$ -detector. Due to an electric field positively charged radon progenies are drifted onto the diode. (Right) Top flange of the radon monitor (RaMon). The diode is embraced by a PTFE insulator.

### 2.3. Integral emanation measurement of the XENON1T detector

After the final assembly, an integral  $^{222}\text{Rn}$  emanation measurement of the XENON1T system including the TPC was performed. The purification system (i.e., QDrive pumps and getters in Figure 2.3) was excluded. For this measurement it was necessary to modify the standard procedure described in section 2.2 for two reasons: Firstly, the detector has been exposed to xenon and a large out-gassing was expected. This makes the use of the miniaturized proportional counters impossible since the extracted radon cannot be separated from the xenon bulk with the available counter filling facilities. As a consequence, electrostatic radon monitors [65] have been used as alternative detectors. These are large enough to fit both, the radon sample and the out-gassed xenon and will be characterized in section 2.3.1. Secondly, the available pumping facility didn't allow us to extract the system's entire gas volume through the activated carbon trap. Therefore, only a fraction of the sample's radon emanation has been measured. For the upscaling of the emanation rate measured for the extracted gas fraction to the entire system, we need to assume a homogeneous radon distribution inside the detector. In order to guarantee homogeneity, also in dead ended volumes of the detector, we developed a dedicated gas mixing procedure. The measuring process and details of the setup used for sample extraction are explained in section 2.3.2.

#### 2.3.1. Electrostatic collection radon monitors for $^{222}\text{Rn}$ detection

Electrostatic collection radon monitors are commercially used for measuring the  $^{222}\text{Rn}$  concentration in ambient air. The ultra-sensitive detectors used in this work have been developed and constructed at the Max-Planck-Institut für Kernphysik in Heidelberg [65]. Their basic structure is sketched in Figure 2.4. The sample vessel houses the radon containing gas to be measured. The vessel is vacuum tight and resists pressures up to 14 bar (absolute). The amount of filled gas is monitored by a pressure gauge during the mea-

surements. A Si PIN diode<sup>1</sup> is used to detect  $\alpha$ -particles. It is mounted to an insulating PTFE cylinder which is fixed at the top flange of the sample vessel. Studies in ambient air showed that after the radioactive decay of  $^{222}\text{Rn}$  almost 90% of the formed daughter isotope  $^{218}\text{Po}$  are positively charged [66]. Due to an electric field (here  $-2\text{ kV}$ ), applied between the grounded sample vessel and the PIN diode, the  $^{218}\text{Po}$  ions are drifted onto the surface of the PIN diode. In the subsequent decay of the polonium, the emitted  $\alpha$ -particle has a 50% probability to be emitted into the semiconductor detector where it is detected (solid angle argument). Thus, the radon monitor doesn't measure the  $\alpha$ -decay of radon directly but that of its progenies.

Once trapped on the diode, the daughter isotopes stay on the surface and decay according to the  $^{222}\text{Rn}$ -chain to the stable  $^{206}\text{Pb}$ . As a consequence, also the  $\alpha$ -decays of  $^{214}\text{Po}$  and, with a long half-life,  $^{210}\text{Po}$  are observed. As we will learn in the following section, we will use  $^{214}\text{Po}$  for the XENON1T emanation measurements as it has the highest detection efficiency.

In this work, we used two different radon monitors which differ in the size and shape of their sample vessels but using similar PIN diodes. The HP-RaMon detector has a physical volume of 41 and a hemispheric sample vessel. The smaller RaMon detector has a cylindric shape and a volume of about 11. The latter is used also for the radon reduction measurements in boil-off xenon which are the topic of chapter 3. For the detection of  $^{220}\text{Rn}$  and its progenies by means of radon monitors, we refer to [67].

### $^{222}\text{Rn}$ detection efficiency and energy calibration

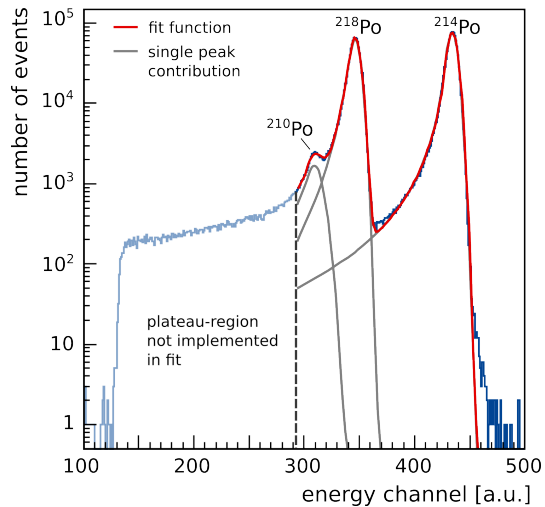
For efficiency calibrations of the radon monitors, we used  $^{222}\text{Rn}$  sources of a known emanation rate in the range of 10 mBq to 30 Bq. Their precise emanation rate has been determined using the miniaturized proportional counters mentioned in section 2.2. For calibration measurements we evacuated the radon monitor and transferred the radon from the emanation source into the sample vessel. Similarly as has been done in the emanation measurements, the radon monitor was then filled with 2 bar (absolute) nitrogen. We define  $-2.0\text{ kV}$  as the standard high voltage setting for the electric drift field in this work. The impact of the carrier gas, filling pressure and electric field on the detection efficiency are discussed later in this section.

In Figure 2.5, a typical energy spectrum is shown as it is acquired with radon monitors measuring a highly active radon sample. The three  $\alpha$ -decays within the  $^{222}\text{Rn}$  chain (see Figure 2.1) are clearly visible. We assign the central peak, at about channel 350, to the direct radon daughter  $^{218}\text{Po}$  and the subsequent  $^{214}\text{Po}$ -decay to the peak with the highest energy at channel 430. The average time interval between both decays is 68 min, short with respect to the  $^{222}\text{Rn}$  half-life of 3.8 d. Thus, their activity corresponds in good approximation to the investigated  $^{222}\text{Rn}$  activity of the sample. The observed  $^{210}\text{Po}$  events, on the other hand, origin mainly from polonium isotopes accumulated on the PIN diode in previous radon measurements. Since its half-life is more than 20 years, the  $^{210}\text{Po}$  event rate changes slowly with time and totally exposed activity.

---

<sup>1</sup>Hamamatsu Si PIN photodiode model S3204-09.

**Figure 2.5.:** An  $\alpha$ -spectrum as acquired with the radon monitors. The peaks of the radon daughters  $^{218}\text{Po}$ ,  $^{214}\text{Po}$  and  $^{210}\text{Po}$  are clearly visible and can be fitted by Crystal-Ball functions. The plateau-region towards lower energies is caused by  $^{222}\text{Rn}$  decay in the gas near the PIN diode.



We can describe the energy spectrum with three overlapping Crystal-Ball functions [68], fitting the means  $\mu_E$  and variances  $\sigma_E$  of the different full adsorption peaks (see Figure 2.5). Crystal-Ball functions are commonly used to model Gaussian distributions which have some tailing. Thereby, the tailing is described by a power function. The Crystal-Ball functions are given by

$$f(E; \mu_E, \sigma_E, \alpha, n) = N \cdot \begin{cases} \exp\left(-\frac{(E-\mu_E)^2}{2\sigma_E^2}\right) & \text{for } \frac{E-\mu_E}{\sigma_E} > -\alpha \\ A \cdot \left(B - \frac{E-\mu_E}{\sigma_E}\right)^{-n} & \text{for } \frac{E-\mu_E}{\sigma_E} \leq -\alpha \end{cases} \quad (2.1)$$

where

$$\begin{aligned} A &:= \left(\frac{n}{|\alpha|}\right)^n \cdot \exp\left(-\frac{|\alpha|^2}{2}\right) \quad \text{and} \\ B &:= \frac{n}{|\alpha|} - |\alpha|. \end{aligned}$$

The parameter  $\alpha$  determines the point where the power function of order  $n$  takes over in order to describe the tailing of the Gaussian. The scaling parameter  $N$  corresponds to the integral of the peak. As indicated in Figure 2.5, the fit model doesn't describe the plateau-region at energies below the  $^{210}\text{Po}$  peak. We assign these events to  $^{222}\text{Rn}$  decays happening close enough to the PIN diode, such that the  $\alpha$ -particles deposit a fraction of their energy in the detector. Since the full adsorption energy of radon is below that of  $^{218}\text{Po}$  and  $^{214}\text{Po}$ , the two isotopes relevant for this analysis, we don't expect any impact from those events.

The fit values for  $\mu_E$ ,  $\sigma_E$  and the measured activity of the single polonium isotopes (obtained from  $N$ ) are shown in Table 2.2. We find that the measured  $^{218}\text{Po}$  activity of the sample is reduced by a factor of  $(0.861 \pm 0.002)$  with respect to  $^{214}\text{Po}$ . The lower detection efficiency of  $^{218}\text{Po}$  is also discussed in [65]. There it is assumed that after the

	$^{218}\text{Po}$	$^{214}\text{Po}$	$^{210}\text{Po}$
$\mu_E$ [channel]	$(346.10 \pm 0.01)$	$(434.18 \pm 0.01)$	$(308.9 \pm 0.1)$
$\sigma_E$ [channel]	$(4.43 \pm 0.01)$	$(4.42 \pm 0.01)$	$(7.1 \pm 0.2)$
activity [Bq]	$(6.69 \pm 0.01)$	$(7.77 \pm 0.01)$	$(0.051 \pm 0.004)$

**Table 2.2.:** Fit-results for the spectrum shown in Figure 2.5 using Crystal-Ball functions. The detection efficiency of  $^{214}\text{Po}$  is observed to be higher with respect to  $^{218}\text{Po}$ .

$^{222}\text{Rn}$  decay only a fraction of the polonium is drifted onto the PIN diode before the ions get neutralized. The residual  $^{218}\text{Po}$  atoms stay in the gas were they disintegrate forming again positively charged daughter ions. Since those have another chance to drift onto the diode, the detection efficiency for the subsequent  $^{214}\text{Po}$  decay is increased. An alternative explanation is given in [66]. Therein, the ionization probability of formed  $^{218}\text{Po}$  atoms is measured to be  $(0.873 \pm 0.016)$ , which is in agreement with  $(0.861 \pm 0.002)$  determined in this work. Consequently, the observed ratio between  $^{218}\text{Po}$  and  $^{214}\text{Po}$  events might be due to the ionization efficiency of the daughter isotopes after the decay. According to this hypothesis neutralization during the ion drift plays no major role. Dedicated measurements at different field strengths of the drift field is suggested for a further investigation.

For this work, we obtained the detection efficiencies for  $^{218}\text{Po}$  and  $^{214}\text{Po}$  from measurements using  $^{222}\text{Rn}$  calibration standards. As discussed above, an efficiency smaller 0.5 is expected from solid angle arguments. The results of a selection of calibration measurements is given in Table 2.3. All calibration measurements of the HP-RaMon detector have been done at defined standard conditions at 2 bar (absolute) nitrogen and a high voltage bias of  $-2.0\text{ kV}$ . The determined detection efficiencies are  $\epsilon_{218} = (0.277 \pm 0.012)$  for the  $^{218}\text{Po}$  decay and  $\epsilon_{214} = (0.310 \pm 0.016)$  for  $^{214}\text{Po}$ . For the RaMon detector, calibration measurements at different high voltages and different filling gases are given in Table 2.3. The obtained detection efficiencies are constant at  $\epsilon_{218} = (0.220 \pm 0.006)$  and  $\epsilon_{214} = (0.243 \pm 0.006)$ . We explain the deviation from the theoretical possible efficiency of 0.5, constraint by solid-angle arguments, by a non-homogeneous drift field inside the radon monitor. Consequently, the detector is blind for some fraction of its sample volume, e.g. close to the PTFE insulator.

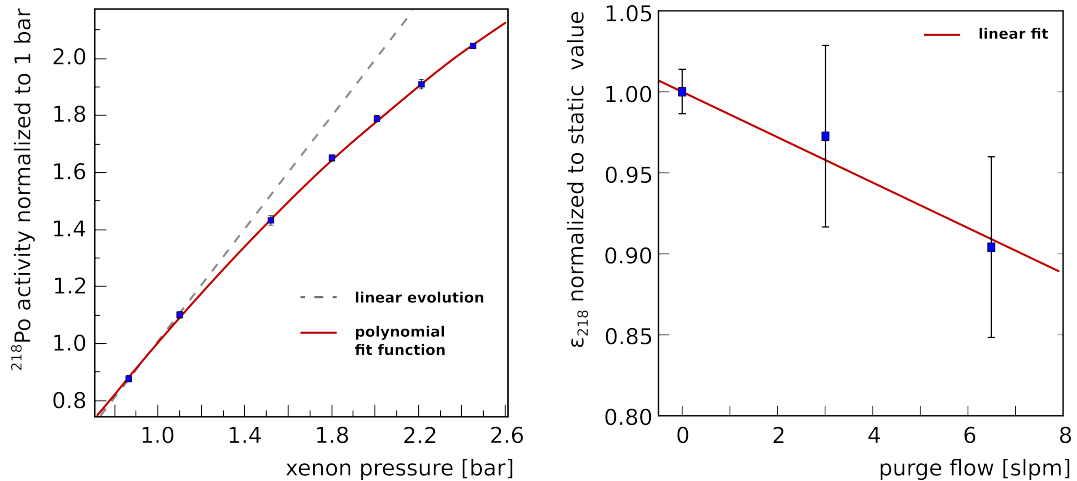
The detection efficiencies might be affected by the filling pressure, the strength of the drift field or the gas composition. Table 2.3 suggests constant values for  $\epsilon_{218}$  and  $\epsilon_{214}$  for RaMon. However, we found a dependency of the  $^{218}\text{Po}$  efficiency  $\epsilon_{218}$  on the xenon gas pressure in the sample volume. For the graph shown in Figure 2.6 (Left), the pressure inside the detector was increased by adding radon enriched xenon gas with a constant activity concentration. Thus, the measured activity should scale with the amount of sample gas inside RaMon. Clearly,  $\epsilon_{218}$  is suppressed at pressures bigger than around 1.4 bar. The efficiency  $\epsilon_{214}$ , on the other hand, was found to be stable in the test series. This effect needs to be accounted for particularly for the boil-off reduction measurements

HP-RaMon					
gas	P [bar]	HV [kV]	activity [Bq]	$\epsilon_{218}$	$\epsilon_{214}$
nitrogen	2.0	-2.0	$(18 \pm 1) \cdot 10^{-3}$	$(0.29 \pm 0.02)$	$(0.34 \pm 0.03)$
nitrogen	2.0	-2.0	$(24 \pm 2) \cdot 10^{-3}$	$(0.29 \pm 0.02)$	$(0.30 \pm 0.03)$
nitrogen	2.0	-2.0	$(28 \pm 1) \cdot 10^{-3}$	$(0.25 \pm 0.02)$	$(0.29 \pm 0.02)$
<b>averaged efficiency:</b>				<b><math>(0.277 \pm 0.012)</math></b>	<b><math>(0.310 \pm 0.016)</math></b>

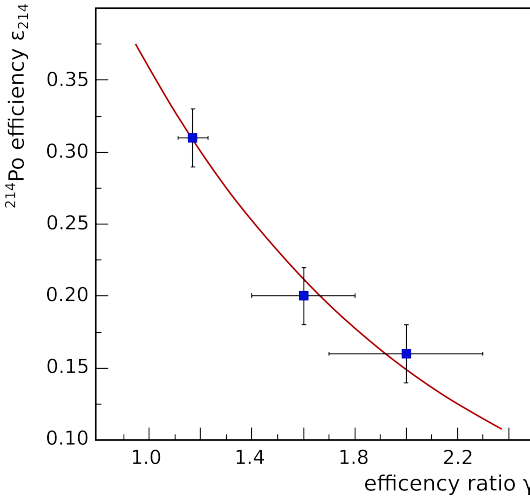
  

RaMon					
gas	P [bar]	HV [kV]	activity [Bq]	$\epsilon_{218}$	$\epsilon_{214}$
nitrogen	1.0	-1.0	$(29 \pm 1)$	$(0.22 \pm 0.01)$	$(0.24 \pm 0.01)$
nitrogen	1.0	-1.5	$(25 \pm 1)$	$(0.23 \pm 0.01)$	$(0.25 \pm 0.01)$
xenon	1.1	-1.0	$(55 \pm 2) \cdot 10^{-3}$	$(0.21 \pm 0.01)$	$(0.24 \pm 0.01)$
<b>averaged efficiency:</b>				<b><math>(0.220 \pm 0.006)</math></b>	<b><math>(0.243 \pm 0.006)</math></b>

**Table 2.3.:** Selection of calibration measurements of the two radon monitors used in this work. The efficiencies  $\epsilon_{218}$  and  $\epsilon_{214}$  are determined for the detection of  $^{218}\text{Po}$  and  $^{214}\text{Po}$  events, respectively, using radon sources of known activity. Additionally, information about the operational mode (filling gas, high voltage) and the strength of the calibration source are given.



**Figure 2.6.:** (Left) Measurement of the  $^{218}\text{Po}$  decays using RaMon operated at  $-1.8\text{ kV}$ . The obtained activity doesn't scale linearly with the amount of the sample gas (indicated by the pressure) which has a constant activity concentration. This points to a pressure dependence of  $\epsilon_{218}$ . (Right) The detection efficiency  $\epsilon_{218}$  for the RaMon detector as a function of the purge flow through the monitor.



**Figure 2.7.:** The ratio  $\gamma$  as an indicator for a reduced detection efficiency  $\epsilon_{214}$  of HP-RaMon operated with 1 bar nitrogen. Gas impurities which neutralize the polonium ions might cause the here shown effect.

discussed in chapter 3. During dynamic measurements, i.e., the sample gas was continuously flushed through the radon monitor with an adjusted purge flow, we observed indication for a decreasing detection efficiency  $\epsilon_{218}$  as a function of the flow. This effect is shown in Figure 2.6 (Right) for the RaMon detector. Given the limited data available at the date of writing this thesis, we describe the evolution of  $\epsilon_{218}$  by a linear fit.

During the integral emanation measurement of XENON1T, we observed a reduced detection efficiency for both radon monitors with respect to our results given in Table 2.3 (see section 2.3.3 for details). Even though operated at the above defined standard conditions,  $\epsilon_{214}$  obtained for the HP-RaMon monitor was reduced by a factor of 2. We explain this effect by impurities inside the detector which have been extracted from XENON1T together with the radon. Some of them might neutralize the polonium ions and prevent them to be drifted onto the PIN diode. As an indicator for a reduced detection efficiency, we identified the ratio

$$\gamma \equiv \frac{\text{number } ^{214}\text{Po events}}{\text{number } ^{218}\text{Po events}} . \quad (2.2)$$

The neutralization effect is expected to have a larger impact on  $\epsilon_{218}$  with respect to  $\epsilon_{214}$ . In Figure 2.7, we show measurements of  $\epsilon_{214}$  as a function of  $\gamma$  obtained during this work with the HP-RaMon detector operated at standard conditions ( $-2.0\text{ kV}$ , 2 bar (absolute) nitrogen). The first data point marks the inverse polonium isotope ratio we discussed before ( $1/\gamma = (0.861 \pm 0.002)$ ). Motivated by the description of the electron attachment to impurities discussed in [43], we choose an exponential description for the observed evolution. Due to our limited data and an expected, non-homogeneous drift field inside the radon monitors, we cannot conclude on the ion life-time or other crucial parameters without further investigation.

### Sensitivity studies

Similar as discussed in [69], we want to investigate the sensitivity of the radon monitors used in this work. We assume a monitor with a background rate  $B(t)$  which is measuring

a radon sample of the activity  $A(t)$ . Both quantities, in general, evolve with time. After the measurement time  $t$ , we expect to observe a certain number of background events  $b(t)$  and signal events  $s(t)$ . Since the number of events is assumed to be Poisson distributed, we find for the total number of events

$$n(t) = n_b(t) + n_s(t) \quad , \quad (2.3)$$

where

$$\begin{aligned} n_b(t) &= \text{Poiss}(b(t)) \\ n_s(t) &= \text{Poiss}(s(t)) \quad . \end{aligned} \quad (2.4)$$

In order to estimate our sensitivity, we want to determine the critical number of events  $n_c(t) = n_b(t) + n_s^c(t)$ , necessary to claim the smallest detectable signal  $n_s^c(t)$  at a confidence level  $\alpha$  given the background  $n_b(t)$  of the detector. For the null hypothesis, i.e.  $n_s = 0$ , we claim

$$P(n(t) \geq n_c(t)) = \sum_{i=n_c(t)}^{\infty} \text{Poiss}(b(t)) = 1 - \sum_{i=0}^{n_c(t)-1} \text{Poiss}(b(t)) \leq 1 - \alpha \quad . \quad (2.5)$$

On the other hand we want to avoid to miss a signal with the required confidence level. Therefore we claim

$$P(n(t) < n_c(t)) = 1 - \sum_{i=0}^{n_c(t)-1} \text{Poiss}(b(t) + s^c(t)) \leq 1 - \alpha \quad . \quad (2.6)$$

For a given background rate of the radon monitor,  $n_c(t)$  can be determined from Eq. (2.5). The result can be inserted into Eq. (2.6) in order to determine  $s^c(t)$  and the corresponding minimum activity of the sample measured with confidence  $\alpha$ .

We want to use above equations in order to estimate the sensitivity of the RaMon detector. Thereby we focus only on  $^{214}\text{Po}$  events, similar as we will do in the later discussed emanation measurements (see section 2.3.3). This restriction is motivated by the higher detection efficiency with respect to  $^{218}\text{Po}$  and the higher stability of  $\epsilon_{214}$  regarding gas pressure and purity. In a background measurement, lasting for 1.5 months, the background rate of RaMon was determined to be 0.7 counts/day ( $^{214}\text{Po}$  events). The radon emanation of the detector itself is thought to be the main source of this background. Therefore, the rate is expected to increase until reaching the emanation equilibrium and has thus a time dependence. In some cases, however, also electronic noise can cause events in our region of interest. For convenience, we will assume here a constant background rate of 0.7 counts/day and find

$$b(t) = 0.7 \cdot t \quad , \quad (2.7)$$

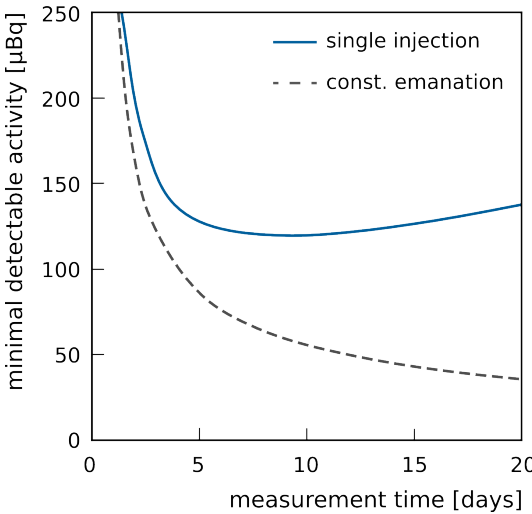


**Figure 2.8.:** Sensitivity limit at 95% C.L. obtained for the RaMon radon monitor as a function of time of measurement. We distinguish two scenarios: The sample is injected at the beginning of measurement and decays (blue solid line). The sample emanates with a constant rate (gray dashed line).

for the expected background events after the time  $t$ . The amount of signal events,  $s(t)$ , detected in the same time period depends naturally on the activity of the sample, but also on the measuring process. We distinguish *single injection* and *constant emanation* measurements. In measurements of the first type, the radon sample is injected at the beginning of the measurement and decays inside the radon monitor. This is the standard operation for the XENON1T emanation measurements. In measurements of the second type, a constant emanation rate is measured. A possible scenario for this type of measurements is an emanation source placed inside the radon monitor (assuming emanation equilibrium and neglecting any impact on the electric drift field). For the expected signal events we can write:

$$s(t) = A_{em} \cdot \epsilon_{214} \cdot t \quad \text{constant emanation} \quad (2.8)$$

$$s(t) = A_0 \cdot \epsilon_{214} \cdot (1 - e^{-\lambda \cdot t}) \cdot \lambda^{-1} \quad \text{single injection} \quad (2.9)$$

$A_{em}$ , in the constant emanation scenario, represents the constant  $^{214}\text{Po}$  activity of the sample and  $\epsilon_{214}$  the detection efficiency as we discussed in the last section. For single injection measurements,  $A_0$  is the sample's activity at the beginning of the measurement. In contrast to a constant radon source, the amount of signal events doesn't increase linear with time but levels off as soon as the sample has been decayed.

We can use the background and signal expectation for RaMon and calculate the detection limit according to Eqs. (2.5) and (2.6). In Figure 2.8 the result for the selected confidence level of  $\alpha = 0.95$  is shown. In case of a single injection (blue solid line), we find a sensitivity limit of about  $120 \mu\text{Bq}$  after 8 days of measurement. This corresponds to about two half-lives of  $^{222}\text{Rn}$ . Then, mostly background events are detected which explains the lower sensitivity for longer measurement times. In case of constant emanation (gray dashed line), we reach a limit of about  $70 \mu\text{Bq}$  in the same measuring period. It is further decreasing reaching a sensitivity below  $50 \mu\text{Bq}$  for measurements longer than 10 days. The values obtained for HP-RaMon operated under standard conditions are simi-

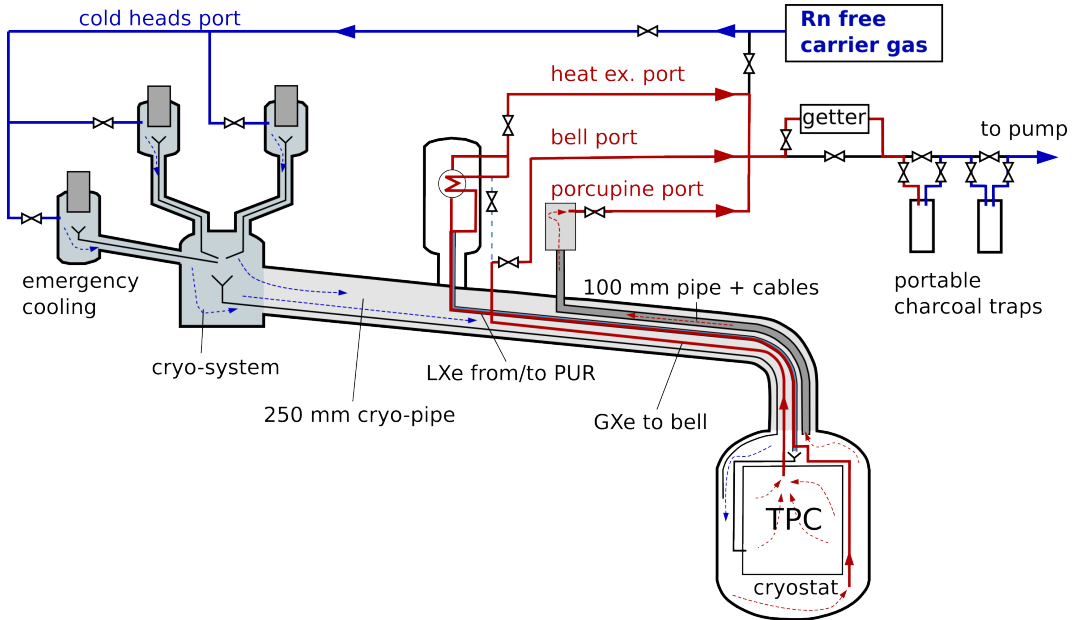


**Figure 2.9.:** Schematics of the detector system during the emanation measurements of XENON1T. In order to ensure the collection of the emanation from all detector sub-systems we use several ports for the filling and extraction of carrier gas. The radon is collected on portable activated carbon traps cooled with liquid nitrogen.

lar. We find a limit of about  $100 \mu\text{Bq}$  after  $t = 5$  days for single injection measurements. Since we expect activities of several mBq for our XENON1T emanation measurements, we conclude that the radon monitors are well suited for this purpose.

### 2.3.2. Setup and measuring process

Figure 2.9 shows a schematics of the setup used during the XENON1T emanation measurements. The detector's different sub-systems are highlighted. Their individual radon emanation rate has been discussed in section 2.2.2. Similar to the procedure introduced in section 2.2.1, the whole system was first evacuated in order to remove all radon before the start of the measurement. Then, the detector was filled with radon free nitrogen up to about 0.5 bar (absolute) used as a carrier gas. We employed activated carbon traps cooled with liquid nitrogen for the purification of the filling gas. In the following days (emanation time), radon from all detector sub-systems accumulated in the carrier gas towards the emanation equilibrium.

During the extraction of the radon enriched carrier gas, the radon was collected on portable activated carbon traps. In order to guarantee that also radon from the detector's dead ends gets extracted, e.g., radon from the '100 mm pipe' or 'porcupine', we used several gas ports as indicated in Figure 2.9. Directly before each extraction, additional, radon-clean nitrogen was pushed into the system via the cold heads port. By doing so, radon originating from the cryo-system and the 250 mm cryo-pipe should be

flushed into the cryostat volume where it mixes with the radon which has been emanated there. In all measurements, we doubled the gas amount during this operation, reaching a filling pressure of about 1 bar (absolute). For the extraction of the radon enriched gas, three ports were used. The heat exchanger port allows for gas extraction from the inner cryostat. Via the bell port, gas was pumped out directly from inside the TPC. The porcupine port ensured that also radon emanated inside the 100 mm pipe got collected in the activated carbon traps.

The extraction was not done simultaneously from all ports the same time. Most of the sample was pumped from the bell port since it connects directly to the detector's biggest volume. We extracted the carrier gas until reaching a pressure of about 0.3 bar inside the XENON1T detector. Then, we refilled the system with radon clean nitrogen via the cold head ports until 0.8 bar. During a second extraction, the carrier gas was pumped out until reaching again a pressure of about 0.3 bar.

Since the detector has been exposed to air during the construction phase, we expected a high out-gassing rate. Therefore, the extracted gas was flushed through a gas purifier (getter) before reaching the activated carbon traps. As shown in Figure 2.9, we used two traps mounted in series for collecting the radon from the carrier gas. Both were cooled with liquid nitrogen during the extraction. All radon should get adsorbed in the first trap. The second, the so-called security trap, was used to ensure that no radon broke through the first trap during the extraction. This was verified by measurements of the radon content in the security trap using proportional counters.

After the extraction, the first activated carbon trap was connected to an evacuated radon monitor. The trap was warmed up to 180 °C while the radon, which got released from the activated carbon, was expanded into the radon monitor. Additionally, we filled the radon monitor with nitrogen via the hot trap to its operating pressure of 2 bar. This ensured that residual radon inside the trap was desorbed and transferred into the monitor. This was again verified by measurements with proportional counters. The residual, not extracted gas inside the XENON1T detector, needed to be pumped from the system before the start of the next emanation measurement.

### 2.3.3. Data analysis and results

Three emanation measurements have been done from the fully assembled XENON1T detector (excluding the purification system). As described in the previous section, the radon sample was extracted from the detector and transferred into the radon monitors. For data analysis, only the  $\alpha$ -decay of  $^{214}\text{Po}$  was used. Its detection efficiency  $\epsilon_{214}$  is the highest and was found to be more robust concerning small changes in the detector's operational mode (see section 2.3.1). From the number of  $^{214}\text{Po}$  events,  $n_{214}$ , detected within the time  $\Delta t$ , we determine the radon emanation rate by

$$A = \frac{n_{214} \cdot \lambda_{Rn}}{\epsilon_{214} \cdot \kappa_f \cdot \kappa_e} \cdot \frac{1}{1 - e^{-\lambda_{Rn} \cdot \Delta t}} \quad . \quad (2.10)$$

Here,  $\lambda_{Rn}$  is the decay constant of  $^{222}\text{Rn}$ . The  $\kappa$ -factors account for corrections specific for the single measurements, e.g., the fraction of the extracted radon sample referred to

date	detector	emanation yield $\kappa_e$	extracted fraction $\kappa_f$
07.01.2016	HP-RaMon	(0.92 ± 0.02)	(0.40 ± 0.01)
12.01.2016	HP-RaMon	(0.50 ± 0.10)	(0.84 ± 0.01)
17.01.2016	RaMon	(0.55 ± 0.09)	(0.86 ± 0.01)

**Table 2.4.:** Overview of the three XENON1T integral emanation measurements. The emanation yield  $\kappa_e$  and the extracted fraction  $\kappa_f$  are used in Eq. (2.10) to infer the radon emanation rate.

as  $\kappa_f$  or the emanation yield  $\kappa_e$ . In the following, we want to discuss each measurement individually. Their basic data is listed in Table 2.4.

**1st measurement (07.01.2016):** The detector was filled with radon free nitrogen on 24.12.2015<sup>2</sup> up to  $p_1 = (1.09 \pm 0.01)$  bar. The time between preparation and the radon extraction was  $\Delta t_e = 14$  days. Since this was too short to reach the emanation equilibrium need to calculate the emanation yield using

$$\kappa_e = 1 - e^{-\lambda_{Rn} \cdot \Delta t_e} = (0.92 \pm 0.02) . \quad (2.11)$$

First, we extracted carrier gas from the detector until  $p_2 = (0.91 \pm 0.01)$  bar through the carbon traps and refilled the detector hereafter to a pressure of  $p_3 = (1.20 \pm 0.01)$  bar. Then, the system was pumped to a pressure of  $p_4 = (0.87 \pm 0.01)$  bar via the activated carbon traps. The fraction of the radon sample extracted in this operation is calculated to

$$\kappa_f = 1 - \frac{p_2 \cdot p_4}{p_1 \cdot p_3} = (0.40 \pm 0.01) . \quad (2.12)$$

As described in section 2.3.2, the sample was transferred from the activated carbon trap into the HP-RaMon detector. In Figure 2.10 (Left) similar data acquired with HP-RaMon in the 2nd measurement is exemplary shown. The event windows for the  $\alpha$ -decays of the different polonium isotopes are chosen according to the peak-spectrum discussed in section 2.3.1. For HP-RaMon we observed bursts of several 100 background events within a time interval of a second (see Figure 2.10). The origin of these bursts is still unclear. Most likely they have been caused by electronic noise induced by other devices in the lab. For data analysis, these time intervals are cut to avoid the contamination of the signal. We used the constant  $^{210}\text{Po}$  rate from the PIN diode to cross-check that our measurements are not contaminated after applying our burst cuts.

In this measurement, we observed an increased polonium isotope ratio of  $\gamma = ^{214}\text{Po}/^{218}\text{Po} = (2.2 \pm 0.4)$ . As discussed in section 2.3.1, this indicates a reduced efficiency  $\epsilon_{214}$ . We suppose that gas impurities, which have been extracted together with the sample from the detector, might have caused this efficiency loss. However, further investigations of the gas composition using a rest-gas-analyzer (RGA) didn't identify any specific candidate. The obtained mass-spectrum is shown in appendix A. In order to estimate  $\epsilon_{214}$  we use

<sup>2</sup>Merry Christmas Danilo and thank you!

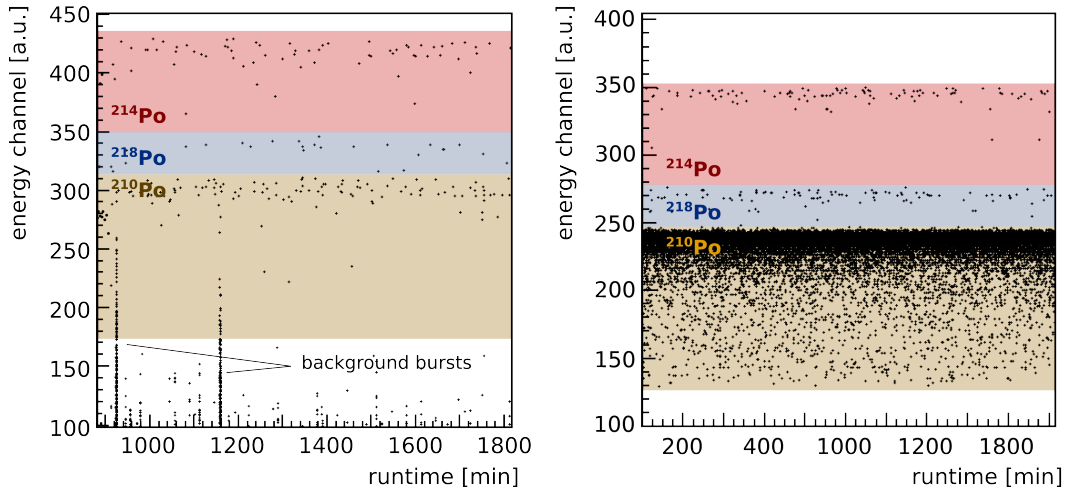


**Figure 2.10.:** (Left) Data from the 2nd measurement acquired with the HP-RaMon monitor. Two prominent background bursts are visible. The affected time periods are cut for analysis. (Right) Data from the 3rd measurement using the RaMon monitor. Due to past measurements of very high activities the  $^{210}\text{Po}$  rate is much higher than the emanation signal.

the exponential fit to data shown in Figure 2.6 (Right) and obtain  $\epsilon_{214} = (0.17 \pm 0.03)$ . Taking into account above corrections, we determine in the 1st measurement a  $^{222}\text{Rn}$  emanation rate of  $A = (19 \pm 4)$  mBq.

**2nd measurement (12.01.2016):** Similar to the 1st measurement, the detector was evacuated and prepared with radon pure nitrogen on 08.01.2016 at a pressure of  $(0.41 \pm 0.01)$  bar. Since the emanation time of the 2nd measurement was only about four days, the emanation yield is  $\kappa_e = (0.50 \pm 0.10)$ . Before the extraction, additional nitrogen was filled via the cold-heads port until reaching a pressure of  $p_1 = 0.88$  bar. Then, we pumped the system via the activated carbon traps down to  $p_2 = 0.30$  bar. After filling again a pressure of  $p_3 = 0.61$  bar, we recuperated until a pressure of  $p_4 = 0.29$  bar. Using Eq. (2.12), we obtain  $\kappa_f = (0.84 \pm 0.01)$ . In Figure 2.10 (Left) the data of this measurement is shown as acquired with HP-RaMon. Similar to the 1st measurement, time periods where background bursts happened were cut.

The polonium isotope ratio is  $\gamma = (2.2 \pm 0.3)$ , similar as in the 1st measurement. This indicates a reduced detection efficiency with respect to the values given in Table 2.3. After measuring the sample extracted from XENON1T, we wanted to do a calibration measurement under the changed conditions. To do so, we connected an empty activated carbon trap to HP-RaMon and cooled it with liquid nitrogen. We extracted the before measured XENON1T sample from HP-RaMon via the trap, the same way than we do in a normal emanation measurement. Then, we injected a calibrated radon source into the evacuated monitor. In contrast to a usual calibration measurement, the detector was not filled with clean nitrogen, but though the warmed up activated carbon trap containing the before extracted gas sample. The measured efficiency for  $^{214}\text{Po}$  events is

## 2. Radon mitigation in the XENON1T experiment

---

date	detector	$\epsilon_{214}$	$^{222}\text{Rn}$ emanation [mBq]
07.01.2016	HP-RaMon	$(0.17 \pm 0.03)^a$	$(19 \pm 4)$
12.01.2016	HP-RaMon	$(0.16 \pm 0.02)^b$	$(19 \pm 4)$
17.01.2016	RaMon	$(0.20 \pm 0.01)^b$	$(20 \pm 3)$
<b>averaged radon emanation rate:</b>			<b><math>(19.3 \pm 2.1)</math></b>

**Table 2.5.:** Results of the three  $^{222}\text{Rn}$  emanation measurements of the fully assembled XENON1T detector (excluding purification system).

<sup>a</sup>Determined by fit as shown in Figure 2.6 (Right).

<sup>b</sup>From calibration measurement.

$\epsilon_{214} = (0.16 \pm 0.02)$ , only 52% of the value obtained under standard conditions. This calibration measurement is used as a data point in Figure 2.6 (Right). Using the new calibration, we compute a  $^{222}\text{Rn}$  emanation rate of XENON1T of  $A = (19 \pm 4)$  mBq for the 2nd measurement.

**3rd measurement (17.01.2016):** The system was evacuated and prepared on the 13.01.2016. The pressure during the emanation was 0.28 bar. From Eq. (2.11) we calculate an emanation yield of  $\kappa_e = (0.55 \pm 0.09)$ . Similar to the previous measurements, we filled as a first step clean nitrogen up to  $p_1 = 0.88$  bar. Then we extracted the sample through the carbon traps until reaching a pressure of  $p_2 = 0.30$  bar. After filling again to  $p_3 = 0.60$  bara we pumped the system down to  $p_4 = 0.26$  bar, again via the activated carbon traps. Altogether, this results in an extracted fraction of the radon sample of  $\kappa_f = (0.86 \pm 0.01)$ .

The 3rd measurement was done using the RaMon detector. In Figure 2.10 (Right), the corresponding data is shown. The much higher  $^{210}\text{Po}$  rate with respect to HP-RaMon is obvious. It is caused by past measurements of very highly active samples (radon reduction measurements in chapter 3). Since in our analysis only the higher energetic  $^{214}\text{Po}$  decay is used, we don't expect any impact due to  $^{210}\text{Po}$ . No background bursts were detected when using RaMon. The ratio of  $^{214}\text{Po}$  and  $^{218}\text{Po}$  was again found slightly increased and was determined to be  $\gamma = (1.3 \pm 0.1)$ . Similar as we did after the 2nd measurement, we determined the reduced detection efficiency by a calibration measurement and obtained  $\epsilon_{214} = (0.20 \pm 0.01)$ . This results in a  $^{222}\text{Rn}$  emanation rate of the XENON1T detector system of  $A = (20 \pm 3)$  mBq.

In Table 2.5, the results of the three emanation measurements are summarized. They are consistent among each other and indicate a  $^{222}\text{Rn}$  emanation rate of the fully assembled XENON1T detector system of  $(19.3 \pm 2.1)$  mBq (gas purification loop excluded). For the discussion of this result in context of previous radon emanation measurements we want to refer to the previous section 2.2.2.

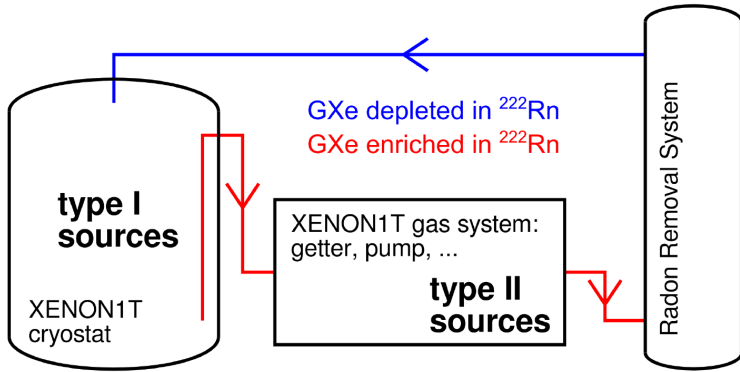


**Figure 2.11.:** Schematics of a radon purification loop. Radon enriched xenon is flushed through a radon removal system where it gets purified. Figure courtesy of Sebastian Lindemann [62].

## 2.4. Concept of an on-line radon removal system for liquid xenon detectors

Once the detector is fully assembled, its radon emanation rate and thus also the radon induced background is set. In order to achieve further background mitigation, the liquid xenon target needs to get continuously purified from emanated radon. In this section, we want to discuss one strategy for realizing an on-line radon removal system and its impact on liquid xenon based detectors similar to XENON1T. In our scenario, the xenon target is looped with a certain recirculation speed through a radon removal unit. There, the radon gets separated from the xenon which is then flushed back into the detector (see Figure 2.11). Since radon and xenon are both noble gases with very similar properties, finding an effective separation technique is essential.

### 2.4.1. Impact of a radon removal system

The mathematical model to describe the impact of a radon removal system realized in a gas purification loop, was discussed in the context of the XENON1T detector in [62]. Since we will use this model when analyzing our data in chapter 4, we repeat in this section its derivation and most important formulas.

From the radon emanation measurements we have learned that the total  $^{222}\text{Rn}$  budget in the XENON1T detector is made up from the contribution of different subsystems. According to their position within the radon purification loop, we distinguish type I and type II emanation sources (see Figure 2.11). Radon originating from type II sources first passes the radon removal system before it is flushed into the TPC. Typical type II candidates are, e.g., recirculation pumps and gas purifiers (getters) as they are used in the XENON1T gas system. Type I sources are characterized by their position directly after the radon removal system or inside the TPC. Radon emanated from type I sources reaches first the liquid xenon target before it passes the radon removal system. Thus, in order to remove type I sources, the radon enriched xenon needs to get first flushed

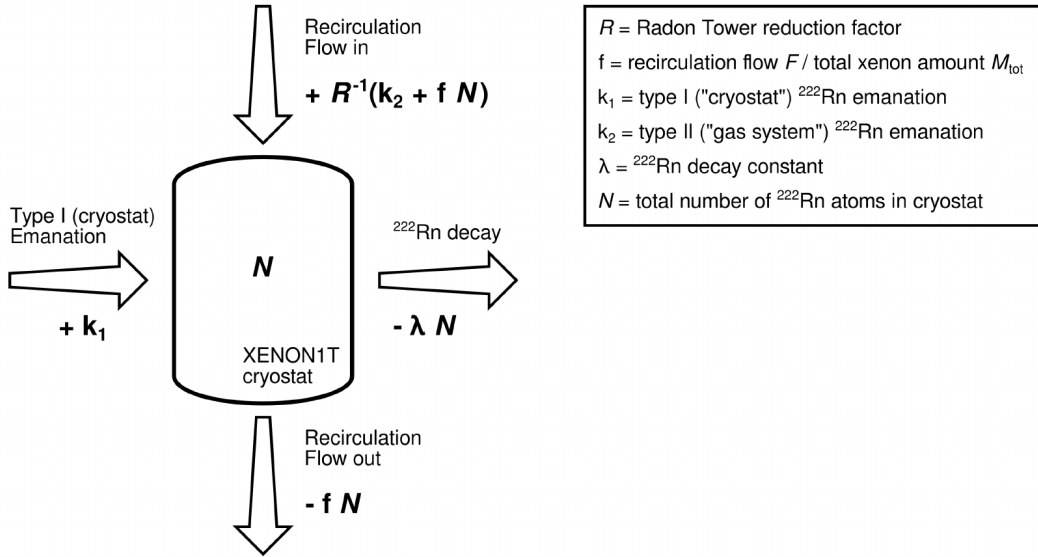


**Figure 2.12.:** Model of the number of radon atoms in the XENON1T experiment. The different radon sources and removal processes are used in the differential equation Eq. (2.13). Figure courtesy of Sebastian Lindemann [62].

out of the detector. The cryostat or the TPC, including PMTs, are typical examples of type I sources in XENON1T.

Assuming a homogeneous radon distribution in the liquid xenon target, the amount of  $^{222}\text{Rn}$  atoms inside the cryostat for the system shown in Figure 2.11 can be described by the differential equation [62] (see Figure 2.12)

$$\frac{\partial N(t)}{\partial t} = k_1 + \frac{k_2}{R} - f \cdot N(t) + \frac{f \cdot N(t)}{R} - \lambda \cdot N(t) . \quad (2.13)$$

Per time unit,  $k_1$  radon atoms of type I and  $k_2$  radon atoms of type II are produced due to emanation. While  $k_1$  directly enters the cryostat,  $k_2$  sources are suppressed by the radon reduction factor  $R$ . This factor expresses the effectiveness of the radon removal system and is defined as

$$R \equiv \frac{c_{\text{in}}}{c_{\text{out}}} , \quad (2.14)$$

where  $c_{\text{in}}$  and  $c_{\text{out}}$  are the radon concentrations of the xenon at the inlet and outlet of the radon removal system respectively. For an RRS having no impact on the detector's radon concentration we find  $R = 1$ . During operation, the xenon is looped with the mass flow  $F$  through the radon removal system. Thus, a fraction of  $(F/M_{\text{tot}}) \cdot N(t)$  radon atoms is flushed out of the cryostat per time unit. The ratio of the mass flow  $F$  and the total mass of the xenon target  $M_{\text{tot}}$  is referred to as flow parameter  $f$  in Eq. (2.13) and has the dimension  $[s^{-1}]$ . The number of radon atoms flushed back into the cryostat is suppressed by the reduction factor  $R$ . The last term in Eq. (2.13) accounts for the

radioactive decay of the radon.

The general solution of  $N(t)$  is given by

$$N(t) = \frac{K}{\Lambda} + [N_0 - \frac{K}{\Lambda}] \cdot e^{-\Lambda \cdot t} , \quad (2.15)$$

where

$$\begin{aligned} K &= k1 + k2/R \\ \Lambda &= [\lambda + f \cdot (1 - 1/R)] . \end{aligned}$$

Of particular interest are the solutions for the limits ( $t \rightarrow \infty$ ) and ( $R \rightarrow \infty$ ) given by

$$N(t) \xrightarrow{t \rightarrow \infty} \frac{K}{\Lambda} = \frac{k1 + k2/R}{\lambda + f \cdot (1 - 1/R)} \xrightarrow{R \rightarrow \infty} \frac{k1}{\lambda + f} . \quad (2.16)$$

The solution for ( $t \rightarrow \infty$ ) determines the reduced and constant radon concentration level in the detector for a given radon removal system providing the reduction power  $R$ . The limit ( $R \rightarrow \infty$ ) points out the dependence of the radon reduction achieved inside the detector on  $f$ . While type II emanation sources can be completely removed, type I sources will be hardly effected due to the limited recirculation speed realized for the detector system.

We can use Eq. (2.16) and the emanation results from section 2.2.2 to predict the impact of a radon removal system for the XENON1T experiment expressed by the reduction factor  $D$ . Thereby, we assume all subsystems inside the cryostat (TPC, 250 mm cryo-pipe, ...) to be type I sources,  $k1 = (19.4 \pm 1.2)$  mBq, while the purification system (QDrive-pumps, getter, ...) are considered as type II sources,  $k2 = (8.6 \pm 0.3)$  mBq. The achievable reduction inside the cryostat is plotted in Figure 2.13 (red labeled contours) as a function of the gas recirculation flow  $F$  and the reduction factor  $R$  of the radon removal system. Realistic flow settings for XENON1T are shadowed. We conclude that even in case of  $R \rightarrow \infty$  only a reduction of a factor  $D = 3.5$  is possible for XENON1T at the present stage. In our scenario, this is explained by the dominating type I sources in combination with the limited recirculation speed. In order to achieve a higher radon reduction, we need to increase  $F$  or prevent type I classified radon from entering the liquid xenon target. We will come back to the latter at the end of chapter 4.

## 2.4.2. Radon-xenon separation techniques

Radon and xenon are both noble gases having very similar physical properties. This makes it difficult to find a separation technique to be used for the here discussed radon removal system. In previous works, adsorption on activated carbon [62, 70] and cryogenic distillation [62] have been investigated. The aspects of both separation techniques are shortly summarized in this section.

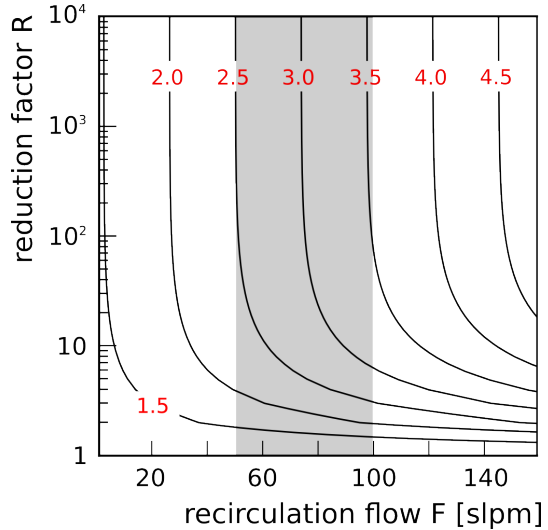


**Figure 2.13.:** Estimated impact of a radon removal system in XENON1T as a function of the gas recirculation flow  $F$  and the reduction factor  $R$ . The shadowed region marks realistic flow settings. The red labeled contours give the achieved radon reduction inside the detector.

### Radon removal based on adsorption

Adsorption as a separation technique is widely used, e.g., in gas chromatography [71]. During the radon emanation measurements, we also made use of the fact that radon is much more likely to get adsorbed in our activated carbon traps than the carrier gas used (see section 2.2.1). In [70], activated carbon traps have been developed to act as a radon removal system for the XMASS experiment [72]. In a test setup, radon enriched xenon was looped with a flow rate of  $F = 1$  slpm through a series of two cylindric traps, providing in total a path length of 180 cm filled with 5.5 kg activated carbon<sup>3</sup>. During operation, the charcoal was cooled to  $-85^\circ\text{C}$  to enhance the radon adsorption. Under these conditions, the retention time of  $^{222}\text{Rn}$ , i.e., the time it takes until radon passes the charcoal trap, was found to be  $T_{Rn} = (14.75 \pm 0.50)$  days. Since this corresponds to about four times the half-life of  $^{222}\text{Rn}$ , the radon concentration at the outlet of the charcoal trap is reduced by a factor of  $R = 15.5$  with respect to the inlet. This theoretical reduction capability, however, turned out to be reduced by the radon emanation of the activated carbon itself. For the described charcoal trap, an emanation rate of  $\leq 3.1$  mBq is expected [70]. Operated at the XMASS detector with a recirculation flow of 1 slpm, this radon removal system is expected to reduce the radon transfer into the detector from 12 mBq to 4.8 mBq [70]. Experimental data that support this calculations has not been published at the time of writing this thesis.

The development of an adsorption based radon removal system for XENON1T has been investigated in [62]. For a charcoal trap achieving a radon reduction factor  $R$ , it was found that the fraction

$$k_{ch} = (1 - 1/R) \cdot \ln^{-1}(R) \quad (2.17)$$

of the charcoal's total radon emanation rate will enter the detector. This additional type I source was estimated to be too high for all investigated adsorbent materials even

<sup>3</sup>Shirasagi G2X4/6-1 by Japan EnviroChemicals, Ltd.

for unrealistic large  $R$ -values. Another important aspect is the adsorption of xenon in the charcoal trap which has been pointed out in [73]. Measurements showed that the mass of adsorbed xenon per charcoal mass is about 1.3 g/g at a pressure of 1 bar and a temperature of  $-80^{\circ}\text{C}$ . Thus, large amounts of additional xenon will be needed for the operation of an efficient radon removal system.

### Radon removal based on cryogenic distillation

Cryogenic distillation is commonly used in industry and science to clean gases or liquids from traces of impurities. In order to achieve the required xenon purity in terms of krypton contamination, a cryogenic distillation column has been constructed for the XENON1T experiment [57]. It has been designed to reduce the krypton concentration in the liquid xenon target below  $0.1 \cdot 10^{-12} \text{ mol/mol}$  before the start of a dark matter run. Measurements show that the column provides a krypton reduction factor of about  $R = 3.7 \cdot 10^5$  by means of cryogenic distillation. The separation of radon from xenon, however, hasn't been investigated yet.

In the distillation process, the more volatile component of a binary liquid (e.g., a xenon and radon mixture), gets enriched in the gas blanket above the liquid surface. Its enhancement in the gas phase is in literature described by the volatility factor  $\alpha \geq 1$ . It is defined as the ratio of the vapor pressures of the two components at the corresponding temperature. A single gas and liquid phase is referred to a single stage distillation. In this case,  $\alpha$  is equivalent to the reduction factor  $R$  of the less volatile component in the gas phase (see appendix B for more details). In multiple stage processes, e.g., realized in distillation columns, the separation effect is enhanced by repeating the single stage process using only the already enriched/depleted phase from the previous stage.

In case of a xenon/radon mixture, xenon is the more volatile component and enriched in the gas phase. The vapor pressures of both noble gases as a function of temperature are shown in Figure 2.14 (Left). Experimental data for xenon is taken from [74]. Data on the vapor and sublimation pressures of radon is very limited. In [75], an empirical equation for the radon vapor pressure curve based on [76] is developed and adapted to published data. We will discuss these measurements in chapter 3 in more detail in the context of our own results (see section 3.5). In Figure 2.14 (Right), this empirical description is used to determine the volatility  $\alpha$  as a function of temperature. According to this model we expect a radon reduction in the gas phase above a liquid xenon reservoir by a factor of about  $R = 11$  at liquid xenon temperatures.

The separation of radon from xenon by means of cryogenic distillation is the main topic of this thesis. In chapter 3 we will present measurements of the reduction factor  $R$  in a single stage distillation setup. The application of radon distillation in an on-line radon removal system is studied in chapter 3.

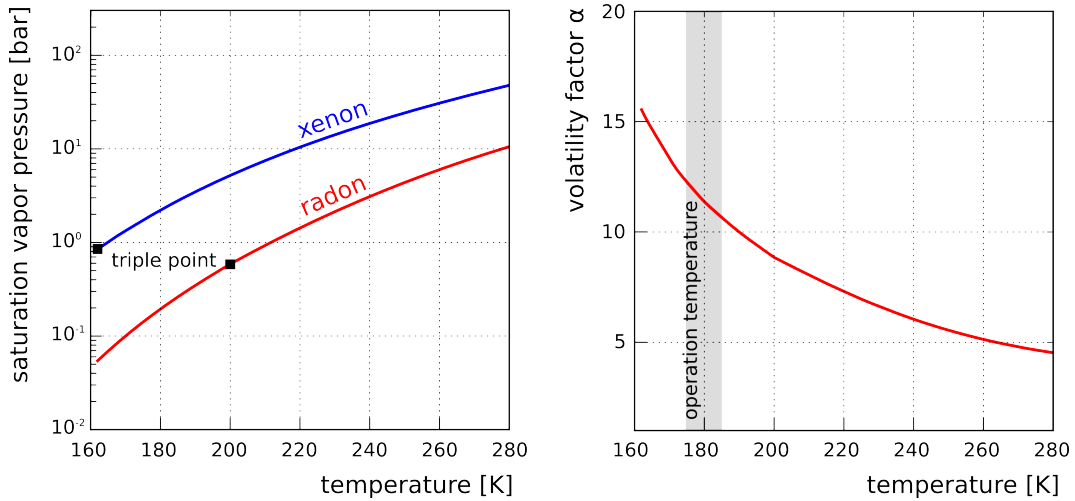


**Figure 2.14.:** (Left) The saturation vapor pressures of xenon (data from [74]) and radon (empiric description from [75]). (Right) The expected radon reduction in a single distillation stage as a function of temperature.

## 2.5. Summary and conclusions

In this chapter,  $^{222}\text{Rn}$  has been identified as the dominating source of the electronic recoil background in XENON1T. It permanently emanates from detector materials into the liquid xenon target where the decay of its daughter isotopes can mimic dark matter events. In order to mitigate this background, all materials being in contact with xenon have been screened in terms of their radon emanation rate. After the final assembly of XENON1T, the radon emanation of the full detector system has been measured. Due to out-gassing and the complexity of the detector, we modified the standard procedure for emanation measurements. Radon monitors were characterized and used for this purpose. The  $^{222}\text{Rn}$  emanation rate of the detector was determined to be  $(19.3 \pm 2.1)$  mBq excluding the purification system.

The radon concentration in liquid xenon detectors can be further reduced by means of a radon removal system. In this chapter, we discussed the concept of a purification loop where radon gets separated from the circulated xenon. A promising separation technique is cryogenic distillation. In the following chapters we will investigate its radon reduction capability and its application in a radon removal system.

# Chapter 3

## Radon depletion in xenon boil-off gas

In the previous chapter we discussed the idea of an online radon purification of the liquid xenon target based on cryogenic distillation. This technique makes use of the different saturation vapor pressures of radon and xenon at a given temperature. As a consequence, the relative radon contamination in xenon boil-off gas is reduced with respect to the liquid phase. Our considerations in section 2.4 predict a radon reduction by a factor of  $R = 11$  at liquid xenon temperature. However, the experimental proof of this so-called boil-off reduction hasn't been given yet. In this chapter, first measurements to study radon depletion in the xenon boil-off gas are shown. Therefore, several kg of radon enriched xenon were liquefied inside the HeXe (Heidelberg Xenon) experimental setup. Then, the HeXe cryostat was emptied again by flushing the gas phase above the liquid surface slowly into a stainless steel bottle immersed in liquid nitrogen by means of cryo-pumping. This operation is in the following referred to as recuperation of the cryostat. During recuperation, the radon activity concentration of the boil-off gas was continuously monitored using a radon monitor (RaMon detector, see section 2.3.1). Measurements with proportional counters [63] provided complementary results. The ratio of the activity concentrations in the liquid reservoir and of the recuperated gas phase determines the investigated boil-off reduction. The here presented studies proof the applicability of cryogenic distillation to be used as a separation technique in a radon removal system for xenon based detectors.

We start this chapter by introducing the Heidelberg Xenon (HeXe) setup in section 3.1. The preparation of homogeneously mixed, radon enriched xenon as well as the process of measuring the radon depletion in boil-off gas are discussed in section 3.2. After a description of the analysis methods, see section 3.3, we present the individual runs in detail in section 3.4. Differences between the measurements, such as recuperation flows or mass of the liquid xenon reservoir, are pointed out and their impact on the boil-off reduction is discussed. The results are summarized in section 3.5 and section 3.6, followed by a final discussion of the results. The most important findings of this chapter have been published in [77]. Here, we discuss our results in detailed and introduce also additional analysis strategies.

### 3. Radon depletion in xenon boil-off gas

---

## 3.1. The Heidelberg Xenon (HeXe) setup

The HeXe setup, as it was used in our measurements, can be divided into two subsystems. The HeXe cryostat is the central element of the setup. It houses the radon enriched liquid xenon reservoir which is recuperated throughout the run. The gas system is designed to enable the filling and recuperation of gaseous xenon from the cryostat but it also connects the radon monitor to measure the radon activity of the boil-off gas.

### 3.1.1. HeXe cryostat

The HeXe cryostat is composed of a stainless steel vessel, containing the liquid xenon reservoir, and a cooling system at the top. Both components are connected to a main flange which itself is held by a support structure (see Figure 3.1). A Gifford-McMahon refrigerator (cold head) provides a constant cooling power of 200 W for xenon liquefaction. The refrigerator is in thermal contact with a copper block inside the cryostat which acts as a cold-finger. As indicated in Figure 3.1, the copper block is equipped with 4 PT100 sensors which monitor the temperature inside the cold finger. One of those PT100 sensors is used to control 3 heating cartridges which are placed between cold-head and cold-finger. The heating cartridges can provide a maximum heating power of 300 W, and are adjusted so that the refrigerator's cooling power is partly compensated in order to keep the copper block constant at the liquefaction temperature of xenon. The liquid drops, falling off the cold finger, are collected by a funnel which guides the liquid xenon through a vacuum insulated pipe into the main volume of the cryostat.

The stainless steel vessel, which houses the liquid xenon reservoir, has an inner diameter of 200 mm and a height of 540 mm. It is placed on a movable platform which enables to lower the vessel after removing the connecting screws to the main flange. The vessel is vacuum insulated and equipped with a heating plate at the bottom. Using its additional heating power, the xenon evaporation can be enhanced to enable higher recuperation flows for the boil-off gas. In standard operation, a cylindric bell structure, having a height of 300 mm and a diameter of 150 mm, was placed inside the cryostat. Its bottom edge is 10 mm above the cryostat's floor so that the liquid xenon reservoirs inside and outside the bell are connected. However, as the liquid level rises above the bottom edge, the boil-off gas phases inside and outside the bell get separated. During the measurements, radon enriched xenon gas was filled into the cryostat via a feed-through in the main flange. The gas entered the volume outside of the bell structure. During our measurements, the radon depleted boil-off gas inside the bell was flushed out through a flexible pipe which is connecting the top of the bell to a second feed-through of the main flange.

The HeXe system is not equipped with dedicated level-meters. Instead, a CCD camera is mounted inside the bell providing pictures of the liquid surface. A scale inside the bell allows to determine the liquid level. Additionally, eight PT100 sensors, mounted on a PTFE stick outside the bell-structure, give some information about the filling level. During our measurements, however, the liquid level was determined more precisely by means of the CCD camera.

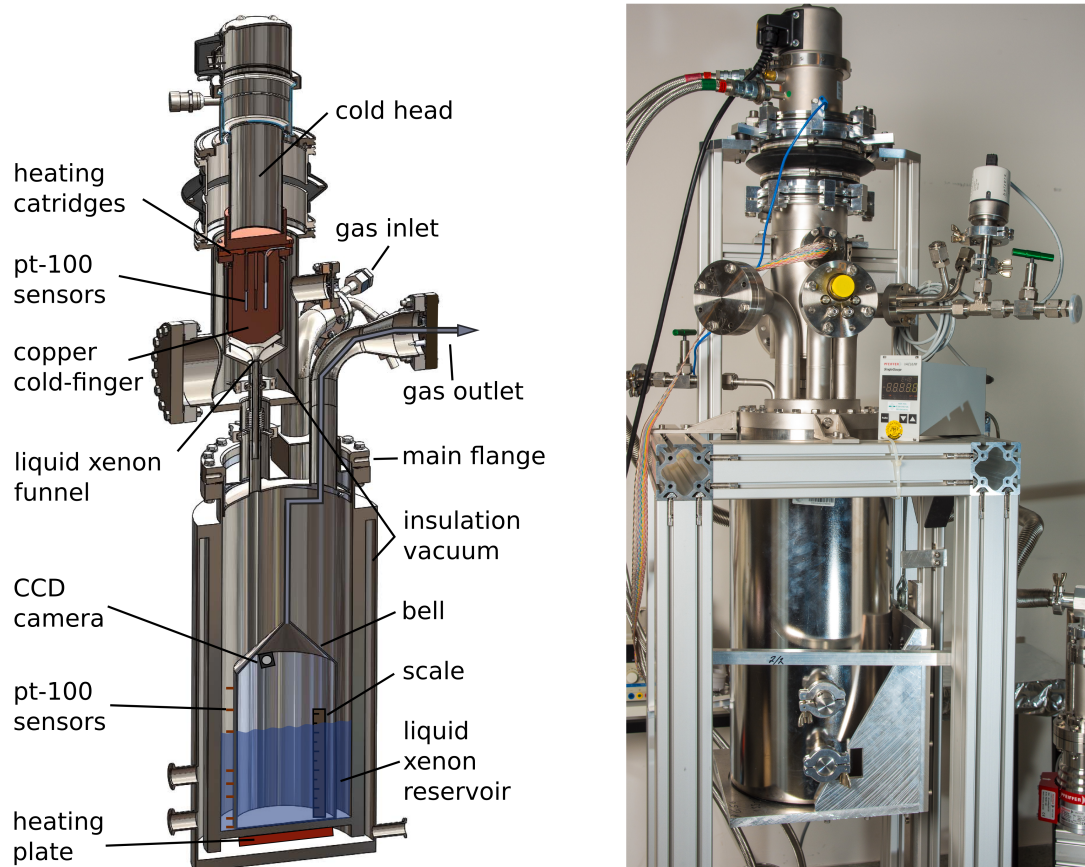


**Figure 3.1.:** (Left) Sketch of the HeXe cryostat. The cooling system with the copper cold-finger for xenon liquefaction is located at the top. Liquid xenon drops are guided into the main vessel. The bell structure at the floor of the cryostat separates inflowing gas from the boil-off gas recuperated from the bell. (Right) Picture of the HeXe cryostat. A support structure holds the main flange which connects the cooling system with the vacuum insulated vessel which is housing the liquid reservoir.

### 3. Radon depletion in xenon boil-off gas

---

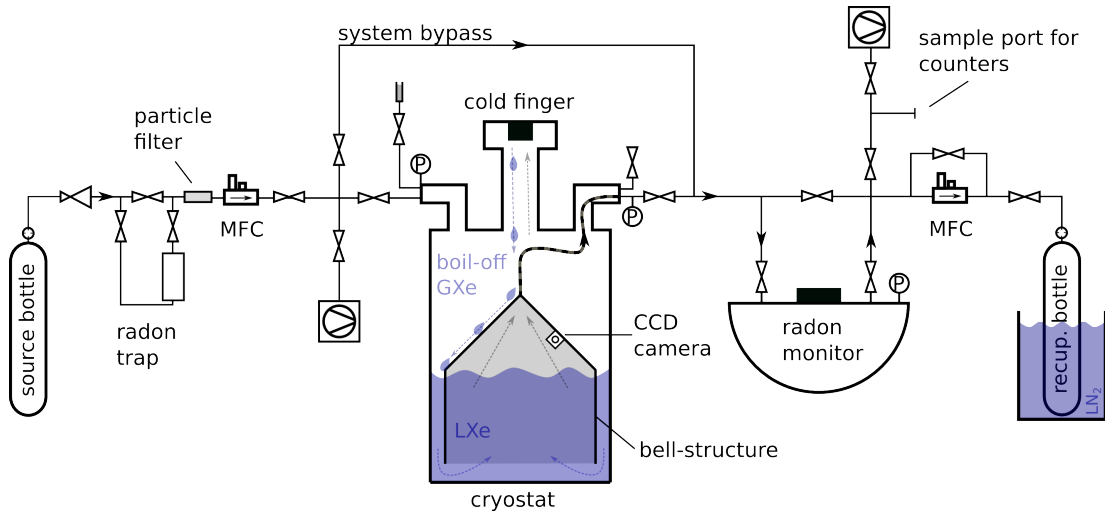


**Figure 3.2.:** Schematics of the experimental setup. The gas system connects the HeXe cryostat with the source- and recuperation bottle and the radon monitor. Details about the individual components as well as about the measuring process are given in the text.

#### 3.1.2. Gas system

The schematics of the gas system, including the HeXe cryostat is shown in Figure 3.2. It provides two connection ports for standard gas cylinders, labeled as source bottle and recuperation bottle, respectively. Before each measurement, we filled the cryostat with xenon gas from the source bottle. Thereby, the mass-flow was controlled using a mass-flow controller (MFC). During the run, we extracted radon depleted boil-off gas from the cryostat and flushed it through the radon monitor into the recuperation bottle (i.e., the recuperation process). The mass-flow, driven by cryo-pumping towards the cooled recuperation bottle, was again controlled by means of a MFC. A sample port, placed behind the radon monitor, enabled us to take samples of the boil-off gas. These samples were used for complementary measurements of their radon activity concentration employing miniaturized proportional counters.

We used the gas system also for the preparation of radon enriched xenon gas (see following section 3.2). For this procedure, the system is additionally equipped with a radon trap and a line to bypass the HeXe cryostat (system bypass).

## 3.2. Process of measuring

The process of measurement includes: the preparation of the radon enriched xenon, the filling of the cryostat with a certain amount of radon enriched gas and the recuperation of the boil-off gas while simultaneously measuring its radon activity concentration. In this section we also want to point out differences in the procedure between the individual runs which will be important for later analysis.

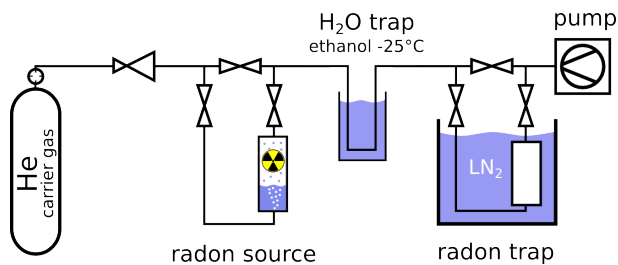


**Figure 3.3.:** Using helium as a carrier gas, radon from an aqueous standard was flushed into a charcoal trap (radon trap) where it got adsorbed. The H<sub>2</sub>O trap removes humidity. Later, the charcoal trap was connected to the HeXe gas system to enrich xenon with radon.

### 3.2.1. Preparation of radon enriched xenon

We used an aqueous radium standard, having an activity of approximately 20 kBq, as a radon source. It is preserved in a sealed glass vessel under helium atmosphere. For radon extraction, we used a small helium flux to rinse the aqueous standard with the gas (see Figure 3.3). By doing so, radon was flushed from the standard into a cooled charcoal trap (radon trap) where it got adsorbed. We placed a H<sub>2</sub>O-trap between the radium standard and the radon trap. It consists of an U-shaped pipe filled with glass wool and was immersed in cold ethanol in order to freeze out humidity. After about 0.5 h of flushing helium with a flow of a few ml/min, we stopped the radon extraction. Residual helium was pumped from the cold radon trap now loaded with radon. The radon extraction efficiency of the above described procedure hasn't been investigated in detail since the absolute amount of radon was not important at this stage. As a next step, we connected the radon loaded trap to the HeXe gas system as it is shown in Figure 3.2. At this point, we distinguish between the so-called In-situ preparation procedure and the Pre-filling preparation procedure. As we will see in section 3.3, the data analysis differs according to the preparation procedure of radon enriched xenon.

**In-situ preparation** In this procedure, we enriched the xenon with radon directly inside the HeXe cryostat before the start of the run. As a first step, we connected the radon loaded charcoal trap to the gas system. A cylinder of clean xenon was used as the source bottle in Figure 3.2. The HeXe cryostat, the gas-system and the radon monitor were evacuated. By means of a heating jacket, we baked the radon trap so that the adsorbed radon got released from the charcoal. A small xenon flux from the source bottle flushed the radon from the trap into the HeXe cryostat which was still at room temperature. Having filled about 30 standard liters (sl) of xenon, we stopped filling. The radon activity concentration of the highly enriched xenon was determined using the radon monitor. Therefore, we expanded the gas from the cryostat into the monitor. Gas samples for complementary measurements using proportional counters were taken from the sample port shown in Figure 3.2. As a next step, we closed the cryostat and started cooling for xenon liquefaction. As soon as the system was running stable, i.e. the cryostat pressure and the temperature of the cold finger were constant, we filled

### 3. Radon depletion in xenon boil-off gas

---

additional, but now radon-free xenon from the source bottle into the cryostat. During this process, the filled gas got continuously liquefied such that the pressure inside the cryostat was kept stable. Having filled the desired xenon mass, the cryostat's gas inlet was closed and the measurement was ready to start. As we will discuss in section 3.4, the activity concentration of the liquid xenon reservoir was determined by the measurement of the highly enriched xenon gas multiplied by the dilution factor which is obtained from measuring the additional filled, radon-free gas. The In-situ preparation has been used only in the first two runs. For the later measurements, we used the Pre-filling preparation method as an alternative.

**Pre-filling preparation** In contrast to the In-situ preparation procedure, the total amount of radon enriched xenon gas was produced before filling it into the HeXe cryostat. As a starting point, we connected a cylinder of clean xenon (source bottle) and the radon loaded charcoal trap to the gas system (see Figure 3.2). The empty recuperation bottle was immersed in liquid nitrogen. At the end of this preparation process, it contained the radon enriched xenon. The gas system was evacuated and the radon trap was baked using a heating jacket to release the adsorbed radon. Clean xenon gas was then transferred from the source bottle through the hot radon trap to the recuperation bottle by means of cryo-pumping (i.e., recuperation). In this step, the HeXe cryostat and the radon monitor were bypassed. After the transfer, the recuperation bottle was warmed up and was reconnected as the new source bottle to the gas system for the boil-off measurement (see Figure 3.2). The source bottle provided homogeneously mixed, radon enriched xenon. This was confirmed by measuring the radon activity concentration of the source bottle at different filling levels.

Before each run, the radon activity concentration of the enriched xenon was determined by means of the radon monitor. For complementary measurements using proportional counters, a gas sample was taken from the sample port. Then, the radon enriched xenon was filled into the HeXe cryostat. The continuous xenon liquefaction at the cold-finger guaranteed that the pressure inside the cryostat staid constant. The Pre-filling preparation was the preferred procedure and was used in most of the runs. It avoided the exposure of the radon monitor to high activities and, in contrast to the In-situ preparation, no determination of the dilution factor is necessary to evaluate the radon activity of the liquid reservoir (see also section 3.4).

#### 3.2.2. Measurement of boil-off reduction

At the beginning of a run, the HeXe cryostat was filled with a certain amount of liquid xenon. The gas system and the radon monitor were evacuated and we immersed the recuperation bottle in liquid nitrogen. After the filling process we waited until an equilibrium established between the evaporating gas from the liquid reservoir and the xenon liquefaction at the cold finger of the cryostat. Depending on the filled xenon mass, the liquid level exceeded the bottom edge of the bell structure. In that case, the boil-off gas below the bell was separated from the gas inlet and the volume in contact with the cold-finger (see section 3.1). We started the measurement by expanding boil-off gas

	filled xenon mass [kg]	recup. flow [slpm]	prep. procedure	bell structure
xe_run1	$0.6 \pm 0.1$	static	in-situ	yes
xe_run2	$1.9 \pm 0.1$	static	in-situ	yes
xe_run3	$2.1 \pm 0.1$	0.50	pre-filling	yes
xe_run4	$2.7 \pm 0.1$	0.55	pre-filling	yes
xe_run5	$2.6 \pm 0.1$	0.55 and 3.50	pre-filling	no
xe_run6	$4.0 \pm 0.1$	0.50 and 8.00	pre-filling	no

**Table 3.1.:** Overview of the six runs presented in this work. The runs differ in filled xenon mass, in the adjusted recuperation flow but also in the pre- or absence of the bell structure inside the cryostat.

from the bell into the radon monitor. Then, we started the recuperation of the boil-off xenon from the cryostat with an adjusted mass flow through the radon monitor into the recuperation bottle. The radon activity concentration of the gas, the mass flow and the pressures inside the cryostat and the radon monitor were continuously monitored. During the recuperation process, a gas sample for proportional counter measurements was taken from the sample port. As we will discuss in section 3.3, the boil-off reduction factor is given by the ratio of the radon activity concentration of the boil-off gas and the activity concentration of the liquid phase. By means of the heating plate at the bottom of the cryostat (see section 3.1), it was possible to achieve flows of up to 8.0 slpm. In Table 3.1 we give an overview of the six runs presented in this work. Those runs differ in the initially filled xenon mass and the procedure of enriching xenon with radon. The bell structure has been removed in the last two runs to study its impact (see section 3.4). In the absence of the bell, the CCD camera was mounted at the top of the cryostat vessel. During the first two runs, the liquid xenon was not recuperated at a controlled mass flow. Instead, the radon activity concentration in the boil-off gas was measured static, i.e., we expanded boil-off xenon from the cryostat into the radon monitor and measured its activity without continuous gas flow through the detector. In xe\_run5 and xe\_run6 the measurements were started adjusting a mass flow of about 0.5 slpm to reproduce the results of previous runs. At the end of these runs, the recuperation flow was increased to 3.5 slpm and 8.0 slpm, respectively (see Table 3.1), to investigate the boil-off reduction factor at these conditions.

### 3.3. Data analysis

In Figure 3.4 the raw data of xe\_run4, as it was acquired by the radon monitor (Ra-Mon), is shown for illustration. The working principle and detection efficiency of the radon monitor has been discussed in section 2.3.1. For our data analysis, we only use  $^{218}\text{Po}$  events which have a short half-life of 3.1 min and thus allow for a reasonable time

### 3. Radon depletion in xenon boil-off gas

---

resolution in monitoring the evolution of the  $^{222}\text{Rn}$  concentration. The activity plateau at the beginning of the run corresponds to the radon enriched xenon gas initially filled to the HeXe cryostat. Therefore, we expanded xenon from the source bottle, via the system bypass (see Figure 3.2), directly into RaMon. At about  $t_0 = 110$  min, the recuperation of the boil-off gas started. The observed drop in the measured activity is already a clear indication for the radon reduction in the boil-off gas. As a second feature pointing towards boil-off reduction, we observe the activity increase throughout the recuperation phase, exceeding even the start activity. This evolution is explained by the accumulation of radon in the liquid reservoir. The red dashed lines in Figure 3.4 mark the times when gas samples were taken for measuring the activity of the initially filled gas (pipette 1) and of the boil-off gas (pipette 2) using proportional counters.

In this section, we want to discuss how we determine the boil-off reduction factor  $R$ , defined as the ratio of the radon concentrations in the liquid and gaseous xenon phase,

$$R \equiv \frac{c_l}{c_g} . \quad (3.1)$$

We introduce two different analyses. The *dynamic reduction analysis* investigates the boil-off reduction continuously throughout the run. Thus, it is sensitive to changes of  $R$  as a function of the mass of the liquid reservoir. This analysis is also adopted for analyzing the proportional counter measurements and to the so called static radon monitor measurements (see section 3.2.2).

The *constant reduction fit* analysis, on the other hand, assumes a constant  $R$  to describe the increasing activity of the recuperated xenon gas as observed in Figure 3.4. Since this analysis requires a constant recuperation mass flow, it is only applied in xe\_run3 and xe\_run4 (see Table 3.1).

#### 3.3.1. Dynamic reduction analysis

The  $^{218}\text{Po}$  activity  $A(t)$  of the boil-off xenon is continuously monitored during a run (see Figure 3.4). From this measurement we obtain the radon activity concentration in the gas phase,  $c_g(t)$ , as a function of time. The initially filled xenon mass and the totally filled activity at the beginning of the run are labeled  $M_0$  and  $A_0$ , respectively. Since the recuperation flow  $f(t)$  is known, we can use  $c_g(t)$  to determine the activity concentration of the liquid reservoir  $c_l(t)$ . Using both concentrations,  $c_g(t)$  and  $c_l(t)$ , we can investigate the boil-off reduction factor  $R$  as a function of time which corresponds also to the liquid xenon mass and  $c_l(t)$  due to the recuperation process.

Using the radon monitor's physical volume<sup>1</sup>  $V^D$  and the xenon gas density  $\rho_g^D(t)$  inside the monitor, the activity concentration in the gas phase is given by

$$c_g(t) = \frac{A(t)}{V^D \cdot \rho_g^D(t) \cdot \epsilon_{218}(\rho_g^D(t))} \cdot e^{\lambda_{Rn} \cdot (t - t_0)} . \quad (3.2)$$

---

<sup>1</sup>The superscript  $D$  emphasizes that this quantity is related to the radon detector.

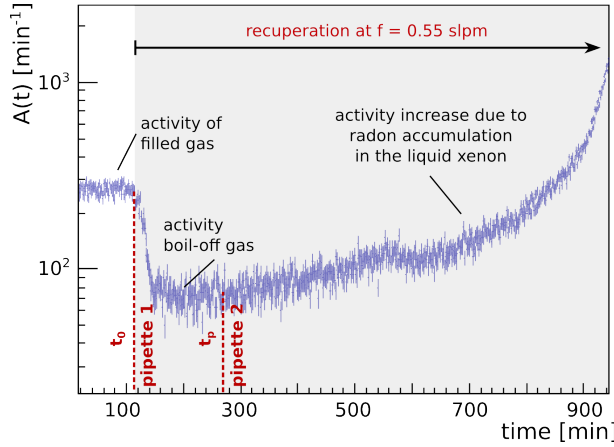


**Figure 3.4.:** Radon monitor data of a typical measurement (xe\_run4). The activity of the filled gas is clearly higher than of the recuperated boil-off gas. The observed increase of the activity concentration during recuperation is also used to determine the boil-off reduction factor  $R$ . Gas samples (pipette 1, pipette 2) are taken for complementary measurements using proportional counters.

The factor  $\epsilon_{218}(\rho_g^D(t))$  is the radon monitor's detection efficiency for  $^{218}\text{Po}$  decays introduced in section 2.3.1. It also accounts for the dependency of the efficiency on the gas density  $\rho_g^D(t)$ . Since the gas density is not necessarily constant during the measurement (e.g., changing pressures) also  $\epsilon_{218}(\rho_g^D(t))$  changes with runtime  $t$ . As a reference point to correct for the radon decay during the measurement we use  $t_0$  (recuperation start). This correction is expressed by the exponential factor in Eq. (3.2). The activity concentration of the initially filled xenon gas is labeled by  $c_0$  and is determined again using Eq. (3.2).

For the activity concentration in the liquid phase as a function of time we write

$$c_l(t) = \frac{A_l(t)}{M_l(t)} , \quad (3.3)$$

where  $A_l(t)$  is the absolute radon activity in the liquid xenon reservoir of mass  $M_l(t)$ . Both are dependent on the elapsed runtime  $t$  since we recuperate xenon from the cryostat during the run. Thus, the radon accumulates in the liquid due to the distillation process. The liquid xenon mass is given by

$$M_l(t) = M_0 - V_g^C \cdot \rho_g^C(t) - \int_{t_0}^t f(t') dt' . \quad (3.4)$$

The integral over the recuperation flow  $f(t)$  gives the recuperated xenon mass at the time  $t$ . As we show in Eq. (3.4), the total filled xenon mass  $M_0$  is not equivalent to the liquid xenon mass at the recuperation start  $M_l(t = t_0)$  due to the gas phase above the liquid reservoir inside the cryostat. We calculate the gaseous xenon mass by the product

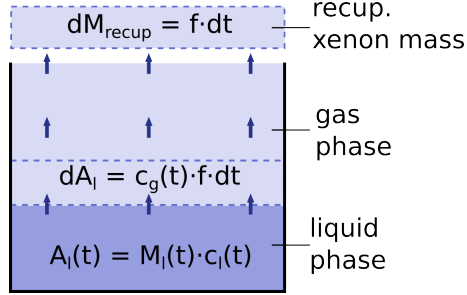


**Figure 3.5.:** Evolution of the absolute radon activity in the liquid phase  $dA_l(t)/dt$ . In the constant reduction fit analysis, we assume a constant  $R$  and a constant recuperation flow  $f$  and gas pressure inside the HeXe cryostat.

of the cryostat's physical volume  $V_g^C$  and the gas density  $\rho_g^C(t)$  inside the cryostat<sup>2</sup>. Due to the gas recuperation during the run, the gas volume increases with the decreasing liquid level. For the measurements discussed in this work, however, this effect was found to be  $< 1\%$  and can be neglected.

Analogously, we find for the absolute radon activity in the liquid xenon reservoir

$$A_l(t) = c_0 \cdot M_0 - c_g(t) \cdot V_g^C \cdot \rho_g^C(t) - \int_{t_0}^t c_g(t') \cdot f(t') dt' . \quad (3.5)$$

The first term determines the total radon activity initially filled into HeXe, while the second term represents the absolute activity in the gas phase inside the cryostat. The integral sums up the total activity which has been recuperated in the time between the recuperation start  $t_0$  and the time  $t$ . Together with Eq. (3.3), we can use the expressions found for  $M_l(t)$  and  $A_l(t)$  to determine the activity concentration in the liquid phase,

$$c_l(t) = \frac{c_0 \cdot M_0 - c_g(t) \cdot V_g^C \cdot \rho_g^C(t) - \int_{t_0}^t c_g(t') \cdot f(t') dt'}{M_0 - V_g^C \cdot \rho_g^C(t) - \int_{t_0}^t f(t') dt'} . \quad (3.6)$$

After inserting the expression obtained for  $c_g(t)$  and  $c_l(t)$  in Eq. (3.1), we find for the reduction factor

$$R(t) = \frac{c_0 \cdot M_0 - c_g(t) \cdot V_g^C \cdot \rho_g^C(t) - \int_{t_0}^t c_g(t') \cdot f(t') dt'}{c_g(t) \cdot \left( M_0 - V_g^C \cdot \rho_g^C(t) - \int_{t_0}^t f(t') dt' \right)} . \quad (3.7)$$

### 3.3.2. Constant reduction fit

In this analysis approach we determine the boil-off reduction factor  $R$  from the observed increase of the measured activity of the recuperated boil-off gas (see Figure 3.4). The rising evolution is explained by the accumulation of radon in the liquid xenon reservoir,

<sup>2</sup>The superscript  $C$  emphasizes that these quantities are related to the cryostat and not, e.g., to the radon monitor.

i.e. an increasing activity concentration in the liquid  $c_l(t)$ . In contrast to the dynamic reduction analysis, we assume an unknown, but constant reduction factor  $R$ . Consequently, the time evolution of  $c_l(t)$  is proportional to the measured evolution of  $c_g(t)$ . The boil-off reduction is then obtained from fitting the data acquired by the radon monitor.

In our fit model, we want to describe the evolution of the absolute radon activity in the liquid xenon phase  $A_l(t)$  as a function of time. As shown in Figure 3.5, we assume a homogeneous  $c_g(t)$  of the gaseous xenon inside the HeXe cryostat. Then, the time evolution of  $A_l(t)$  can be expressed by the differential equation

$$\frac{dA_l(t)}{dt} = -c_g(t) \cdot f . \quad (3.8)$$

At this point, we have simplified the analysis by assuming a constant recuperation flow  $f = \text{const}$  throughout the measurement. Thus, it can only be applied to xe\_run3 and xe\_run4. Using the definition of  $R \equiv c_l/c_g$  (Eq. (3.1)), the differential equation Eq. (3.8) rewrites as

$$\frac{dA_l(t)}{dt} = -\frac{c_l(t)}{R} \cdot f . \quad (3.9)$$

For the activity concentration in the liquid reservoir we extend Eq. (3.3) to

$$c_l(t) = \frac{A_l(t)}{M_l(t)} = \frac{A_l(t)}{M_l(t_0) - f \cdot (t - t_0)} . \quad (3.10)$$

We want to emphasize that the last equation implies a constant gas pressure in the boil-off phase (in contrast to the dynamic reduction analysis) which further restricts the applicability of the analysis. After inserting Eq. (3.10) into Eq. (3.8), we can solve the differential equation to

$$A_l(t) = (M_l(t_0) \cdot R - f \cdot R \cdot (t - t_0))^{1/R} \cdot C , \quad (3.11)$$

where  $C$  is an integration constant. We can insert  $A_l(t)$  in Eq. (3.10) which results in

$$c_l(t) = R^{1/R} \cdot (M_l(t_0) - f \cdot (t - t_0))^{1/R-1} \cdot C . \quad (3.12)$$

Since we have assumed a constant reduction factor  $R$  this can be transformed to

$$c_g(t) = R^{1/R-1} \cdot C \cdot (M_l(t_0) - f \cdot (t - t_0))^{1/R-1} , \quad (3.13)$$

using the definition Eq. (3.1). Above Eq. (3.13) is our model to fit the constant boil-off reduction factor  $R$  in the constant reduction fit analysis.

## 3.4. Results boil-off reduction

As discussed in section 3.2, we distinguish static runs, i.e., the xenon boil-off gas was expanded into the radon monitor and measured static, and runs where the liquid xenon

### 3. Radon depletion in xenon boil-off gas

---

reservoir was recuperated from the cryostat with a continuous gas flow through the radon monitor. The latter is referred to as recuperation measurements. Table 3.1 gives an overview about some important parameters of the single runs such as total filled xenon mass and recuperation flow. In the following, we will discuss the analysis of each run individually. The results of all runs will be summarized and discussed in section 3.6.

#### 3.4.1. Static measurements

Xe\_run1 and xe\_run2 are static measurements. In both runs, we prepared the radon enriched xenon according to the In-situ preparation procedure introduced in section 3.2. The analysis of the static measurements is done according to the dynamic reduction analysis but setting the recuperation flow to zero, i.e.,  $f = 0$  (by definition). Thus, Eq. (3.7) simplifies to

$$R = \frac{c_0 \cdot M_0 - c_g \cdot V_g^C \cdot \rho_g^C}{c_g \cdot (M_0 - V_g^C \cdot \rho_g^C)} , \quad (3.14)$$

where  $c_0$  is the  $^{222}\text{Rn}$  activity concentration of the radon enriched xenon gas initially filled into the cryostat.  $c_g$  labels the radon concentration of the boil-off gas which is measured statically by means of the radon monitor. The term  $V_g^C \cdot \rho_g^C$  gives the mass of the boil-off xenon inside the cryostat. As we discussed in section 3.3, we assume a constant gas volume which is  $V_g^C = (17.3 \pm 0.5)\text{l}$  (volume of cryostat). The density of the boil-off xenon is estimated for both static runs to be  $\rho_g^C = (7.6 \pm 1.8)\text{ g/l}$  at 1 bar xenon pressure. This average density has been determined from temperature measurements by means of the PT100 sensors placed inside the cryostat. In our analysis,  $\rho_g^C$  is scaled up/down according to the pressure measured inside the cryostat relative to the 1 bar reference. If not stated differently, the radon monitor was operated at  $-1.8\text{ kV}$ . For convenience, we measure the  $^{222}\text{Rn}$  activity concentrations in units of detected  $^{218}\text{Po}$  events per minute<sup>3</sup> when the radon monitor was filled with 1 bar of the sample gas. Since we are only interested in relative changes of the activity concentration, we don't account for the absolute detection efficiency  $\epsilon_{218}$ , but correct for its pressure dependence (see section 2.3.1).

#### xe\_run1 (27.11.2014):

Following the In-situ preparation of radon enriched xenon, we filled 32 sl xenon into the cryostat via the hot, radon loaded activated carbon trap. During this process the cold-head was switched off and the whole setup was at room temperature. After filling, we expanded some radon enriched gas from the cryostat into the evacuated radon monitor (RaMon) to measure its  $^{218}\text{Po}$  activity concentration  $\tilde{c}_0$  (upper level). Then, the cooling and thus xenon liquefaction was started and additional 68 sl, but now radon clean xenon was filled. The monitored mass-flow during filling is shown in Figure 3.6 (Left). In total we filled  $M_0 = (0.6 \pm 0.1)\text{ kg}$  xenon. From the ratio of the amount of xenon filled before

<sup>3</sup>We want to remind that we use  $^{218}\text{Po}$  events to determine the radon activity since the radon monitor cannot detect  $^{222}\text{Rn}$  directly.

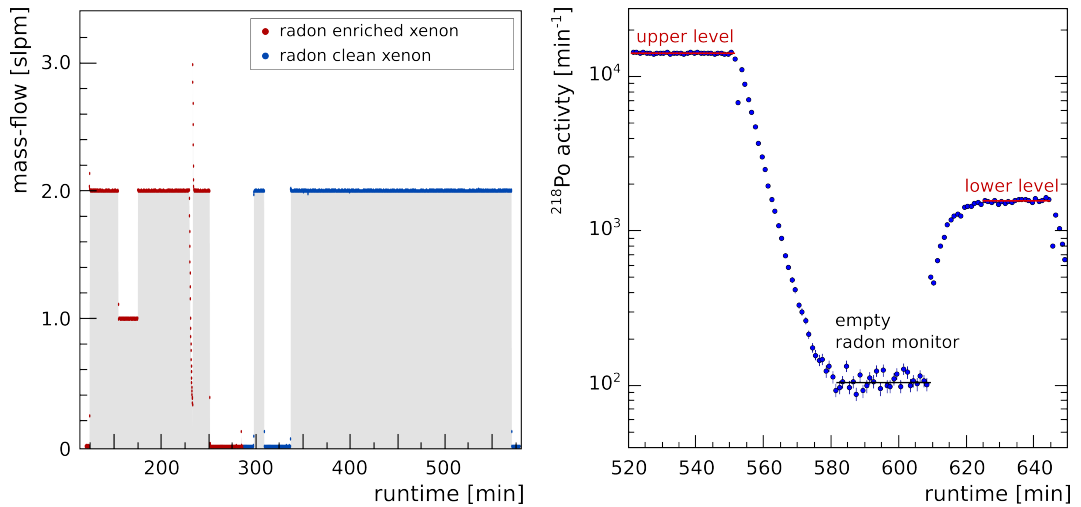


**Figure 3.6.:** (Left) Xenon mass-flow during the filling procedure of xe.run1. The dilution factor  $f_d$  is obtained from the ratio of radon enriched and radon clean xenon. (Right) Radon activity acquired by the radon monitor (before pressure correction). The reduction factor is determined from the ratio of the upper/lower activity levels.

cooling (red data points) and the total filled xenon mass, we determine the dilution factor  $f_d = (0.320 \pm 0.005)$ . After the filling process, we again expanded a sample of the boil-off gas into the radon monitor to measure its radon activity concentration (lower level). For both radon monitor measurements, upper and lower level, we took samples for the proportional counters directly from the monitor.

The measurements of the upper level  $\tilde{c}_0$  and the lower level  $c_g$  are shown in Figure 3.6 (Right) before pressure normalization. The levels are determined by a constant fit. Normalized to 1 bar sample gas inside RaMon we measured the  $^{218}\text{Po}$  activity concentrations of  $\tilde{c}_0 = (109.4 \pm 2.3) \text{ kBq/kg}$  and  $c_g = (11.24 \pm 0.17) \text{ kBq/kg}$  for the upper and lower level, respectively. After measuring the upper level, the radon monitor was emptied while we continued data taking (HV was switched off in order to avoid electric discharges). As expected, the  $^{218}\text{Po}$  rate decreases with time but levels off at a rate of  $(105.7 \pm 1.8) \text{ min}^{-1}$  (see Figure 3.6). This is explained by leakage from the higher energetic  $^{214}\text{Po}$  decays into the  $^{218}\text{Po}$  event selection window. While measuring the upper level, the number of atoms drifted onto the radon monitor's PIN diode was similar for both polonium isotopes. In that phase, the leakage was  $< 1\%$  and thus negligible. After emptying RaMon, however, the  $^{214}\text{Po}$  decayed with a half-life of about  $t_{1/2} = 60 \text{ min}$ , i.e., 20 times slower than  $^{218}\text{Po}$ . Due to residual  $^{214}\text{Po}$  from the upper level measurement, the leakage into the  $^{218}\text{Po}$  event selection window was found to contribute up to 3-4% to the lower level  $c_g$ . As shown in Figure 3.7 (Right), the leakage was determined by fitting a Crystal-Ball function [68] (see also Table 2.2) to the energy spectrum. Using Eq. (3.14), we find for

### 3. Radon depletion in xenon boil-off gas

---

the reduction factor

$$R = \frac{\overbrace{\tilde{c}_0 \cdot f_d \cdot f_t \cdot M_0 - c_g \cdot V_g^C \cdot \rho_g^C}^{c_0}}{c_g \cdot (M_0 - V_g^C \cdot \rho_g^C)} = 3.4 \pm 0.2_{\text{stat}}^{+0.5}_{-0.2} \text{ syst} \quad (\text{radon monitor}), \quad (3.15)$$

where  $f_d$  is the dilution factor and  $f_t$  corrects for the radioactive decay in the time period between the measurements of the upper and lower level, respectively. The radon concentration after dilution and time correction is given by  $c_0 = \tilde{c}_0 \cdot f_d \cdot f_t = (35.0 \pm 0.5) \text{ kBq/kg}$ . The statistical error of  $R$  comes from the activity measurements and is determined according to counting statistics. The systematical error is dominated by the uncertainties of the mass  $M_0$  and the estimated xenon mass of the boil-off gas inside the cryostat (i.e., the term  $V_g^C \cdot \rho_g^C$ ). To determine the systematical error, we used the maximal and minimal value obtained for  $R$ , respectively, when varying the systematic quantities (i.e.,  $M_0$ ,  $V_g^C$ ,  $\rho_g^C$ ) within their error bands given in this work.

The gas samples for the proportional counters have been taken directly from the radon monitor. In order to transfer the sample into the counter, the sample vessels have been connected directly to the counter-filling facility. For the activity measurements in this run, we count the number of  $\alpha$ -decays<sup>4</sup> from radon and its progenies within a chosen time window after filling the sample into the counter. The  $\alpha$ -activity concentration of the upper level was measured to be  $(184 \pm 10) \text{ kBq/kg}$  having filled  $(0.95 \pm 0.05) \cdot 10^{-3} \text{ sl}$  of sample into the proportional counter. For the lower level we obtained  $(17.5 \pm 2.0) \text{ kBq/kg}$  for  $(0.94 \pm 0.05) \cdot 10^{-3} \text{ sl}$  of gas. A correction factor  $f_t$  is used in order to account for the radioactive decay since the upper and lower level couldn't be measured simultaneously. In order to determine the reduction factor  $R$ , we use Eq. (3.14), similar as we did for the radon monitor measurement. We obtain:

$$R = \frac{\overbrace{\tilde{c}_0 \cdot f_d \cdot f_t \cdot M_0 - c_g \cdot V_g^C \cdot \rho_g^C}^{c_0}}{c_g \cdot (M_0 - V_g^C \cdot \rho_g^C)} = 4.11 \pm 0.54_{\text{stat}}^{+0.25}_{-0.21} \text{ syst} \quad (\text{prop. counter}) \quad (3.16)$$

#### **xe\_run2 (18.02.2015):**

This measurement is similar to xe\_run1. We filled 33.5 sl radon enriched xenon gas into the warm cryostat. After switching on the cold head, we added 345 sl radon-clean xenon. This results in a dilution factor of  $f_d = (0.0971 \pm 0.0016)$  and a total filled xenon mass of  $M_0 = (1.9 \pm 0.1) \text{ kg}$ . After dilution, the activity concentration of the filled gas is calculated to be  $c_0 = (9.69 \pm 0.22) \text{ kBq/kg}$ .

Normalized again to the gas amount inside the radon monitor at 1 bar pressure, we find  $\tilde{c}_0 = (99.9 \pm 1.5) \text{ kBq/kg}$  for the upper level  $^{218}\text{Po}$  activity concentration. Similarly to xe\_run1, we waited for about one hour after filling the total xenon mass  $M_0$  in order to let the system equilibrate. Then, we expanded gas from the boil-off gas into the evacuated radon monitor in order to measure the lower level of  $c_g = (2.40 \pm 0.05) \text{ kBq/kg}$ . As

<sup>4</sup>The used proportional counters cannot resolve the high energetic  $\alpha$ -decays from radon and its progenies.

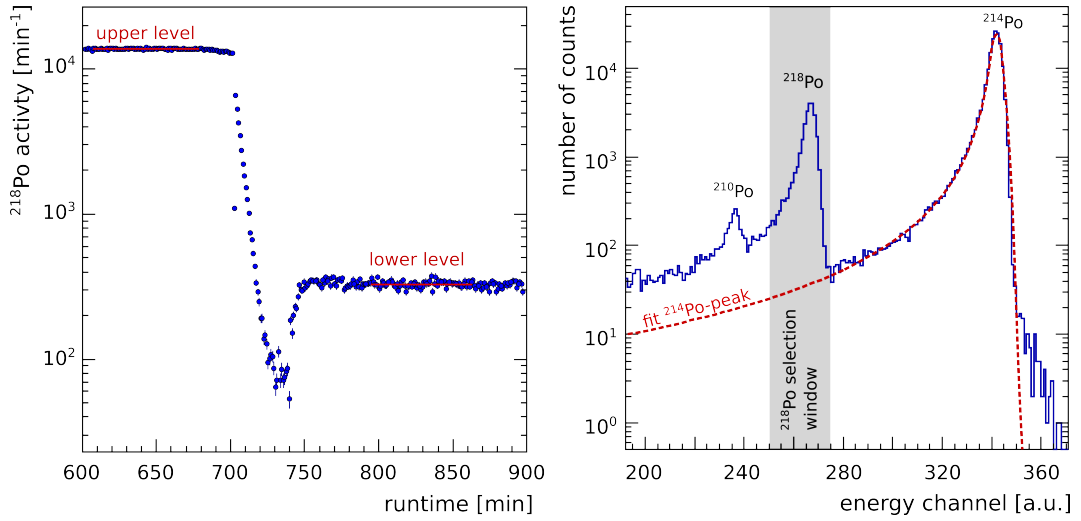


**Figure 3.7.:** (Left) Determination of the upper and lower  $^{218}\text{Po}$  activity levels for xe\_run2 (before pressure correction). The dip in the activity evolution origin from evacuating the radon monitor between the two measurements. (Right) The leakage of  $^{214}\text{Po}$  events into the  $^{218}\text{Po}$  event selection window was estimated by fit.

we discussed in xe\_run1, we need to account for the leakage of  $^{214}\text{Po}$  events into event selection window. Both, the upper and lower level are determined by a constant fit. We obtain for the reduction factor:

$$R = 4.63 \pm 0.21_{\text{stat}}^{+0.10} {}_{-0.07}^{\text{syst}} \quad (\text{radon monitor}) \quad (3.17)$$

Similar as in xe\_run1, we took gas samples for proportional counter measurements for the upper and lower level from the radon monitor. Having filled  $(0.931 \pm 0.033)$  sl of sample gas, the upper level had an  $\alpha$ -activity concentration of  $(178 \pm 8)$  kBq/kg. For the lower level we measured  $(3.4 \pm 0.6)$  kBq/kg for  $(0.826 \pm 0.027)$  sl of sample gas. From Eq. (3.16) we find for the reduction factor:

$$R = 5.29 \pm 0.86_{\text{stat}}^{+0.11} {}_{-0.09}^{\text{syst}} \quad (\text{prop. counter}) \quad (3.18)$$

### 3.4.2. Recuperation measurements

The remaining runs (xe\_run3 to xe\_run6) are dynamic measurements, i.e., we determined the reduction factor as a function of time during the recuperation phase by means of Eq. (3.7). In xe\_run3 and xe\_run4, the recuperation flow was kept constant. Here, we can apply the constant fit analysis as introduced in section 3.3. If not stated differently, the radon monitor was operated at  $-1.8$  kV. For all dynamic measurements we followed the Pre-filling preparation procedure (see section 3.2) in order to prepare radon enriched xenon.

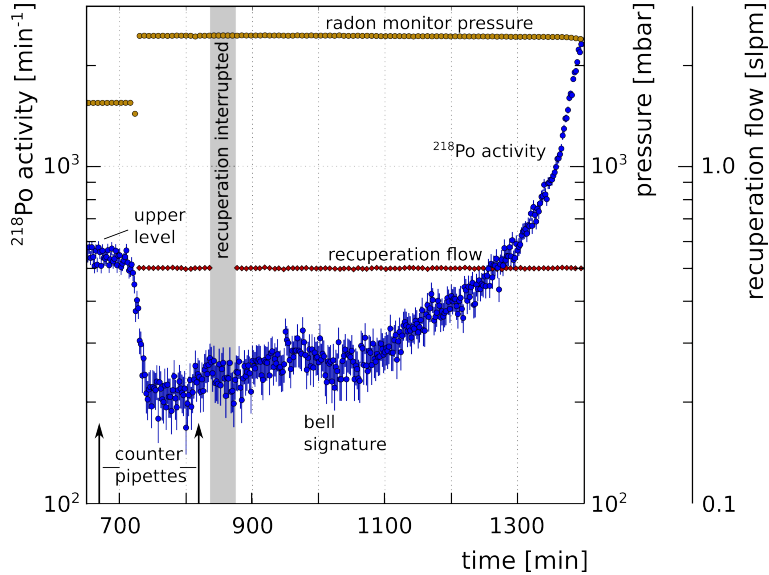


**Figure 3.8.:** Monitored  $^{218}\text{Po}$  activity acquired with the radon monitor in xe.run3. The upper level refers to the activity concentration of the initially filled xenon gas. At about  $t_0 = 720$  min recuperation started. The pressure and recuperation flow were monitored throughout the run. At the moment when the liquid xenon surface falls below the bell structure we observe a dip in the activity evolution referred to as bell signature.

#### xe\_run3 (05.03.2015):

We filled in total  $M_0 = (2.1 \pm 0.1)$  kg of radon enriched xenon. Thus, the liquid level was above the bottom edge of the bell structure which was present in this run. Figure 3.8 shows the evolution of the  $^{218}\text{Po}$  activity (blue data points), the pressure inside the radon monitor (golden circles) and the mass flow (red diamonds) during the run. The radon activity concentration of the filled gas,  $c_g(t_0)$  was measured by both, the radon monitor and proportional counters (labeled as upper level). For the liquid xenon reservoir, we calculate an activity concentration of  $c_l(t_0) = (4.50 \pm 0.09)$  kBq/kg at the beginning of the run and using Eq. (3.6). At about  $t_0 = 720$  min, we started the recuperation of the boil-off gas with a constant mass-flow of  $f = (0.500 \pm 0.005)$  slpm. While measuring the upper level, the radon monitor was operated statically at a pressure of about 1.6 bar. The pressure increased to 2.5 bar at the start of the run, as soon as the radon monitor got connected to the cryostat. As we discussed in section 3.3, the changing pressure conditions, but also the related change of the detector efficiency (see chapter 2) is taken into account when evaluating the reduction factor. We took gas samples from the initially filled gas and during the run for proportional counter measurements (marked with arrows in Figure 3.8). At  $t = 820$  min, the recuperation was interrupted. During that time, the radon monitor's outlet was closed while the gas inlet stayed connected to the cryostat. After about 40 min, recuperation was restarted with the same flow as before. At about  $t = 1000$  min, we see a dip in the measured activity which is not related to any evolution in the pressure or recuperation flow. From observation of the liquid xenon surface using

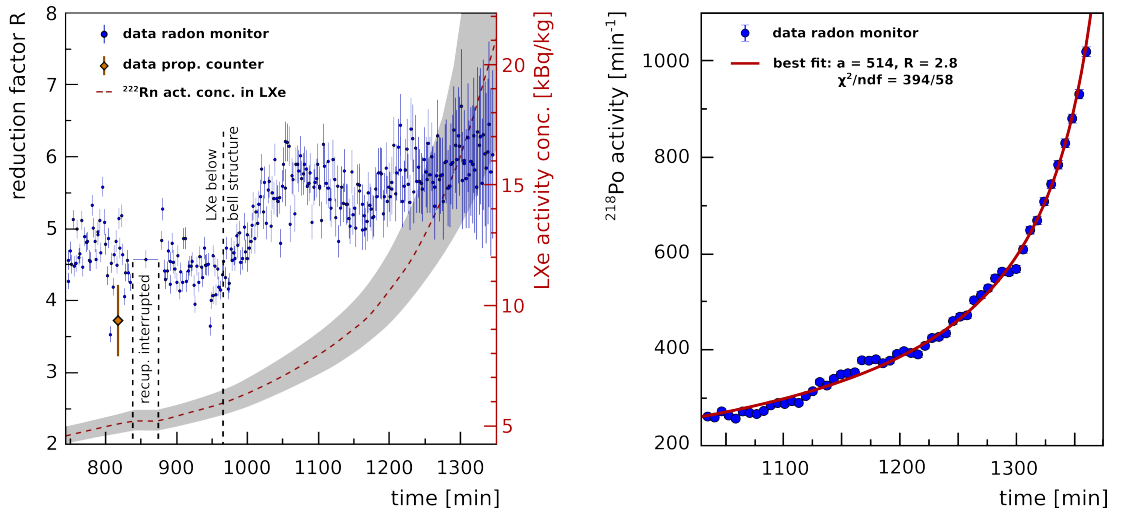


**Figure 3.9.:** (Left) The reduction factor  $R$  as obtained from the monitored  $^{218}\text{Po}$  activity using Eq. (3.7). (Right) Fit of the constant reduction model, Eq. (3.13), to radon monitor data.

the CCD-camera, we noticed that this signature correlates with the liquid level falling below the bell structure. The impact of this bell signature will be discussed later. In Figure 3.9 (Left), we show the reduction factor  $R$  as a function of time determined using Eq. (3.7). Since we recuperate the xenon with a constant mass-flow, the time axis correlates to the liquid xenon mass inside the cryostat. Until  $t = 825$ , we measured an average reduction factor of:

$$R = 4.61 \pm 0.02_{\text{stat}}^{+0.29}_{-0.27} \text{ syst} \quad (\text{radon monitor})$$

Only the statistical errors are shown in Figure 3.9 (Left). The dominating systematic errors are driven by uncertainties of the mass flow but also on the xenon density used to determine the mass of the boil-off gas (see section 3.3). The systematical errors have been determined using the maximal and minimal values obtained for  $R$ , respectively, when varying the systematic quantities (i.e.,  $M_0$ ,  $V_g^C$ ,  $\rho_g^C$ ,  $f$ ) within their error bands given in this work. The leakage of  $^{214}\text{Po}$  events into our  $^{218}\text{Po}$  event selection window was found to be  $< 1\%$  in all dynamic runs and is thus neglected. The complementary measurement using proportional counters gives a slightly lower reduction factor of

$$R = 3.75 \pm 0.50_{\text{stat}}^{+0.08}_{-0.06} \text{ syst} \quad (\text{prop. counter}) ,$$

according to the analysis introduced in Eq. (3.16). Thereby, we neglect the effect of the gas recuperation between the two gas pipettes. It was found to be negligible since the boil-off gas sample has been taken shortly after the recuperation start. As a consequence, the systematic errors for the proportional counter measurement is lower with respect to the recuperation measurements employing the radon monitor.

At  $t = 1000$  min, we observe an increase of  $R$ , correlated with the bell signature which

### 3. Radon depletion in xenon boil-off gas

---

is also visible in Figure 3.8. The averaged reduction factor after the bell signature, i.e., after  $t = 1050$  min, is obtained to be:

$$R = 5.58 \pm 0.02_{\text{stat}}^{+0.88}_{-0.68} \text{syst} \quad (\text{radon monitor})$$

Since the systematic errors effect both values for  $R$  (before and after the bell signature) in the same direction, these two measurements of the reduction factor do not agree within their uncertainties. Possible explanations are given in the subsequent section 3.6. In Figure 3.9 (Left), we also show the activity concentration of the liquid phase,  $c_l(t)$ , as a function of time (red, dashed line).  $c_l(t)$  is calculated using Eq. (3.12) and increases by a factor of 10 during the recuperation process due to the accumulation of radon in the liquid xenon. The reduction factor  $R$  showed no significant dependence on  $c_l(t)$ . Since the recuperation flow was constant, we can alternatively analyze xe\_run3 using the constant reduction fit method (see section 3.3). Figure 3.9 (Right) shows the fit of Eq. (3.13) to the data after the bell signature<sup>5</sup>. As a best fit we obtain

$$R = 2.9 \pm 0.1_{\text{stat}}^{+2.0}_{-1.0} \text{syst} \quad (\text{const. reduction fit})$$

According to the reduced chi-square  $\chi^2/ndf = 394/58$ , our model of a constant reduction factor doesn't describe the data well. In fact, we find a second dip in the evolution of  $R$  in Figure 3.9 (Left) at about  $t = 1150$ . Also, we seem to underestimate the errors of the single data points. The large systematic errors of  $R$  have been determined similarly as we did for the radon monitor measurements. They are dominated by the uncertainties of the mass flow and the liquid xenon mass. Since the systematics of the dynamic reduction analysis and the constant reduction fit effects the obtained  $R$  in opposite directions (anti-correlated), both results for the reduction factor are not in tension with each other.

#### xe\_run4 (30.03.2015):

Xe\_run4 was performed identically to xe\_run3. We filled the cryostat with a total xenon mass of  $M_0 = (2.7 \pm 0.1)$  kg. The bell structure was present also in this run. We determined an activity concentration of  $c_l(t_0) = (1.76 \pm 0.03)$  kBq/kg for the liquid xenon reservoir at the recuperation start. Figure 3.10 shows the evolution of the  $^{218}\text{Po}$  activity (blue data points), the pressure inside the radon monitor (golden circles) and the mass flow (red triangles) during the run. Before the recuperation start at  $t_0 = 110$  min, we measured the activity concentration of the radon enriched gas from the source bottle (upper level). At about  $t = 100$  min, we opened the valve towards the cryostat and the pressure increased to about 1.8 bar (i.e., the cryostat pressure). The recuperation flow was first set to 0.50 slpm but then readjusted to  $f = 0.55$  slpm for the rest of the run. The  $^{218}\text{Po}$  activity of the recuperated boil-off xenon was continuously monitored. Similarly to xe\_run3, we observe a dip in the activity evolution at  $t = 600$ , the time, when the liquid level falls below the bottom edge of the bell structure (bell signature in Figure 3.10). For the proportional counter measurements, we took gas samples from the

---

<sup>5</sup>For the period before the bell signature we don't have enough statistics in order to obtain a meaningful result.

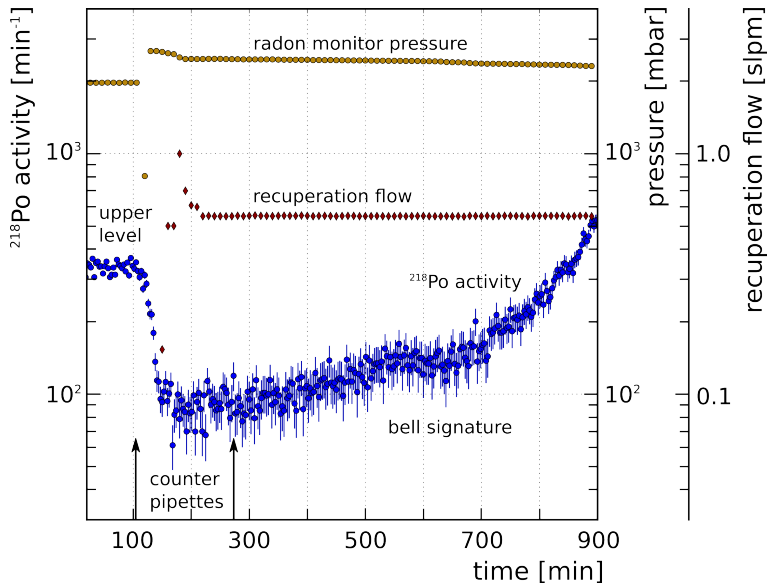


**Figure 3.10.:** Overview of xe\_run4. After measuring the activity concentration of the initially filled gas (upper level) we started recuperation at  $t = 110$  min. Similar to xe\_run3 we observe the bell signature at  $t = 600$  min.

initially filled gas and during the run (indicated by the black arrows in Figure 3.10). The inferred reduction factor  $R$ , using the dynamic reduction analysis, is shown in Figure 3.11 (Left). The systematic errors are not shown in the figure. We distinguish again between the reduction factor before and after the bell signature. At the beginning of the run, we measured an average reduction factor of:

$$R = 5.27 \pm 0.05_{\text{stat}}^{+0.22} {}_{-0.27}^{\text{syst}} \quad (\text{radon monitor})$$

This value is in good agreement with the proportion counter measurement:

$$R = 4.91 \pm 0.68_{\text{stat}}^{+0.07} {}_{-0.05}^{\text{syst}} \quad (\text{prop. counter})$$

For times larger than  $t = 600$  min, i.e., after the bell signature, we find a significant higher level for the reduction factor of:

$$R = 6.02 \pm 0.04_{\text{stat}}^{+1.12} {}_{-0.78}^{\text{syst}} \quad (\text{radon monitor})$$

Apart from the very beginning of the measurement, the recuperation flow was constant throughout the run. Thus, we can apply the constant reduction fit analysis. Motivated by the bell signature, we split the run and applied the constant reduction fit to the data before and after the bell signature separately. Figure 3.11 (Right) shows the fit before the bell signature. We obtain

$$R = 4.2 {}_{-0.5}^{+1.0} {}_{-0.7}^{+3.6} \quad (\text{const. reduction fit}) ,$$

### 3. Radon depletion in xenon boil-off gas

---

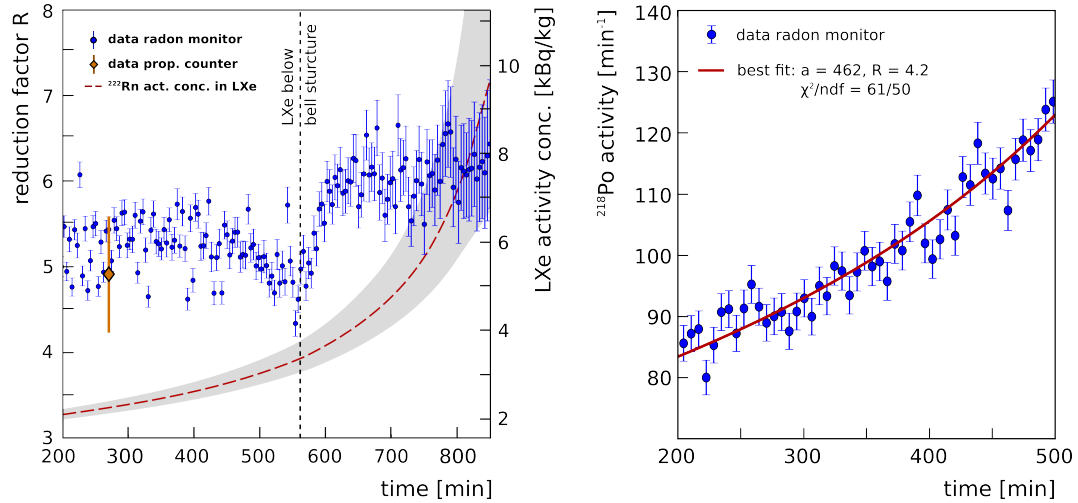


**Figure 3.11.:** (Left) The reduction factor as a function of time as obtained from dynamic reduction analysis. The bell signature is clearly visible. (Right) Fit of the activity increase before the bell signature as described by the constant reduction fit analysis.

achieving  $\chi^2/\text{ndf} = 61/50$ . The fit to the data after the bell structure gives as a best fit

$$R = 4.7_{-0.3}^{\text{stat}} {}^{+0.2}_{-2.0} \text{syst} \quad (\text{const. reduction fit}) \quad ,$$

achieving  $\chi^2/\text{ndf} = 56/38$ . Both results are in agreement to the corresponding values obtained in the dynamic reduction analysis.

#### xe\_run5 (13.05.2015):

In contrast to the previous runs, the bell structure was absent in this measurement. We started after having filled a total xenon mass of  $M_0 = (2.6 \pm 0.1)$  kg and a  $^{218}\text{Po}$  activity concentration in the liquid reservoir of  $c_l(t_0) = (1.22 \pm 0.02)$  kBq/kg. As shown in Figure 3.12, we started the xenon recuperation at about  $t_0 = 450$  min with a flow of  $f = 0.5$  slpm. Again, gas samples were taken for complementary measurements using proportional counters. At  $t = 515$  min we increased the recuperation flow. In order to keep the pressure constant, we made use of the heating plate at the bottom of the cryostat (see section 3.1). We stabilized the system at a recuperation flow of  $f = 3.5$  slpm by introducing an additional heating power of about 37 W. In section 2.3.1, we discussed a flow dependence of the radon monitor's detection efficiency. At 3.5 slpm this correction is negligible and thus omitted in xe\_run5.

In the absence of the bell structure, we do not see any significant changes of the reduction factor  $R$  shown in Figure 3.14 (Left). Only the statistical errors are displayed. For the time interval between  $t = 450$  min and  $t = 620$  min we measured an average value of:

$$R = 7.20 \pm 0.04_{\text{stat}} {}^{+0.50}_{-0.31} \text{syst} \quad (\text{radon monitor}) \quad ,$$

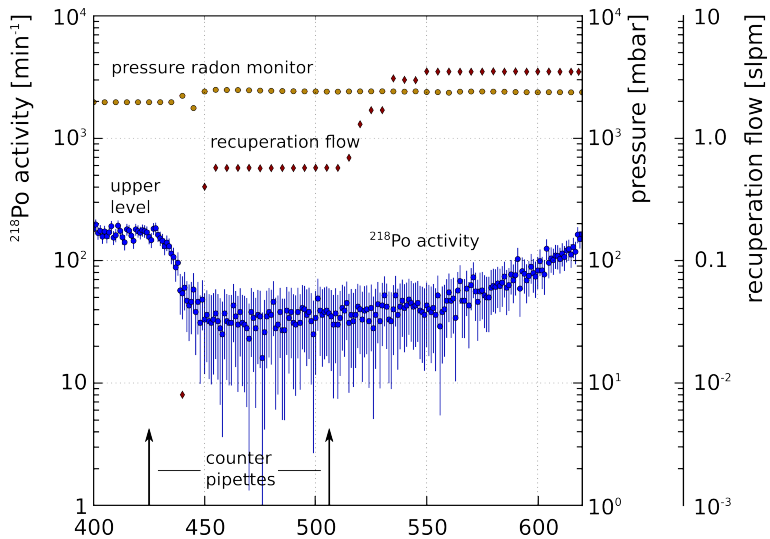


**Figure 3.12.:** Overview of xe\_run5. In this run, no bell structure was installed. Having started recuperation with a mass flow of 0.5 slpm, we increased the flow to 3.5 slpm at about  $t = 515$  min.

during the phase of  $f = 0.5$  slpm. This result is confirmed by proportional counter measurements:

$$R = 8.12 \pm 1.35_{\text{stat}}^{+0.13}_{-0.10} \text{ syst} \quad (\text{prop. counter})$$

After increasing the recuperation flow to  $f = 3.5$  slpm we measured:

$$R = 6.84 \pm 0.08_{\text{stat}}^{+1.06}_{-0.68} \text{ syst} \quad (\text{radon monitor})$$

Since the measurement at  $f = 3.5$  slpm was done at a later phase in xe\_run5, the systematic errors are larger for this measurement. This is explained by the increasing uncertainty on the mass of the liquid xenon reservoir. We did not observe any significant effect on the reduction factor  $R$  due to the changed recuperation flow at about  $t = 515$  min or the increasing activity concentration in the liquid phase (red dashed line in Figure 3.14).

### xe\_run6 (15.05.2015):

In the last run, we filled in total  $M_0 = (4.0 \pm 0.1)$  kg xenon. The activity concentration in the liquid reservoir was determined to be  $c_l(t_0) = (0.87 \pm 0.02)$  kBq/kg at the recuperation start. Similar to xe\_run5, no bell structure was present. In this run, the radon monitor was operated at a lower voltage ( $-1.6$  kV) due to the appearance of yet unexplained discharges. We determined the pressure dependence of  $\epsilon_{218}$ , discussed in section 2.3.1, for the altered drift field.

An overview of xe\_run6 is shown in Figure 3.13. At about  $t_0 = 595$  min, we started the measurement adjusting a recuperation flow of  $f = 0.5$  slpm. These conditions were kept stable until  $t = 680$  min. Then, we increased the flow to  $f = 6.0$  slpm for about 30 min.

### 3. Radon depletion in xenon boil-off gas

---

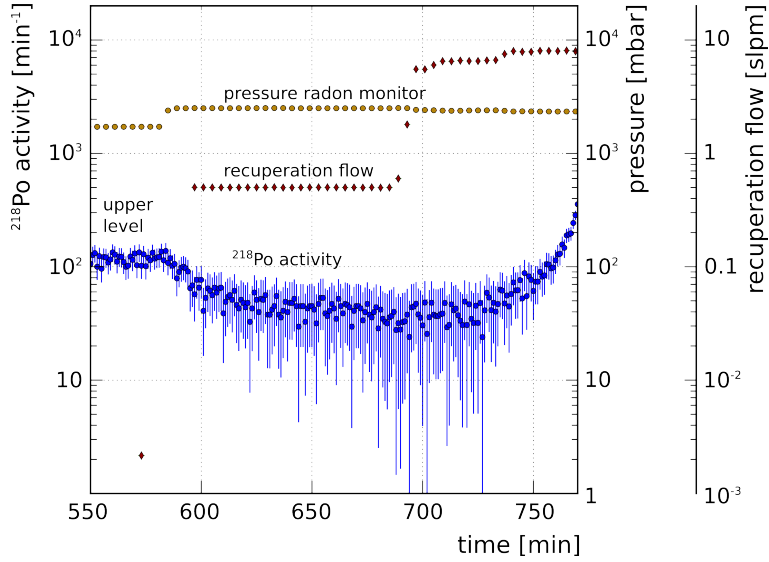


**Figure 3.13.:** Overview of xe\_run6. In this run no bell structure was installed. At about  $t = 680$  min we increased the recuperation flow up to 8.0 slpm.

Similar to xe\_run5, we used the heating plate at the bottom of the cryostat, providing a power of about 70 W, to keep the flow stable. At about  $t = 730$  min, we increased the heating power to 90 W in order to achieve a stable recuperation flow of  $f = 8.0$  slpm. The results obtained from the dynamic reduction analysis are shown in Figure 3.14. We can clearly separate between two phases: before and after increasing the recuperation flow. At  $f = 0.5$  slpm, we observe a constant reduction factor in the time interval between  $t = 615$  min and  $t = 680$  min of:

$$R = 3.77 \pm 0.09_{\text{stat}}^{+0.12}_{-0.13} \text{ syst} \quad (\text{radon monitor})$$

As soon as we increased the recuperation flow, also the reduction factor increased. Between  $t = 700$  min and  $t = 750$  min, we determined an average reduction factor of:

$$R = 5.47 \pm 0.15_{\text{stat}}^{+0.98}_{-0.98} \text{ syst} \quad (\text{radon monitor})$$

Thereby, we don't distinguish between the phases where  $f = 6.0$  slpm and  $f = 8.0$  slpm were adjusted. In section 2.3.1, we describe a dependence of the detection efficiency  $\epsilon_{218}$  on the purge flow. To account for this effect, we used a linear fit to the data as shown in Figure 2.6 (Right). We want to emphasize, however, that the flow dependence was only investigated while operating the radon monitor at a bias voltage of  $-1.8$  kV. Thus, the higher value obtained for  $R$  at recuperation flows greater than 6 slpm might be explained by an insufficient correction of the detection efficiency at the lower voltage setting of  $-1.6$  kV.

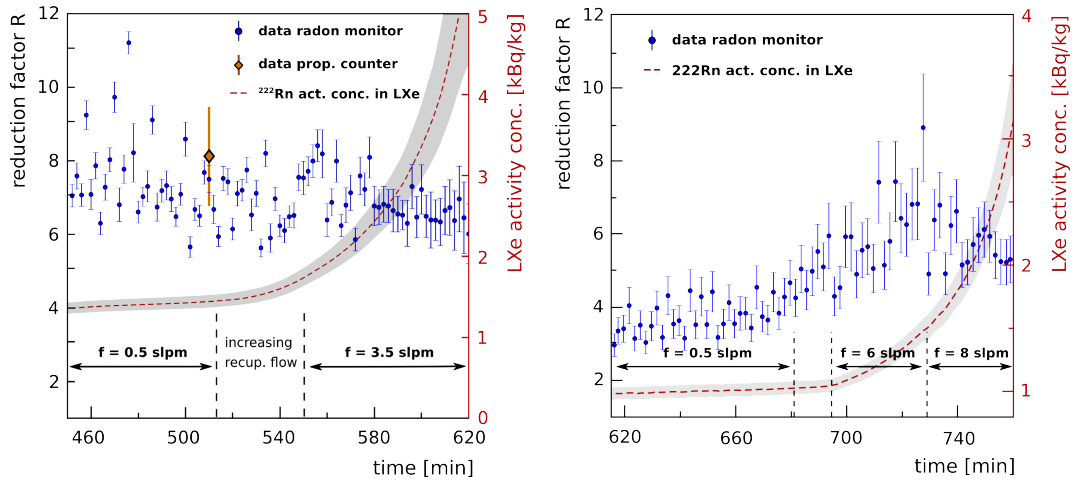


**Figure 3.14.:** (Left) Evolution of the reduction factor in xe\_run5 according to the dynamic reduction analysis. No bell signature is visible in this run. The increase of the recuperation flow to  $f = 3.5 \text{ slpm}$  seems to have no impact on  $R$ . (Right) In xe\_run6, the reduction factor seems to increase for higher recuperation flows.

### 3.4.3. Argon measurements

In preparation of the xenon runs, we performed two measurements using liquid argon. These tests were primarily meant to proof the setup's stability at cryogenic temperatures. However, one argon run is also suitable to determine the radon depletion in boil-off argon with respect to the liquid argon reservoir.

For the measurement, we prepared radon enriched argon following the Pre-filling preparation method described in section 3.2. The bell structure was present. In total, we filled  $M_0 = (6.5 \pm 0.2) \text{ kg}$  argon into the cryostat. The activity concentration of the liquid phase at the start of the run was  $c_l(t_0) = (0.84 \pm 0.07) \text{ kBq/kg}$ . The measurement of the boil-off reduction was done statically and is shown in Figure 3.15 (Left) (activity is not pressure corrected). Following the analysis introduced in section 3.4.1, we find for the upper level  $c_0 = (0.847 \pm 0.014) \text{ kBq/kg}$  and  $c_g = (0.037 \pm 0.002) \text{ kBq/kg}$ . Since we followed the Pre-filling preparation method, we don't need to consider the dilution factor  $f_d$ . For the argon gas density inside the cryostat we estimate  $\rho_g^C = (2.3 \pm 0.5) \text{ g/l}$  using the PT100 sensors to determine the gas temperature inside the cryostat. From Eq. (3.14), we derive for the boil-off reduction factor

$$R = 23.24 \pm 1.28_{\text{stat}}^{+0.05} {}_{-0.04}^{\text{syst}} \quad (\text{radon monitor}) \quad . \quad (3.19)$$

Due to the higher vapor saturation pressure of argon we expect an increased reduction factor with respect to the xenon measurements. In fact, according to our discussion presented in section 2.4.1 an  $R \sim 1 \cdot 10^8$  is predicted. Reasons for the lower reduction factor obtained in our run haven't been further investigated. For a similar discussion concerning our results obtained in the xenon runs, we want to refer to the following section 3.6.

### 3. Radon depletion in xenon boil-off gas

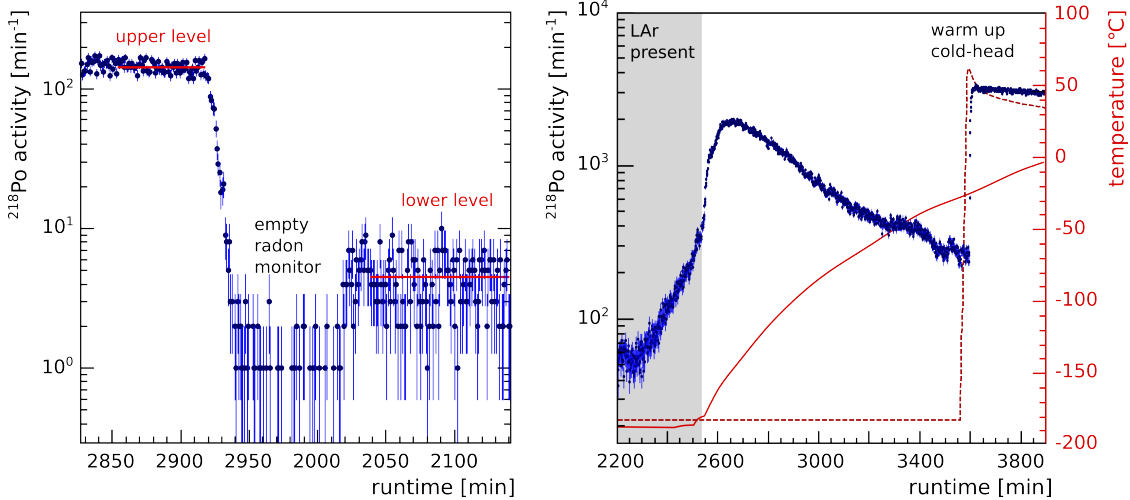


**Figure 3.15.:** (Left) The  $^{218}\text{Po}$  activity acquired by the radon monitor during the argon run. The upper and lower level are determined by a constant fit. No pressure correction has been applied to the shown data. (Right) Evolution of the  $^{218}\text{Po}$  activity (blue data points) and the temperatures in the cryostat (red solid line) and at the cold finger (red dashed line). The increased activity after warming up the cold finger is an indication for radon freeze-out during the argon measurement.

We found strong indication that radon was frozen out at the cold-head during the argon run. Figure 3.15 (Right) shows the last phase of the argon measurement. The blue markers refer to the  $^{218}\text{Po}$  activity monitored by the radon monitor. Also shown are the temperatures at the bottom of the cryostat (red solid line) and in the cold finger (red dashed line). During the run, we continuously flushed argon from the cryostat through the radon monitor before it was released to atmosphere. Similarly to the xenon measurements, the monitored activity concentration increased with the decreasing liquid argon reservoir. Since the CCD camera inside the bell did not work at liquid argon temperatures, the disappearance of the liquid phase is only indicated by the increasing temperature at the bottom of the cryostat (at about runtime 2540 min). The higher temperature value measured at the cold finger with respect to the cryostat is explained by the PT100's position between the cold finger's surface where argon liquefaction takes place and the heating cartridges. After all liquid argon has been evaporated, the gas volume inside the cryostat was slowly warming up while the cold finger was kept at liquefaction temperature. The overpressure, due to the expanding argon gas, was released via the radon monitor to atmosphere. In Figure 3.15 (Right), we observe a decreasing radon activity concentration during that time period. At about runtime  $t = 3550$  min, we closed the cryostat and heated the cold finger up to more than  $50^\circ\text{C}$ . In order to mix the gas inside the cryostat, we let build up some pressure which was then released via the radon monitor. The same procedure was repeated for several times. Then, a gas sample was filled from the cryostat into the radon monitor and its activity was measured statically. The increased radon activity measured after warming up the cold finger is

a strong indication for radon freeze-out during the argon run. Similar measurements performed after the xenon runs did not show this behavior. We conclude that due to the presence of xenon or simply due to the warmer liquid xenon temperatures with respect to liquid argon, radon did not stick to the cold surfaces as it was observed in the argon run.

### 3.5. On the vapor pressure of radon

In section 2.4.2, we estimated the radon reduction in boil-off xenon after a single distillation step. According to Raoult's law, the reduction factor in the limit of negligible amounts of radon with respect to xenon, is given by the ratio of the vapor pressures of xenon and radon, respectively (see appendix B). Thus, we can use our boil-off reduction results to determine the vapor pressure of radon at liquid xenon temperatures.

In the following, we use only the reduction factors  $R$  obtained by means of the radon monitor when no bell structure was present (static measurements and dynamic measurements at 0.5 slpm). To our understanding, this scenario is closest to an undisturbed system (see discussion in the following section 3.6). The averaged reduction factor is  $R = (5.2 \pm 2.5)$ . To account for the fluctuations of  $R$  between the single measurements, we increased the error to cover also the lowest/largest reduction factors found in the considered runs. For the vapor pressure of xenon we use our pressure monitoring inside the cryostat. We determine a radon vapor pressure of  $P_{Rn} = (0.43 \pm 0.20)$  bar at 180 K. Figure 3.16 shows the available experimental data including our result (blue data point). The oldest, nevertheless most reliable measurements have been performed by Gray and Ramsay [78] (triangles). They used about 0.1 mm<sup>3</sup> (at 0°C and 1 atmosphere) of radon gas and measured the vapor pressure directly after liquefaction. Kovarik [79] (circles), used only small radon samples<sup>6</sup>. He concluded in the paper that due to the small amounts of radon his measurements are strongly influenced by radon condensation in monatomic layers in his setup. Also the data by Wertenstein [80] (squares) have been obtained using only small amounts of radon. He explained the tension to other publications by residual gas impurities which impacted his measurements.

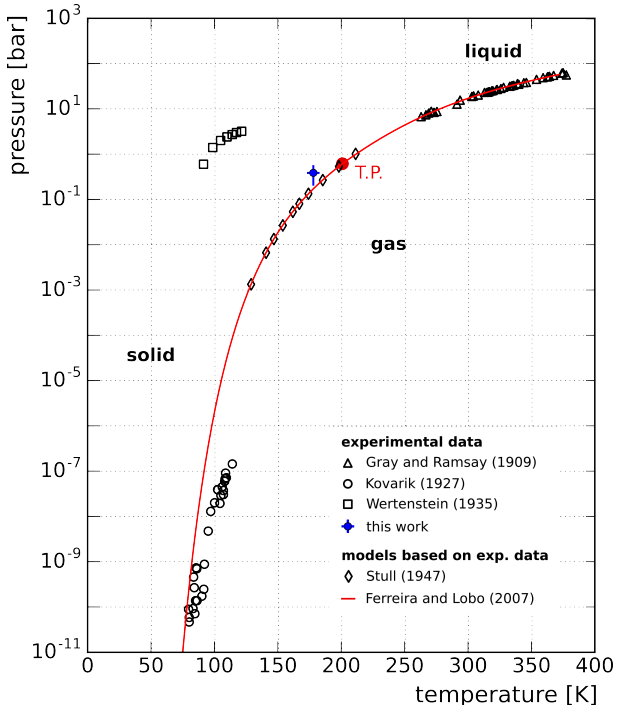
In addition, Figure 3.16 shows two theoretical models based on the experimental data. The values given by Stull [81] (diamonds) are based on the data by Gray and Ramsay and derived by means of the fugacity of a gas as described in [78]. The red line indicates an empiric model derived by Ferreira and Lobo [75] which we already introduced in section 2.4.2.

Given the uncertainties of the experimental data, our result for the vapor pressure of radon is in good agreement with previous measurements. The empiric model by Ferreira and Lobo suggests a slightly lower pressure translating also into a higher reduction factor of  $R = 11$  (see section 2.4.1). Nevertheless, we want to emphasize the different systematics of our result. While the other measurements aimed to use a radon sample as clean as possible, we derived our result from a binary mixture of xenon and radon while

---

<sup>6</sup>There is no number given, however, from the activity measurements we estimate less than  $10^{-10}$  g of radon.

**Figure 3.16.:** Experimental data obtained for the vapor pressure of radon by Gray and Ramsay [78] (triangles), Kovarik [79] (circles) and Wertenstein [80] (squares). The models published by Stull [81] (diamonds) and Ferreira and Lobo [75] (red line) are adapted to the experimental data. The radon vapor pressure derived in this work is shown by the blue data point. The triple point as predicted by [82] is marked by the red circle.



recuperating continuously the boil-off gas. The effect of xenon on the vapor pressure has not been studied in this thesis. Furthermore, the validity of Raoult's law at the investigated radon concentrations at the  $10^{-15}$  mol/mol level needs to be shown. The focus of our runs was clearly the proof of radon depletion in xenon boil-off gas due to cryogenic distillation and its suitability to be used as an on-line radon removal system. Thus, the vapor pressure for radon should be only understood as a side discussion.

### 3.6. Summary and conclusions

We summarize our results in Table 3.2. In all runs we measured a clear radon reduction in the boil-off xenon by a factor  $R \gtrsim 4$ . Motivated by the evolution of  $R$  observed in xe\_run3 and xe\_run4, we distinguish between the reduction factors measured when the liquid level was above or below the bottom edge of the bell structure. In the last two measurements, xe\_run5 and xe\_run6, the bell structure was not installed. The statistical error is the counting error of the activity measurements. Systematic uncertainties origin from the filled xenon mass, the mass flow controller and the mass of the total boil-off gas inside the cryostat.

The lowest reduction factor, measured by means of the radon monitor, was obtained in the static run xe\_run1. This measurement is particular due to the small xenon amount initially filled and the large radon activity concentration of the liquid reservoir. The second static run, xe\_run2, is in good agreement with the results obtained in the dynamic measurements at small recuperation flows of about  $f = 0.5$  slpm.

The runs xe\_run3 and xe\_run4 are of particular interest as both show the previously introduced bell signature (see, e.g., Figure 3.11). The reduction factor  $R$  is significantly lower as long as the liquid xenon level is above the bottom edge of the bell structure, i.e., the measured boil-off xenon is only recuperated from the gas phase enclosed by the bell. The cause of this effect is not understood. Explanations focusing on the smaller liquid surface below the bell from where the xenon was evaporated or the bell's additional heat input are not supported by the measurements at higher recuperation flows. There, we achieved high xenon evaporation rates and additionally increased the heat input in order to keep the recuperation flows stable but couldn't find any correlations to the reduction factor  $R$ .

In xe\_run5, where the bell structure was absent, we observe a stable reduction factor throughout the run. The measured  $R$  is comparable with the values obtained in xe\_run3 and xe\_run4 when the liquid level was below the bell. The reduction factor did not change even when we increased the recuperation flow to 3.5 slpm. In xe\_run6, we obtained a significantly smaller  $R$  with respect to the other measurements done at similar recuperation flows. After adjusting higher recuperation flows of 6.0 slpm and later 8.0 slpm, the reduction factor increased to a higher level. We want to emphasize that this run is exceptional since the radon monitor was operated at non standard high voltage settings. The higher reduction factor measured for higher flows might be due to an insufficient correction of the radon monitor's detection efficiency which is also impacted by the purge flow.

Even though the bell signature is not understood, our measurements clearly show a radon depletion in the boil-off gas above a liquid xenon reservoir. These results demonstrate for the first time the applicability of cryogenic distillation to purify xenon from  $^{222}\text{Rn}$ . The thereby measured  $^{218}\text{Po}$  activity concentrations below 1 kBq/kg correspond to a radon concentration in xenon at the  $10^{-15}$  mol/mol level. In section 2.4.1, we used the saturation vapor curves of xenon and radon to predict the reduction factor for a single distillation stage. Our measurements showed a lower reduction factor than the theoretically derived value of  $R = 11$ . The comparison, however, is challenging since the radon saturation vapor curve isn't precisely known and most of our measurements have been performed dynamically. Furthermore, it is unclear if the prediction derived from Raoult's law is still valid at the low concentrations we are investigating in this work. In the following chapter, we demonstrate the first on-line radon removal system by means of cryogenic distillation operated at the XENON100 detector.

3. Radon depletion in xenon boil-off gas

---

	$M_0$ [kg]	$c_t(t_0)$ [kBq/kg]	recup. flow [slpm]	detector, analysis	reduction factor R
xe.run1	0.6	35.0	static	radon monitor prop. counter	$3.4 \pm 0.2$ stat $^{+0.5}_{-0.2}$ syst $4.11 \pm 0.54$ stat $^{+0.25}_{-0.21}$ syst
xe.run2	1.9	10.4	static	radon monitor prop. counter	$4.63 \pm 0.21$ stat $^{+0.10}_{-0.07}$ syst $5.29 \pm 0.86$ stat $^{+0.11}_{-0.09}$ syst
xe.run3	2.1	4.5	0.50	radon monitor prop. counter const. fit	$4.61 \pm 0.02$ stat $^{+0.29}_{-0.27}$ syst $5.58 \pm 0.02$ stat $^{+0.88}_{-0.63}$ syst $3.75 \pm 0.50$ stat $^{+0.08}_{-0.06}$ syst $2.9 \pm 0.1$ stat $^{+2.0}_{-1.0}$ syst
xe.run4	2.7	1.8	0.55	radon monitor prop. counter const. fit	$5.27 \pm 0.05$ stat $^{+0.22}_{-0.27}$ syst $6.02 \pm 0.04$ stat $^{+1.12}_{-0.78}$ syst $4.91 \pm 0.68$ stat $^{+0.07}_{-0.05}$ syst $4.2 \pm 1.0$ stat $^{+3.6}_{-0.7}$ syst $4.7 \pm 0.3$ stat $^{+3.7}_{-2.0}$ syst
xe.run5	2.6	1.2	0.50	radon monitor prop. counter 3.50	$7.20 \pm 0.04$ stat $^{+0.50}_{-0.31}$ syst $8.12 \pm 1.35$ stat $^{+0.13}_{-0.10}$ syst $6.84 \pm 0.08$ stat $^{+1.06}_{-0.68}$ syst
xe.run6	4.0	0.9	0.50	radon monitor radon monitor	$3.77 \pm 0.09$ stat $^{+0.12}_{-0.13}$ syst $5.47 \pm 0.15$ stat $^{+0.98}_{-0.93}$ syst

**Table 3.2.:** Summarized results for the radon reduction factor  $R$ . The different analyzes and individual runs are discussed in section 3.3 and section 3.4 respectively.

# Chapter 4

## Operation of a distillation based radon removal system at XENON100

In chapter 2, we discussed the concept of a radon removal system (RRS) and its capability to purify xenon from  $^{222}\text{Rn}$  contaminations in liquid xenon based detectors such as XENON1T. We found that such a system, integrated in the detectors gas purification loop, can efficiently remove radon originating from emanation. In chapter 3, we investigated the suitability of cryogenic distillation as a technique to separate radon and xenon. We could show, that the  $^{222}\text{Rn}$  activity concentration in xenon gets reduced by a factor of  $R \gtrsim 4$  in a single distillation step. Similarly to purifying xenon from krypton by means of cryogenic distillation [83, 84], we expect the radon reduction capability to be enhanced in a multiple stage distillation column.

During the Radon Distillation Campaign, performed from December 2014 to February 2015, we extended the gas purification loop of XENON100 by a cryogenic distillation column which has been adapted for radon distillation. We operated the column in two distillation runs as an on-line radon removal system for XENON100, i.e. xenon was continuously looped from the detector through the column where it got purified. By making use of XENON100 as an  $\alpha$ -detector, we could monitor the  $^{222}\text{Rn}$  activity concentration in the liquid xenon target during the distillation campaign. Since the radon decays inside the distillation column there is no need of extracting radon enriched off-gas as it is necessary, e.g., for krypton distillation. Thus, no xenon was lost during the on-line operation of the radon removal system. The main results of this work have been published in [85].

We start this chapter with an introduction to our data analysis where we discuss the identification of  $^{222}\text{Rn}$  events in XENON100. In section 4.2, we describe our experimental setup. In section 4.3, we report the first successful operation of an RRS based on cryogenic distillation for a liquid xenon experiment such as XENON100. The radon reduction capability of the distillation column is quantified in section 4.4. To do so, we used an auxiliary radon emanation source to increase the radon concentration in the detector. We conclude this chapter by giving in section 4.5 an outlook for the realization

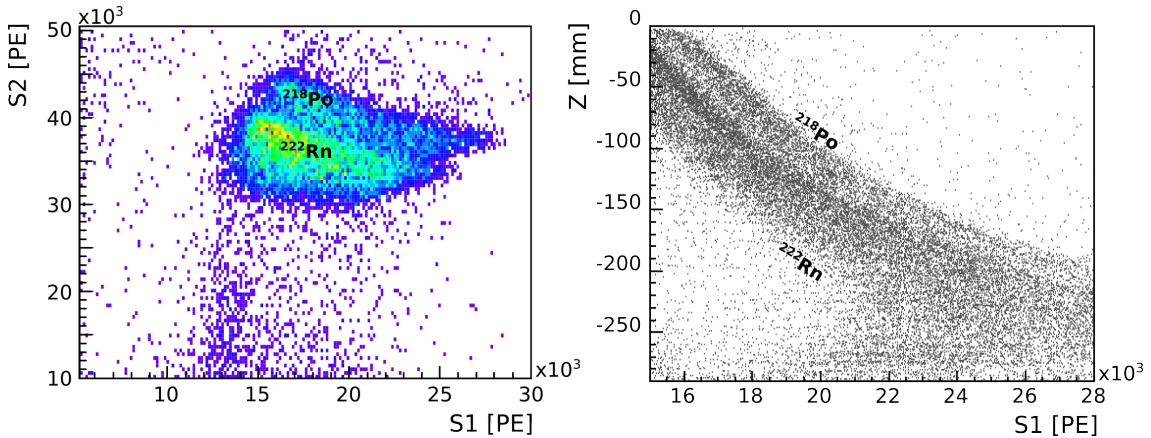


**Figure 4.1.:** (Left)  $\alpha$ -events appear isolated at high S1/S2 signal regions. The single decays of radon and its progenies cannot be resolved without a dedicated the S1  $\alpha$ -correction map. (Right) The S1 signals of the mono-energetic  $\alpha$ -decays of  $^{222}\text{Rn}$  and  $^{218}\text{Po}$  as a function of their Z-coordinate (i.e., depth inside the TPC).

of an RRS for the XENON1T detector.

## 4.1. Data analysis

During the distillation campaign, we studied the impact of the distillation column on the  $^{222}\text{Rn}$  activity concentration inside the XENON100 detector. Even though the detector was designed to be sensitive to low energetic nuclear recoil events, we can use XENON100 to identify radioactive decays of radon and its progenies and thus monitor their evolution with time. We can make use of two standard methods to determine the activity concentration of  $^{222}\text{Rn}$  in the liquid xenon target. Firstly, the high energetic  $\alpha$ -decays of  $^{222}\text{Rn}$  can be clearly identified in XENON100 data. Secondly, we can make use of the time coincident decay of the radon progenies  $^{214}\text{Bi}$  and  $^{214}\text{Po}$  (BiPo events). Both methods are discussed in detail in [61] and [86]. For our data analysis, we mostly use the  $\alpha$ -analysis adapted to our purposes. The BiPo analysis is used to cross-check our results.

### 4.1.1. Analysis using $\alpha$ -decays

The high energetic  $\alpha$ -decays of radon and its progenies give a clear signal in both, primary- (S1) and secondary scintillation light (S2). The raw, i.e., uncorrected signals are shown in Figure 4.1 (Left). Already by eye, we can distinguish two overlaying event distributions. Both occur at large signals of  $S1 > 10\,000$  and  $S2 > 28\,000$  photo-electrons (PE). We will later assign the two events distributions to  $^{222}\text{Rn}$  and  $^{218}\text{Po}$ , respectively. In the following, we will define our selection criteria to identify  $^{222}\text{Rn}$  events in our data.

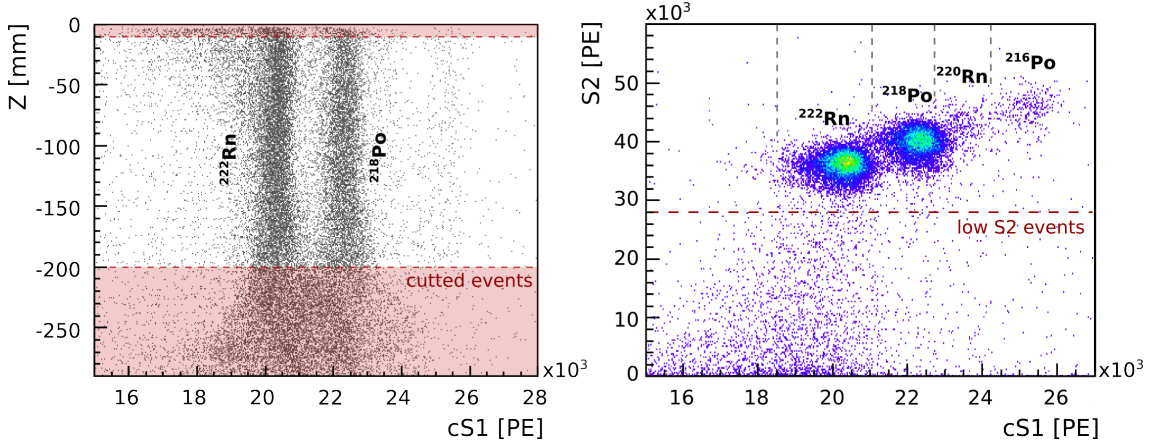


**Figure 4.2.:** (Left)  $\alpha$ -decays of  $^{222}\text{Rn}$  and  $^{218}\text{Po}$  after applying the S1  $\alpha$ -correction map. Over a wide range in  $Z$  the two populations can be clearly separated which is used for analysis. (Right) Different  $\alpha$  populations are identified in the S1/S2 plane. Events appearing at low cS2 signals are cut for the analysis.

### S1/S2 signal corrections

The amount of detected photo-electrons of mono-energetic events is dependent on their position inside the XENON100 TPC. This is illustrated exemplary in Figure 4.1 (Right) showing the  $Z$ -dependent S1 signals of the  $\alpha$ -decays from  $^{222}\text{Rn}$  and its daughter  $^{218}\text{Po}$ . In XENON100, we correct for this position dependent light yield, which is mainly caused by solid angle effects and reflectivity losses [41]. The correction, however, has been optimized for low-energy events as they are expected in dark matter runs. For the high energetic radon decays, a dedicated  $\alpha$ -correction map is necessary to account, e.g., for PMT-saturation effects, typical for large S1 signals. We refer to the  $\alpha$ -corrected S1-signals as  $cS1$ . The  $\alpha$ -correction map used in our analysis was introduced in [61] and corrects S1 signals according to their  $Z$  (depth) and  $R$  (radial) position inside the TPC. For S2 signals, another correction map is necessary to account for small inhomogeneities of the drift field which can bias the position reconstruction of the decay. In order to correct for this, we use the standard S2-correction algorithm developed for XENON100 [41]. We refer to the corrected S2-signals as  $cS2$ . The impact of the S1  $\alpha$ -correction map to our data is shown in Figure 4.2 (Left). The event populations of  $^{222}\text{Rn}$  and  $^{218}\text{Po}$  decays are clearly separated and have a constant signal size throughout the TPC. Only at low  $Z < -200$  mm, the double peak structure cannot be resolved. The  $\alpha$ -correction map is based on data from 2009 where a higher impurity level of the liquid xenon caused a lower light yield [61]. Together with different PMT settings, this explains the diffuse peak separation at low  $Z$  due to an underestimation of PMT-saturation effects. As a consequence, we limit our analysis to events that happen within  $-200 \text{ mm} < Z < -10 \text{ mm}$  where we achieve a good energy resolution. In Figure 4.2 (Right), we show the remaining events in the S1/S2 plane after S1 and S2 corrections have been applied. Compared to Figure 4.1, we now can clearly distinguish different  $\alpha$ -event populations which we will

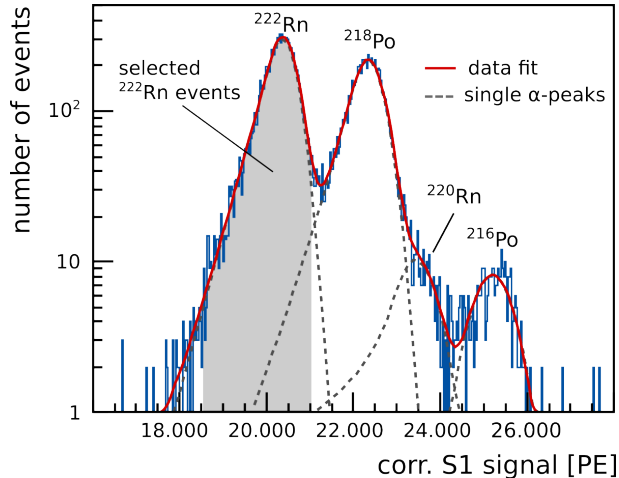


**Figure 4.3.:** Fit of the S1 energy spectrum using Crystal-Ball functions [68]. We identify  $\alpha$ -decays from both, the  $^{222}\text{Rn}$  and the  $^{220}\text{Rn}$  decay-chain. The shadowed region marks our event window used in the  $\alpha$ -analysis to select  $^{222}\text{Rn}$  events.

later assign to  $^{222}\text{Rn}$ ,  $^{220}\text{Rn}$  and their progenies. Events reaching  $\text{cS2} < 28\,000 \text{ PE}$  are cut for later  $\alpha$ -analysis. Their identity and impact on the obtained results is discussed in the subsequent section 4.1.3.

Since the S2 signals are sensitive to small changes in detector parameters, e.g., the liquid xenon level or electron lifetime, we want to restrict our further  $^{222}\text{Rn}$  event selection criteria to the S1 signals only.

### Peak identification

In the following, we look into the projection of Figures 4.2 onto the cS1 axis after applying the above described cuts in Z and cS2. The obtained peak spectrum is shown in Figure 4.3. From previous analysis results [61] but also from the injection of the auxiliary O-ring emanation source during the second distillation run (see section 4.2), we can identify the two highest peaks as the  $^{222}\text{Rn}$  and the  $^{218}\text{Po}$   $\alpha$ -decays, respectively. Together with two further peaks, recognized at higher cS1 signals in figures 4.2 (Right) and 4.3, we can fit the S1 spectrum with four overlaying Crystal-Ball functions [68]. We have introduced this set of asymmetric functions when fitting the energy spectrum obtained by the radon monitors in section 2.3.1. The observed asymmetric behavior is different to the Gaussian distribution of  $\alpha$ -events found in [61]. We explain this mostly by a missing radial cut which would sort out events happen at the edges of the TPC where the light yield is expected to be lower [41]. Secondly, the asymmetric peaks might be caused by the S1 signal correction described above. Events close to the top of the TPC but also at low Z-coordinates, i.e. close to the minimum Z-value accepted in this analysis, happen to be corrected towards lower S1s (see Figure 4.1). This is explained by the fact that some detector conditions, e.g., xenon purity, cathode voltage, liquid level, have slightly changed since the  $\alpha$ -correction has been developed in 2009.

The fit using Crystal-Ball functions describes the S1 spectrum with a reduced  $\chi^2/\text{ndf} = 0.9$  and is shown in Figure 4.3 (red solid line). In Table 4.1, we list the determined values for the full-adsorption energy  $\mu_{S1}$  of each peak. As described above, we can

Isotope (Decay Chain)	Decay energy [MeV]	Energy relative to $^{222}\text{Rn}$	cS1 energy by fit [PE]	fitted cS1 relative to $^{222}\text{Rn}$ -cS1
$^{222}\text{Rn}$ ( $^{222}\text{Rn}$ )	5.59	1.00	$20\ 360 \pm 10$	1
$^{218}\text{Po}$ ( $^{222}\text{Rn}$ )	6.11	1.09	$22\ 330 \pm 10$	1.10
$^{212}\text{Bi}$ ( $^{220}\text{Rn}$ )	6.21		no fit possible, hidden by $^{218}\text{Po}$ peak	
$^{220}\text{Rn}$ ( $^{220}\text{Rn}$ )	6.40	1.14	$23\ 430 \pm 60$	1.15
$^{216}\text{Po}$ ( $^{220}\text{Rn}$ )	6.91	1.24	$25\ 200 \pm 30$	1.24

**Table 4.1.:** Results of the spectral fit shown in Figure 4.3. By comparison of the energy ratios as obtained by fit with those of literature values (section 2.1), we can clearly assign the single peaks to  $\alpha$ -decays within the  $^{222}\text{Rn}$  and the  $^{220}\text{Rn}$  decay chains.

clearly identify  $^{222}\text{Rn}$  events at 20 000 PE and  $^{218}\text{Po}$  decays at 22 000 PE, respectively. The analysis in [61] describes already the observation that there are about 20% less  $^{218}\text{Po}$  events with respect to  $^{222}\text{Rn}$ . We found for a  $^{218}\text{Po}/^{222}\text{Rn}$  ratio of  $0.85_{-0.04}^{+0.06}$  during the radon distillation campaign. Ongoing studies focus on plate-out effects of the charged daughter isotopes after an  $\alpha$ -decay in order to explain this effect [87]. The third  $\alpha$ -decay within the  $^{222}\text{Rn}$  chain is that of  $^{214}\text{Po}$  (see Figure 2.1) which is part of the later discussed BiPo events. As we will see in section 4.1.2, the detector's detection efficiency is strongly suppressed for  $^{214}\text{Po}$  events. In Figure 4.3 we identify also  $^{220}\text{Rn}$  and  $^{216}\text{Po}$ . The other  $\alpha$ -events within the thoron chain are either suppressed due to the detector's efficiency (in case of  $^{212}\text{Po}$ ) or overlaid by the dominating decays within the  $^{222}\text{Rn}$  chain (in case of  $^{212}\text{Bi}$ ).

### $^{222}\text{Rn}$ event selection

So far, we set requirements only for the Z-position ( $-200\text{ mm} < Z < -10\text{ mm}$ ) and the corrected S2 energy ( $\text{cS2} > 28\,000\text{ PE}$ ). This allowed us to identify  $\alpha$ -decays within the  $^{222}\text{Rn}$  decay-chain in the S1-spectrum (see Figure 4.3). In order to monitor the radon activity concentration during the distillation campaign, we selected only  $^{222}\text{Rn}$  events within the energy window  $18\,600 < \text{cS1} [\text{PE}] < 21\,000$ . For this selection we achieved an acceptance of 90% by fitting the  $\alpha$ -spectrum. Furthermore, we found that 10% of the selected events are actually  $^{218}\text{Po}$  decays, leaking to lower energies. Both effects need to be taken into account when we later calculate an absolute  $^{222}\text{Rn}$  rate inside the detector.

#### 4.1.2. BiPo analysis

The subsequent decay of  $^{214}\text{Bi}$  ( $\beta$ -decay) and  $^{214}\text{Po}$  ( $\alpha$ -decay) is referred to as BiPo event. Due to the short half-life of  $^{214}\text{Po}$  ( $\tau_{1/2} = 164\ \mu\text{s}$ ), both decays are likely to happen within the same event-window of XENON100. The time coincidence is a smoking gun to identify BiPo events and thus to conclude also on the activity concentration of their direct mother  $^{222}\text{Rn}$ . In this section we give a short summary of the BiPo analysis

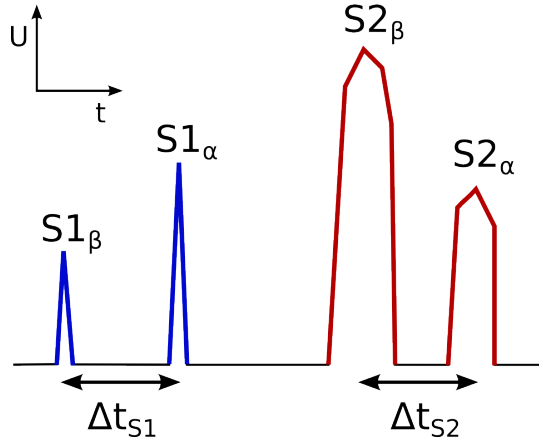


**Figure 4.4.:** The characteristic signature of a BiPo event, where both decays happen within the same event-window of the XENON100 data acquisition. Figure taken from [86] and modified.

developed in [86]. It provides a complementary monitoring tool to the above described  $\alpha$ -analysis and is later used as a cross-check.

### BiPo event selection

In Figure 4.4 we show an idealized BiPo event as it is recorded by the XENON100 detector. Here, the S1 and S2 signals of both, the  $^{214}\text{Bi}$   $\beta$ -decay and the  $^{214}\text{Po}$   $\alpha$ -decay happen within the same event-window of the XENON100 data acquisition. A typical BiPo event needs to fulfill the following criteria: The event-window needs to contain two S1 signals. Additionally, the earlier S1, originating from the  $\beta$ -event, is smaller than the second S1 which has been induced by the  $\alpha$ -decay. Due to the short timescale of the BiPo event, we can assume that both decays happen at the same spatial coordinates inside the TPC [88]. As a consequence we demand that the time difference between the two S1 signals ( $\Delta t_{S1}$  in Figure 4.4) is the same as for the corresponding S2 signals ( $\Delta t_{S2}$ ).

In our analysis we are only interested in BiPo events from the  $^{222}\text{Rn}$  decay chain. Above selection criteria, however, are also fulfilled by BiPo events originating from the  $^{220}\text{Rn}$  chain (thoron). The  $\alpha$ -decay of  $^{212}\text{Po}$ , however, has an even shorter half-life of  $\tau_{1/2} = 300\text{ ns}$ . This allows us to suppress BiPo events from the thoron chain by selecting only events which fulfill  $\Delta t_{S1} \geq 2\mu\text{s}$  [86].

### Detection efficiencies

The above described BiPo event selection was found to have an efficiency of about 20%. This is mostly caused by the finite length of the data acquisition window of XENON100. As a consequence, only parts of the BiPo signature are recorded, depending on the spatial coordinates of the events and their consequent drift times. Also incomplete charge collection at the edges of the TPC reduce the BiPo tagging efficiency. After correction of these effects, the obtained BiPo rate was still found to be about 50% smaller than the simultaneously monitored  $^{222}\text{Rn}$   $\alpha$ -rate [86]. Preliminary analysis point to plate-out effects at the cathode and the walls of the TPC which might also cause the reduced

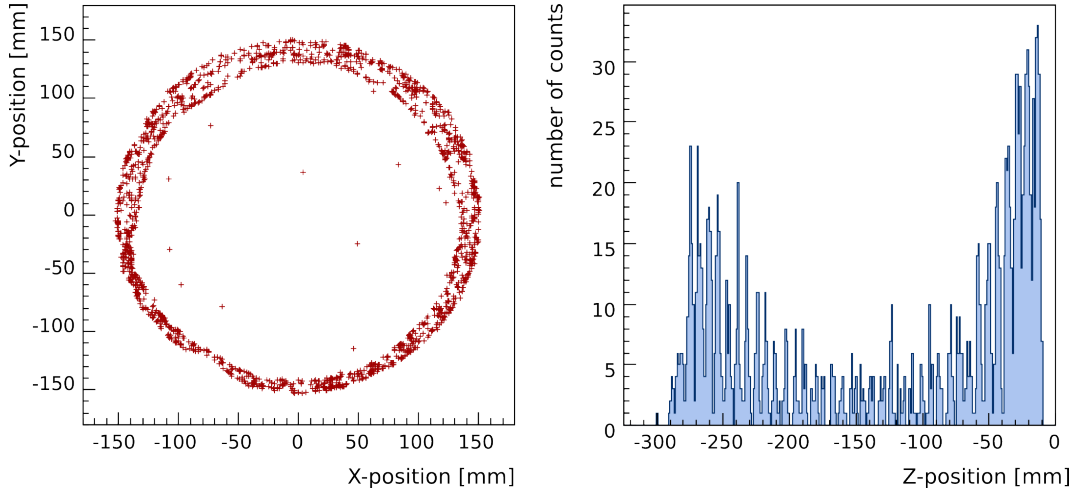


**Figure 4.5.:** The X/Y-position (Left) and the Z-position (Right) of our low S2 events in the XENON100 TPC.

$^{218}\text{Po}$  rate with respect to its daughter  $^{222}\text{Rn}$  (see section 4.1.1). In this work, we only analyze relative changes in the BiPo activity during the radon distillation runs. Thus, the knowledge of the absolute rate is not needed when analyzing the impact of the RRS. For a detailed discussion we therefore refer again to [86].

#### 4.1.3. $^{210}\text{Po}$ events in XENON100

In this section we will investigate events having a large S1 signal, typical for  $\alpha$ -events, but a lower S2 signal. They will be identified as  $\alpha$ -decays from  $^{210}\text{Po}$ . We restrict the here presented analysis to events fulfilling  $\text{cS1} > 10.000 \text{ PE}$  and  $\text{cS2} < 28.000 \text{ PE}$  (see Figure 4.2).

##### Spatial distribution

The spatial distribution of the selected events is shown in Figure 4.5. In their radial X/Y-coordinates (Left) we observe them solely located at the edges of the TPC. Due to the reduced S2 light collection efficiency and electric field inhomogeneities at large radii [41] the radial position of the events might explain already their striking lower S2 signals with respect to other  $\alpha$ -events.

For the Z-coordinate (Right), we find most events accumulated at the anode ( $Z = 0 \text{ mm}$ ) and above the cathode ( $Z = -300 \text{ mm}$ ). We identify 39 underlaying peaks in the Z-distribution of the events. This corresponds to the number of field-shaping rings which are enclosing the TPC as a field cage in order to provide a homogeneous drift field. The accumulation at the field-shaping rings might be only an artifact of the position reconstruction algorithm but it can also originate from, e.g., shielding of the drifting electrons. The above described spatial distribution is expected for  $^{210}\text{Po}$  events. We have seen in previous studies [61] that radon progenies accumulate in the cathode region. In sec-

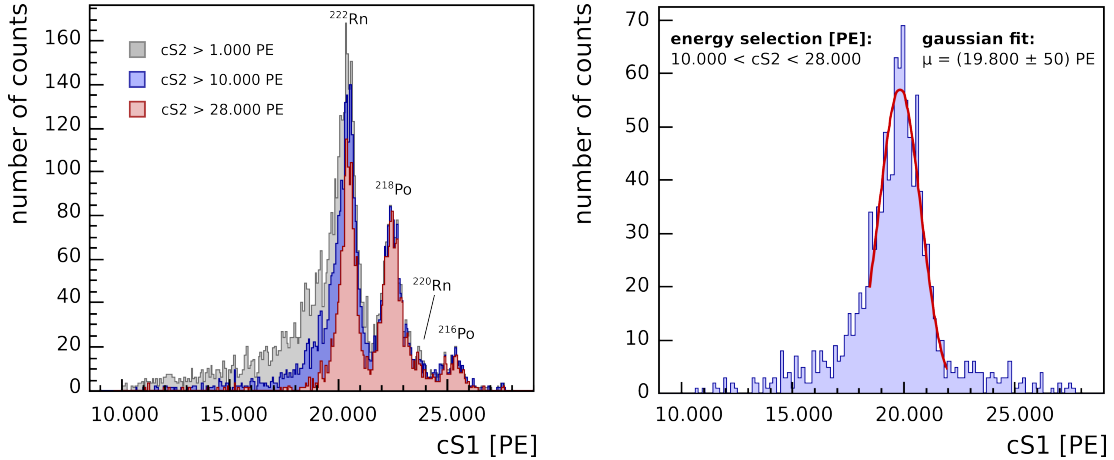


**Figure 4.6.:** (Left) The cS1 spectra for different thresholds of the low S2 cut. The foremost red spectrum corresponds to the low S2 cut as it was used in our  $\alpha$ -analysis. (Right) Gaussian fit of the cS1 energy of the low S2 events.

tion 4.1.1 we mentioned plate-out effects and ion drift to explain this effect. In the LUX experiment,  $^{210}\text{Po}$   $\alpha$ -decays have been identified by their S1 energy [89]. Their spatial distribution inside the LUX liquid xenon TPC showed the same properties as we have found for the here investigated events.

### Energy spectrum

Beside their spatial position, the other striking feature of the investigated low S2 events is their high energetic S1 signal. The only known interactions showing this large but well located signals are  $\alpha$ -decays. In Figure 4.6, we looked into the cS1 spectrum after having applied different cuts on the cS2-energy. In addition, we use a Z-cut of  $-200 \text{ mm} < Z < -10 \text{ mm}$ , similar as we did in the  $\alpha$ -analysis. The red spectrum corresponds to the selection cut used in the  $\alpha$ -analysis. We can identify the peaks of  $^{222}\text{Rn}$  and its progeny  $^{218}\text{Po}$  as well as the  $^{220}\text{Rn}$  daughter  $^{216}\text{Po}$  (see section 4.1.1). By weaken the energy cut on the cS2, we include the low S2 events into the energy spectrum (blue and gray spectra in Figure 4.6). We observe that these low S2 events have a maximum cS1 energy of about that energy found for the  $^{222}\text{Rn}$  decay. Only a minority leaks into the neighbored  $^{218}\text{Po}$  peak. However, in case the investigated low S2 events are misidentified  $^{222}\text{Rn}$  decays, we would expect to detect also the subsequent  $^{218}\text{Po}$  decay at their maximum S1 energy. For further investigation, we plotted the cS1 spectrum for events requiring  $10\,000 \text{ PE} < \text{cS2} < 28\,000 \text{ PE}$ . The result in Figure 4.6 (Right) shows a clear peak of the low S2 events at the energy of  $(19.800 \pm 50) \text{ PE}$  (Gaussian fit). Using the fit results for the  $^{222}\text{Rn}$  events shown in Table 4.1 and assuming a linear energy dependence, we translate the mean of the Gaussian fit to an energy of  $(5.37 \pm 0.07) \text{ MeV}$ . This is in agreement with the decay energy of  $^{210}\text{Po}$  of  $5.40 \text{ MeV}$  (see Figure 2.1).

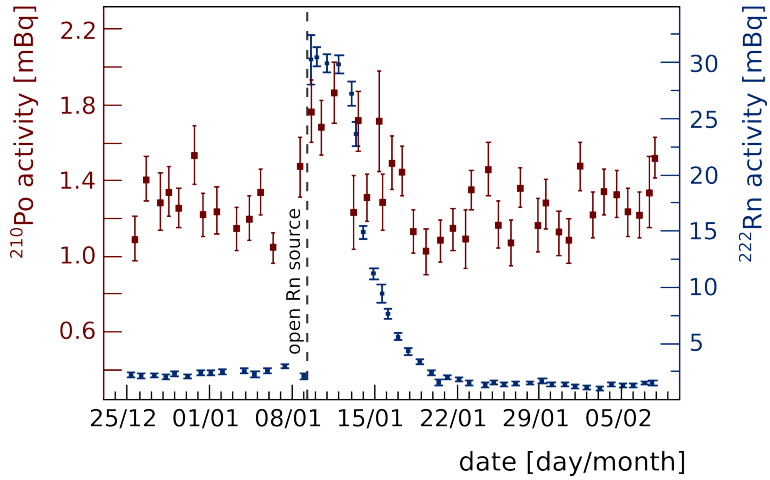


**Figure 4.7.:** During the radon distillation campaign, the  $^{222}\text{Rn}$  rate changed by a factor of 10 after opening the auxiliary radon emanation source. The rate of the low S2 events, on the other hand, increased only by about 40%.

### Time evolution during radon distillation campaign

During the radon distillation campaign, the  $^{222}\text{Rn}$  activity measured in XENON100 changed by one order of magnitude due to an auxiliary emanation source and the subsequent distillation process (see section 4.3). In Figure 4.7 we compare the radon evolution (blue data points) to the rate of our investigated low S2 events (red data points). After opening the auxiliary radon source, the  $^{222}\text{Rn}$  activity immediately increased by a factor of 10. The low S2 events, on the other hand, showed only a moderate increase of about 40%. We conclude that the investigated events are practically independent from the evolution of  $^{222}\text{Rn}$ . Only a small fraction might origin from misidentified  $^{222}\text{Rn}$   $\alpha$ -decays or radon progenies. We estimated the fraction of misidentified  $^{222}\text{Rn}$  to be  $< 2\%$  and will neglect this leakage for our further studies.

From our analysis of the so-called low S2 events we have learned that they are located solely at the edges of the XENON100 TPC. The S1 spectrum of these events peaks at energies of  $(5.37 \pm 0.07)$  MeV. Furthermore, we can exclude the hypothesis that the low S2 events are misidentified  $^{222}\text{Rn}$  events since the time evolution of the larger fraction of those events basically doesn't correlate with that of radon. From these properties we conclude that these events origin from the decay of  $^{210}\text{Po}$ . This isotope is also part of the  $^{222}\text{Rn}$  decay chain, however, due to the long half-life of  $^{210}\text{Pb}$ , the secular equilibrium might be broken. Thus, we assume that the observed  $^{210}\text{Po}$  rate is mostly related to the exposure of the wall materials to air before XENON100's construction. In addition, polonium accumulates at the surfaces of the TPC due to plate-out effects. There the charge collection is strongly influenced by, e.g., inhomogeneities of the drift field which explains the smaller S2 signals with respect to other  $\alpha$ -events.

## 4. Operation of a distillation based radon removal system at XENON100

---

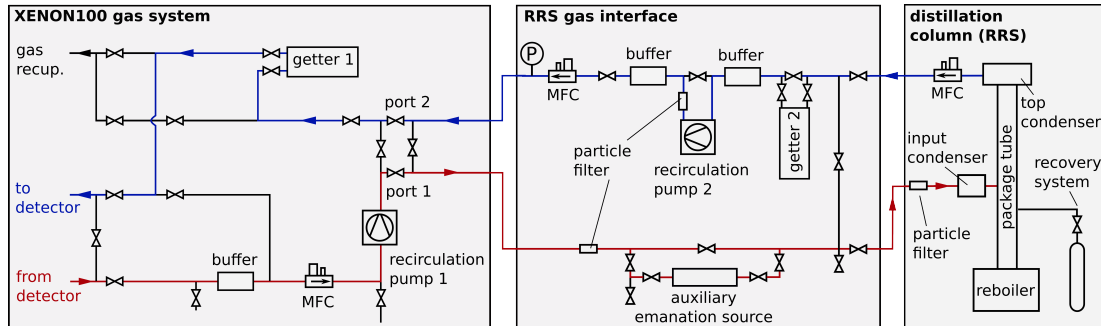


**Figure 4.8.:** The xenon coming from the detector was guided from the XENON100 gas system via an interface gas system to the distillation system, where the radon was removed. The purified xenon was pumped back to the detector. A bypass to an auxiliary radon source could be opened to enhance the radon concentration in the system.

## 4.2. Experimental setup

During the radon distillation campaign, we extended the XENON100 purification loop by a cryogenic distillation column, acting as our radon removal system (RRS). As shown in Figure 4.8, an RRS gas interface provided the connection between XENON100 and the distillation column. During the distillation campaign, xenon was flushed from the detector via the RRS gas interface towards the RRS by means of the recirculation pump 1 (red line). Before entering the distillation column, the xenon could be flushed through an auxiliary radon emanation source. This source enabled us to increase the radon emanation rate of the detector system. In the distillation column, the xenon got purified from radon and was flushed back towards the detector by means of the recirculation pump 2 (blue line). In order to ensure a balanced mass flow between inlet and outlet of the column, we used mass-flow controllers. Before the radon depleted xenon reentered the detector, it was purified from electronegative impurities using a gas purifier (getter 1 in Figure 4.8). The RRS gas interface was equipped with an additional gas purifier (getter 2). It was only used during the preparation phase of the newly installed RRS gas interface and the distillation column. During the distillation run, getter 2 was switched off and always bypassed. In view of its relevance for our results, we want to give more details about the auxiliary radon emanation source and the distillation column:

**Auxiliary radon emanation source** The auxiliary radon emanation source enabled us to enhance the radon contamination of the xenon. Since it was placed before the distillation column, it is classified as a type II source (see section 2.4.1). In contrast to the natural emanation sources of XENON100, the auxiliary source could be switched on/off during the distillation campaign. As shown in Figure 4.10, it is built up from a 21 stainless steel vessel filled with 426 viton O-rings (Novotek). From previous emanation measurements, we know that these O-rings have a high  $^{222}\text{Rn}$  emanation rate. For the auxiliary emanation source we measured a source strength of  $(91 \pm 6)$  mBq using proportional counters. The  $^{222}\text{Rn}$  emanation rate of the XENON100 detector has been measured to

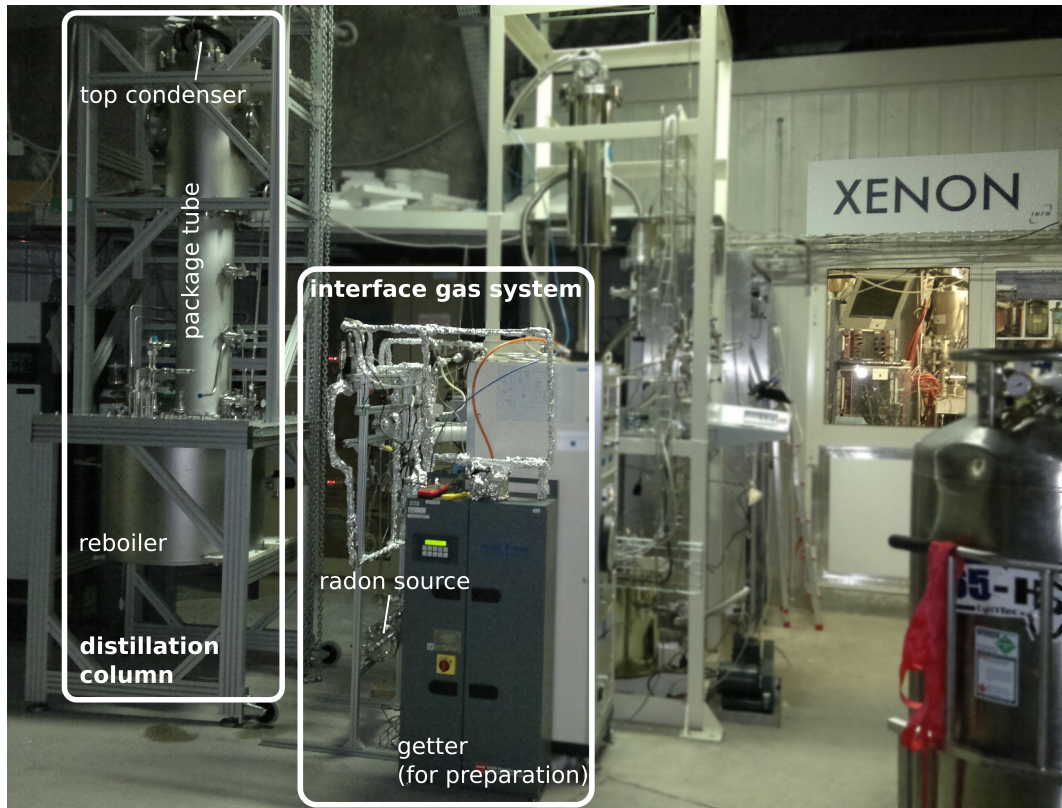


**Figure 4.9.:** Picture of the experimental setup on site. From the XENON100 detector, visible through the window in the XENON box, the xenon was looped via the RRS gas interface through the distillation column.



**Figure 4.10.:** (Left) Picture of the O-ring emanation source vessel as it was integrated in the interface gas system. (Right) Sample of the same type of viton O-rings (Novotek) prepared for radon emanation measurements using proportional counters.

be  $(9.3 \pm 1.0)$  mBq and that of the XENON100 gas system  $(2.6 \pm 0.5)$  mBq [62]. Therefore, the O-ring source was the dominating source in our experimental setup during the distillation campaign.

**Distillation column** We made use of the Phase-1 distillation column, developed in the framework of the XENON1T experiment, in order to purify xenon from krypton [57, 90]. While krypton is enriched in the gas phase due to its higher saturation vapor pressure with respect to xenon, the situation is inverted in case of radon (see section 2.4.2). As we show in Figure 4.8, the xenon was flushed from the RRS gas interface into the column’s input condenser. In the input condenser the gas was pre-cooled before it is injected into the center of the column’s package tube. This vacuum insulated tube is 1 m long and filled with package material<sup>1</sup> to provide a large surface whereon the inflowing xenon liquefies. A liquid xenon reservoir up to 7 kg is stored in the reboiler vessel which is equipped with a heater. Inside the column, an equilibrium establishes between the xenon evaporating from the reboiler and xenon which is liquefied at the top condenser. The inflowing xenon from the detector was thereby negligible with respect to the xenon exchange along the package tube. Due to the thermal contact of liquid and gas in the package tube, this process is analogous to multiple distillation stages. The xenon which was taken from the top condenser was consequently depleted in radon when it was circulated back into the detector.

#### Preparation of the RRS gas interface and the distillation column

The distillation column arrived fully assembled from the Muenster University where it has been used in prior krypton distillation tests. For its transport to the LNGS, it was filled with 1.7 bar xenon as a protection gas. The RRS gas interface has been assembled on site and was pumped and baked for about two weeks. Then, we expanded the protection gas from the distillation column into the RRS gas interface. The xenon was looped for three days through the RRS gas interface, including a gas purifier (getter 2 in Figure 4.8), and the distillation column for cleaning purposes. Meanwhile, the connections to the XENON100 detector, i.e., port 1 and port 2, stayed closed. Before the start of the distillation campaign, the xenon was transferred into a gas cylinder (recovery system) by means of cryo-pumping. In preparation of each distillation run (see section 4.3.1), the distillation column was filled with xenon from the XENON100 detector.

### 4.3. Radon removal in XENON100

With the analysis tools developed in section 4.1, we are able to study the impact of our RRS realized for the XENON100 detector. During the distillation campaign, we performed two runs which mostly differed by the usage of the auxiliary radon emanation source in the 2nd distillation run. We want to start the discussion of our results in

---

<sup>1</sup>Package material from the company Sulzer.

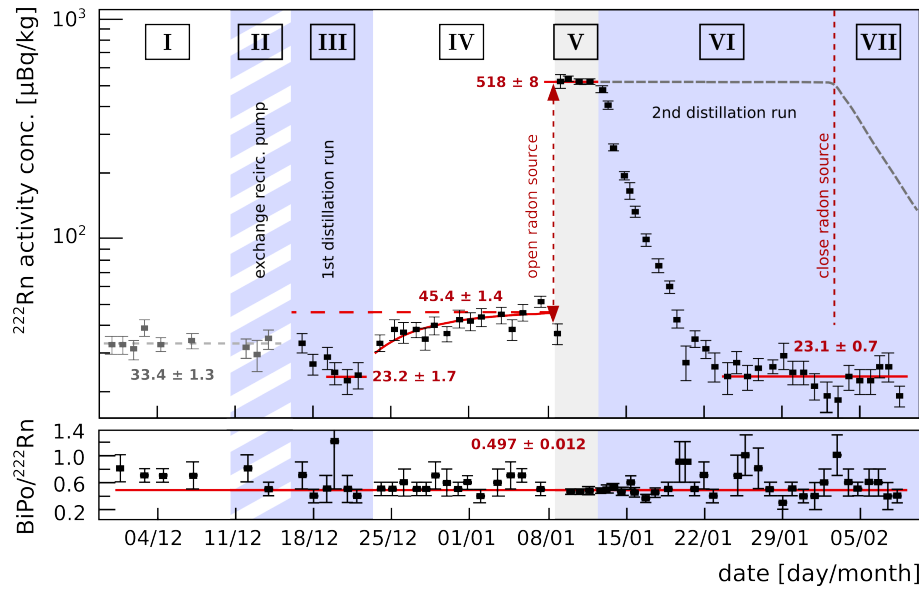


**Figure 4.11.:** (Top panel) The evolution of the  $^{222}\text{Rn}$  activity concentration in XENON100 determined by means of  $\alpha$ -counting. As indicated by the roman numerals, we distinguish seven operational phases of the purification system. (Bottom panel) The ratio of BiPo to  $^{222}\text{Rn}$  events demonstrates consistency of both analyses.

section 4.3.1 with an overview of the different operational modes of the RRS and their impact on the monitored radon activity concentration in XENON100. In section 4.3.2, we discuss the  $^{222}\text{Rn}$  evolution in detail. We will see that the achieved radon reduction inside the detector, expressed by the factor  $D$ , depends not only on the reduction capability of the RRS (later referred to as reduction factor  $R$ ) but also on the types of emanation sources according to our classification introduced in section 2.4.1 (type I and type II sources). The auxiliary  $^{222}\text{Rn}$  emanation source enabled us further, to study the timescales of mixing radon in the liquid xenon target of XENON100 which will be discussed in section 4.3.3. As a last topic, we will estimate possible radon leakage from ambient air which might influence our results in section 4.3.4.

### 4.3.1. Overview of the distillation campaign

The distillation campaign at XENON100 has been carried out from December 2014 until February 2015. The evolution of the  $^{222}\text{Rn}$  activity concentration, determined by means of  $\alpha$ -counting, is shown in Figure 4.11 (top panel). As a cross-check, we also show the ratio of BiPo and  $^{222}\text{Rn}$  events (bottom panel). As indicated by the roman numerals, we distinguish seven operational phases of the gas purification loop during the distillation campaign:

- I Pre-distillation phase: the detector was operated in its standard mode, i.e., xenon gas was circulated through the XENON100 gas-system with a mass flow of 5.0 slpm

#### 4. Operation of a distillation based radon removal system at XENON100

---

mass flow. Meanwhile, the newly installed RRS gas interface and the distillation column were pumped and baked for cleaning purposes.

- II Replacement of recirculation pump 1: in this phase we started the online distillation. However, the recirculation pump 1 at the XENON100 gas system failed twice. Both times, the gas purification was stopped for more than a day. The pump has been exchanged at the end of phase II.
- III 1st distillation run: the liquid xenon reservoir of the distillation column was filled with xenon from the XENON100 detector before we started distillation. During this phase, xenon was circulated through the distillation column at a recirculation speed of 4.5 slpm. This slightly reduced mass flow, with respect to 5.0 slpm in phase I, was kept stable throughout the rest of the distillation campaign. The auxiliary radon emanation source stayed closed.
- IV Standard operation: at the end of the 1st run, most of the column's liquid xenon reservoir was transferred back into the XENON100 detector. The distillation column was kept operational (i.e., the top condenser was still cooling), but the gas inlet and outlet were closed. Xenon from the detector was only looped through the standard purification loop of XENON100.
- V Open auxiliary radon emanation source: xenon gas was continuously looped through the auxiliary radon source but was bypassing the distillation column. Since the auxiliary source emanates  $^{222}\text{Rn}$  at a constant rate, we increased the total radon budget of the detector to a constant higher level.
- VI 2nd distillation run: at the beginning of this phase, the distillation column's liquid reservoir was filled again with xenon from XENON100. Then, on-line radon distillation was re-started. During this phase, the auxiliary radon emanation source was kept open. Thus, the total radon budget was the same as in phase V. On the 23rd of January, the run was interrupted for about 10 hours due to a power failure in the lab. As a consequence of this incident, the distillation column's liquid reservoir got increased by about 1 kg xenon to about 4 kg in total.
- VII Close auxiliary radon emanation source: the radon distillation was continued. Since the auxiliary emanation source didn't contribute any longer, the total radon budget of XENON100 decreased in this phase (dashed gray line).

##### 4.3.2. Evolution of the $^{222}\text{Rn}$ activity concentration

Before the start of the distillation campaign (phase I in Figure 4.11), we observed a  $^{222}\text{Rn}$  activity concentration of  $(33.4 \pm 1.3) \mu\text{Bq/kg}$ . In Table 4.2, we compare this value to the activity concentrations measured for previous science runs of XENON100 under similar operational modes. The values for the science runs are taken from [61]. For cross-check, we also reproduced the result for 225 live days using our  $\alpha$ -analysis. In phase I, we had the lowest radon contamination measured so far for XENON100 operated in its standard

Time period	$^{222}\text{Rn}$ act. conc. [ $\mu\text{Bq}/\text{kg}$ ]
11 live days (2009)	$138 \pm 3$
100 live days (2010)	$45 \pm 1$
225 live days (2012)	$62.9 \pm 0.8$
distill. campaign (phase I)	$33.4 \pm 1.3$
distill. campaign (phase IV)	$45.4 \pm 1.4$

**Table 4.2.:** Comparison of the averaged  $^{222}\text{Rn}$  activity concentrations measured during the three major science runs of XENON100 and during the distillation campaign under similar detector conditions. Data for the science runs taken from [61].

mode. The variations of the  $^{222}\text{Rn}$  concentration are dominated by diffusive air leaks of the gas system, mostly at the sealing and membranes of the recirculation pump 1. This has been confirmed in studies which could correlate variations of the  $^{222}\text{Rn}$  rate monitored inside the liquid xenon target with the radon concentration measured in ambient air in the lab [61, 87].

During the 1st distillation run in phase III, the radon activity concentration decreased to  $(23.2 \pm 1.7) \mu\text{Bq}/\text{kg}$ , the lowest value ever achieved in XENON100. We understand the radon evolution observed in phase III as the first proof for the successful operation of an on-line RRS at an existing liquid xenon experiment.

The abrupt rise at the beginning of phase IV is explained by the emptying of the distillation column. During the 1st distillation run, radon has been accumulated in the column's liquid xenon reservoir which was then transferred back into XENON100. The accumulated radon in the liquid reservoir originated from the detector's emanation. We expected thus a constant rate in phase IV if all radon would have been transferred back to XENON100 (the emanation equilibrium). Instead, we observed an increasing activity concentration which can be described by the function

$$c_{Rn}(t) = c_0 \cdot (1 - e^{-\lambda_{Rn} \cdot (t-t_0)}) \quad , \quad (4.1)$$

i.e., an ingrowing activity concentration towards a new emanation equilibrium  $c_0$ . Since the distillation column wasn't emptied completely, we explain this evolution by residual radon which stayed inside the column. We obtain a new equilibriums concentration in phase IV of  $c_0 = (45.4 \pm 1.4) \mu\text{Bq}/\text{kg}$  by fit using Eq. (4.1). The gas purification loop in that phase was operated in its standard mode and we can compare this value with the others in Table 4.2. The increased concentration with respect to phase I is obvious and explained by the exchanged recirculation pump 1.

We don't have exact knowledge about the  $^{222}\text{Rn}$  emanation rate during the 1st distillation run (phase III). The radon activity concentration measured in phase IV can be seen as a lower limit, since the emanation of the RRS gas interface (recirculation pump 2) didn't contribute during this phase. Under this assumption, we observed a  $^{222}\text{Rn}$  reduction by a factor of  $D_1 = (1.96 \pm 0.16)$  during the 1st distillation run due to on-line

	$^{222}\text{Rn}$ act. conc. [ $\mu\text{Bq}/\text{kg}$ ]	radon reduct.	
	before distill.	during distill.	$D_i$
1st run	$45.4 \pm 1.4$	$23.2 \pm 1.7$	$1.96 \pm 0.16$
2nd run	$518 \pm 8$	$23.1 \pm 0.7$	$22.4 \pm 0.8$

**Table 4.3.:** Measured  $^{222}\text{Rn}$  reduction inside the XENON100 detector in the two distillation runs. For the 1st distillation run  $c_0$  from phase IV has been assumed as a start concentration (see text for details).

radon removal (see Table 4.3).

Phase V started when we opened the auxiliary radon emanation source. We observed a quick increase of the  $^{222}\text{Rn}$  activity concentration. Since the source was in its emanation equilibrium at the time of opening, the new concentration level stayed constant at  $(518 \pm 8) \mu\text{Bq}/\text{kg}$ . As indicated by the dashed gray line in Figure 4.11, this activity concentration would have stayed constant during phase VI without on-line radon removal. Instead, the radon contamination decreased to  $(23.1 \pm 0.7) \mu\text{Bq}/\text{kg}$ , the same level than we achieved during distillation run1. The observed radon reduction, given by the ratio of the activity concentration measured without and with operating the RRS, is  $D_2 = (22.4 \pm 0.8)$  (see Table 4.3).

The difference between the reduction factors  $D_1$  and  $D_2$  is explained by the composition of the total radon emanation rate with respect to type I and type II sources (see section 2.4.1). From emanation measurements of XENON100 and its purification loop we know that type I sources dominate [62]. This was also the case during the 1st distillation run. The situation was inverted after having inserted the auxiliary emanation source, a type II source, during the 2nd distillation run. While the efficiency of an RRS for type I sources is limited by the recirculation flow the purification effect is much stronger for type II sources which explains the higher reduction  $D_2$  with respect to the 1st distillation run (see section 2.4.1).

At the beginning of phase VII, we closed the auxiliary source but continued on-line radon removal. The gray, dashed line in Figure 4.11 indicates the decreasing radon concentration due to radioactive decay of the radon from the source. Since the monitored  $^{222}\text{Rn}$  activity concentration stayed constant in this phase, we conclude that radon from the auxiliary source was completely removed by the distillation column. This is also indicated by the fact that we measured the same lower level of about  $23 \mu\text{Bq}/\text{kg}$  in both, distillation run1 and run2. In section 4.4 we will use these observations to conclude on the radon reduction capability  $R$  of the distillation column.

### 4.3.3. On the distribution of radon in XENON100

As we discussed in the previous section, we introduced the auxiliary radon emanation source into the gas circulation loop at the beginning of phase V. At the moment of opening the source, the emanated radon was flushed at once into the detector. By monitoring the  $^{222}\text{Rn}$  activity concentration inside the TPC, we could learn how the radon

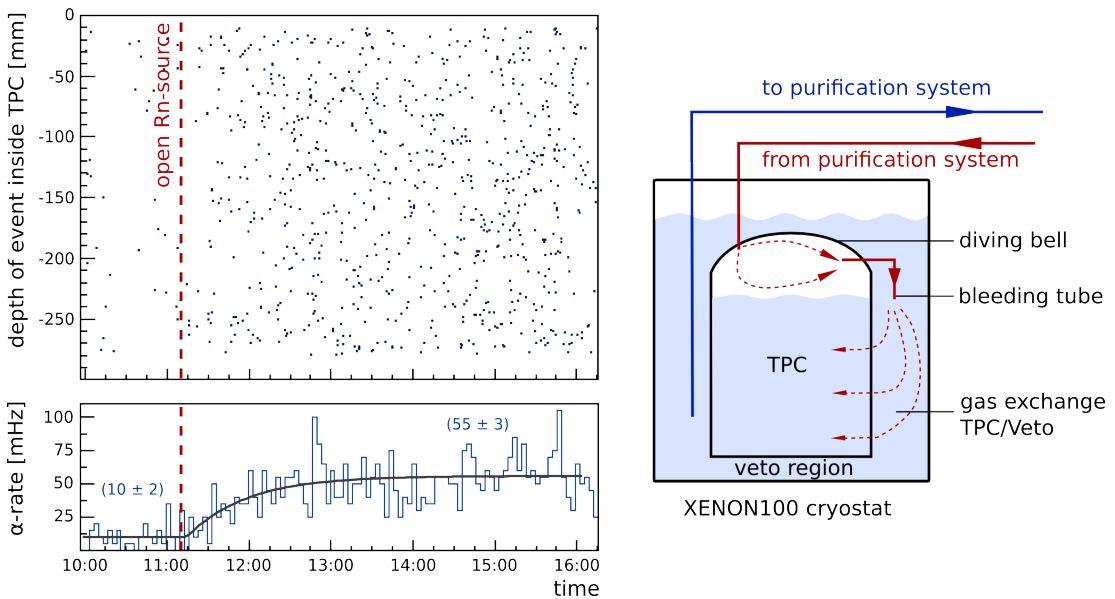


**Figure 4.12.:** (Left) The top panel shows the Z-distribution of  $^{222}\text{Rn}$  and  $^{218}\text{Po}$  events in the TPC at the time when we started to flush through the auxiliary radon emanation source. As shown in the bottom panel, the  $\alpha$ -rate increased slowly and reached the higher equilibrium level after about two hours. (Right) Schematic of the XENON100 cryostat. Most of the injected radon was flushed via the bleeding tube into the veto region.

distributed inside XENON100 and at which timescales it mixed with the xenon target.

### Transport of radon into TPC

The bottom panel in Figure 4.12 shows the evolution of the combined  $\alpha$ -rates from  $^{222}\text{Rn}$  and  $^{218}\text{Po}$  at the time the auxiliary radon source was opened. As we have described in section 1.2.2, the gas from the purification system is flushed directly into the diving bell of the XENON100 detector. Since the vessel which was housing the auxiliary radon source had a volume of about 2.01 only, the full source strength should have reached the bell within a few minutes given the recirculation speed of 4.5 slpm. In Figure 4.12 (bottom panel), however, we observe a slowly increasing  $\alpha$ -rate which reached its equilibrium after about two hours. We conclude, that most of radon was flushed through the so-called bleeding tube into the detector's liquid xenon veto region (see Figure 4.12 (Right)). Thus, the radon entered the TPC from the veto region with a finite exchange flow between both volumes, referred to as  $f_{ex}$ .

In a simple model, we assume a constant  $f_{ex}$ . Furthermore, the radon activity concentrations in the veto region and in the TPC, referred to as  $c_{veto}(t)$  and  $c_{tpc}(t)$ , are considered to be homogeneous in their particular liquid xenon reservoir (we will address this assumption later). The evolution of the absolute radon activity inside the TPC,

$A_{tpc}(t)$ , can be then described by the differential equation

$$\frac{dA_{tpc}(t)}{dt} = -f_{ex} \cdot c_{tpc}(t) + f_{ex} \cdot c_{veto}(t) \quad . \quad (4.2)$$

We can make use of the definition of the activity concentrations in the veto region and the TPC

$$c_{tpc}(t) \equiv \frac{A_{tpc}(t)}{m_{tpc}}$$

$$c_{veto}(t) \equiv \frac{A_{veto}(t)}{m_{veto}} = \frac{A_{tot} - A_{tpc}(t)}{m_{veto}} \quad ,$$

and rewrite the differential equation as

$$\frac{A_{tpc}(t)}{dt} = -\frac{f_{ex}}{m_{tpc}} \cdot A_{tpc}(t) + \frac{f_{ex}}{m_{veto}} \cdot (A_{tot} - A_{tpc}(t)) \quad . \quad (4.3)$$

The masses  $m_{veto}$  and  $m_{tpc}$  are the liquid xenon masses of the veto region and the TPC, respectively, and  $A_{tot}$  is the radon activity in the entire detector (veto region and TPC combined). We can solve Eq. (4.3) to

$$A_{tpc}(t) = A_0 = const. \quad \text{for } t < t_0 \quad ,$$

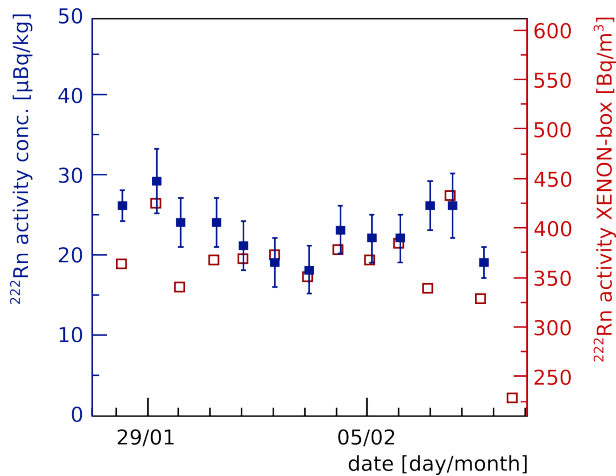
$$A_{tpc}(t) = A_0 + A_s \left( 1 - e^{-\frac{f_{ex} \cdot (m_{tpc} + m_{veto}) \cdot (t - t_0)}{m_{tpc} \cdot m_{veto}}} \right) \quad \text{for } t \geq t_0 \quad , \quad (4.4)$$

where  $A_0$  is the constant activity due to the detector's radon emanation and  $A_s$  is the activity assigned to the auxiliary emanation source. The time of opening the source is labeled as  $t_0$ .

The model in Eq. (4.4) describes our data well and is shown in Figure 4.12 (bottom panel) as the black solid line. For the xenon exchange between veto region and TPC we find  $f_{ex} = (140 \pm 50)$  slpm. This model of the radon transport into the TPC is also supported by the study of a  $^{220}\text{Rn}$  calibration source for the XENON100 detector [88]. This calibration source was connected at the same position in the RRS gas interface as our auxiliary  $^{222}\text{Rn}$  emanation source. After the injection of  $^{220}\text{Rn}$ , a steep rise of the  $\alpha$ -rate within a few minutes was observed (see also [56]). Further studies, however, showed that this instantaneous increase was only due to a small fraction of  $^{220}\text{Rn}$  which directly entered the liquid target after reaching the diving bell. The majority of the thoron was found to be first flushed via the bleeding tube into the veto region.

### Spatial distribution of radon in the TPC

The assumption of a homogeneous  $^{222}\text{Rn}$  concentration is not only used for our model describing the transport of radon into the TPC. Homogeneity is also a basic assumption when we determine the radon activity concentration by means of our  $\alpha$ -analysis and when we model the impact of an RRS in section 2.4.1.



the  $^{222}\text{Rn}$  activity concentration measured in the same time period and using the same time binning. We observe an average radon concentration in ambient air of  $370 \text{ Bq/m}^3$  without any big variations.

In order to estimate the contribution of ambient air to the measured  $^{222}\text{Rn}$  activity concentration in XENON100, we performed a correlation study independent to that developed in [39, 61]. In contrast to the latter, we also need to account for the presence of the RRS. We assume that the observed activity concentration is given by the sum of a constant emanation from the detector and a contribution from ambient air leaking into the system

$$A_{obs}(t) = A_{em} + A_{air}(t) . \quad (4.5)$$

It should be noted that the time dependence of  $A_{obs}(t)$  is only given by the changing contribution from ambient air, i.e. the changing radon concentration measured by the RAD7 monitor (we assume a constant air leak). The radon assigned to emanation sources inside the detector are assumed to be constant in this analysis<sup>4</sup>. We describe the time evolution of  $A_{air}(t)$  by the differential equation

$$\frac{dA_{air}(t)}{dt} = \alpha \cdot A_{\text{RAD7}}(t) - \lambda \cdot A_{air}(t) - f \cdot A_{air}(t) + \frac{f \cdot A_{air}(t)}{R} . \quad (4.6)$$

$A_{\text{RAD7}}(t)$  is the activity concentration measured by the RAD7 monitor. Its contribution to  $A_{obs}(t)$  is suppressed by the leakage factor  $\alpha$ . Once in the detector, the radon from ambient air is reduced by radioactive decay (second term) or it is flushed out of the system and gets reduced by the distillation column (third and fourth term). The reduction factor  $R$  of the RRS has been defined in Eq. (2.14). In the following we simplify Eq. (4.6) by assuming  $R = \infty$ . This assumption will be justified later in section 4.4. The solution of Eq. (4.6) is then

$$A_{air}(t) = A_{air}^0 \cdot e^{-(f+\lambda) \cdot (t-t_s)} + \alpha \cdot \sum_{t'=t_s}^t A_{\text{RAD7}}(t') \cdot e^{-(f+\lambda) \cdot (t-t')} \cdot \Delta t . \quad (4.7)$$

$A_{air}^0$  is the air contribution at the start of RAD7 data taking at  $t = t_s$  and will be treated as a fit parameter. This is necessary since we don't have any knowledge about the radon concentration in the air before the time  $t_s$  and how much radon was brought into the setup. The discrete form of Eq. (4.7) is for convenience as we want to apply this model to our data in Figure 4.13. The time interval  $\Delta t$  represents the bin size of the data. After inserting  $A_{air}(t)$  into Equation 4.5 we have a model to fit to the observed activity concentration inside XENON100  $A_{obs}(t)$  and the RAD7 monitor data  $A_{\text{RAD7}}(t)$ .

The best-fit result ( $\chi^2/\text{ndf} = 7.4/7$ ) is shown in Table 4.14. The constant radon emanation from the detector and the purification system contribute most to the observed  $^{222}\text{Rn}$  activity concentration. From the fit we obtain  $A_{em} = (17 \pm 1) \mu\text{Bq/kg}$ . We want to emphasize that this value is obtained during the 2nd distillation run,

---

<sup>4</sup>We assume here that the detector's emanation is constant but reduced due to the operated RRS.

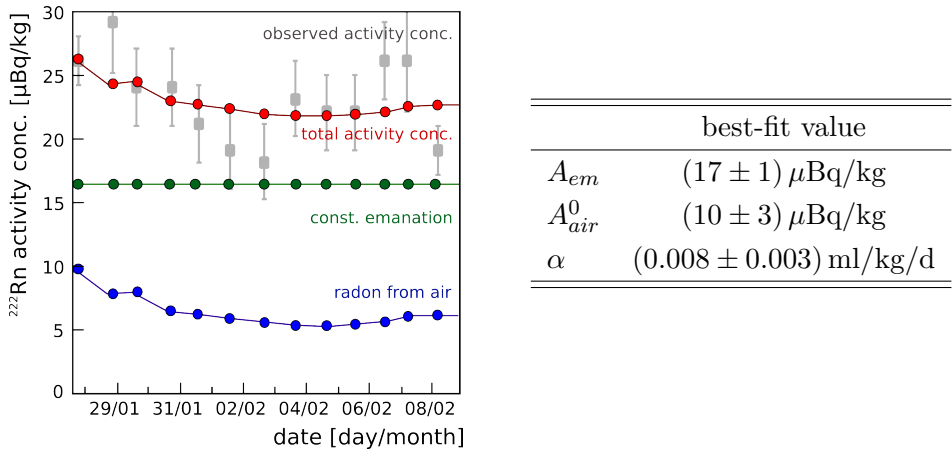


**Figure 4.14 & Table 4.4:** Fit of the model Eq. (4.5) to the  $^{222}\text{Rn}$  activity concentrations in XENON100 and in ambient air. The gray data points correspond to the observed  $^{222}\text{Rn}$  activity concentration in XENON100 as it is also shown in Figure 4.13. The contributions from constant radon emanation and the air leak sum up to the total activity concentration. The best-fit value for the leakage factor  $\alpha$  corresponds to an air leak of  $(1.2 \pm 0.5) \text{ ml}/\text{d}$  at atmospheric pressure.

i.e., when it was reduced due to radon removal. For the leakage factor we obtain  $\alpha = (0.008 \pm 0.003) \text{ ml} \cdot \text{kg}^{-1} \cdot \text{d}^{-1}$ . This corresponds to an air leak of  $(1.3 \pm 0.5) \text{ ml}/\text{d}$  at atmospheric pressure, assuming a liquid xenon reservoir of  $(158 \pm 3) \text{ kg}$  inside XENON100. The large error is explained by the rather flat RAD7 data during the 2nd distillation run. The activity concentration assigned to air at the start of the investigated time period is  $A_{air}^0 = (10 \pm 3) \mu\text{Bq}/\text{kg}$ . This value, however, might be biased from the decreasing activity concentration we observed during phase VI due to the on-line radon removal. In Figure 4.14 we summarize the obtained fit results graphically. In blue we plot the contribution of ambient air to the observed  $^{222}\text{Rn}$  activity concentration. On average, an potential air leak might have increased the concentration by about  $6 \mu\text{Bq}/\text{kg}$ . The green line gives the constant emanation of the system  $A_{em} = (17 \pm 1) \mu\text{Bq}/\text{kg}$  while operating the RRS. According to our model in Eq. (4.5), both, the contributions from the air leak and the constant radon emanation, add up to the total activity concentration (red data-points). For comparison we plot also the observed radon activity during the 2nd distillation run (gray data-points).

The monitoring of the radon in ambient air showed a constant activity concentration of about  $370 \text{ Bq}/\text{m}^3$  during the 2nd distillation run (phases VI and VII). The fit of our model Eq. (4.5) certainly suffers from the limited data. However, we estimated the contribution of radon from ambient air to be about  $6 \mu\text{Bq}/\text{kg}$  while the RRS has been operated. Long term monitoring of the radon concentration in ambient air showed variations of  $\pm 200 \text{ Bq}/\text{m}^3$  at maximum (see [61] for the 225 live days run). Thus, the air leakage induced fluctuations of the radon activity concentration in XENON100 are estimated to be about  $\pm 3 \mu\text{Bq}/\text{kg}$  at maximum. Too small to be used as an alternative

explanation for the decreasing activity concentration observed during both distillation runs. However, we want to emphasize that for the calculation of the observed reduction factors  $D_i$ , we assumed a constant radon contribution from ambient air. Possible fluctuations of  $\pm 3 \mu\text{Bq}/\text{kg}$  haven't been considered in the errors given in section 4.3.2.

#### 4.4. The radon removal capability of the distillation column

In the previous section, we reported on the successful radon reduction in XENON100 due to on-line purification, expressed by the reduction factor  $D_i$ . As a next step, we want to investigate the reduction capability of the distillation column in detail. We have introduced the reduction factor of the RRS in section 2.4.1 as the ratio

$$R := \frac{c_{in}}{c_{out}}, \quad (4.8)$$

where  $c_{in}$  and  $c_{out}$  are referred to as the  $^{222}\text{Rn}$  activity concentrations measured at the distillation column's in-let and out-let, respectively. We want to emphasize the difference to the radon reduction measured inside the detector. While  $R$  is related only to the RRS (here to the distillation column), the observed reduction  $D_i$  is dependent on  $R$ , the types of the emanation sources (type I, type II) and their relative ratio, but also on the flow parameter  $f$ .

In this section, we want to determine  $R$  for our RRS. Since we cannot measure  $c_{in}$  and  $c_{out}$  directly, we use the data acquired during the distillation runs to obtain  $R$  by fitting. Therefore, we use the model discussed in section 2.4.1 with its basic differential equation for the number of radon atoms inside the detector

$$\frac{dN(t)}{dt} = k_1 - f \cdot N(t) - \lambda \cdot N(t) + \frac{k_2 + f \cdot N(t)}{R}. \quad (2.13)$$

The variables  $k_1$  and  $k_2$  describe the  $^{222}\text{Rn}$  emanation rate of type I and type II sources, respectively, while  $f$  parameterizes the recirculation flow through the RRS.

In section 4.4.1, we will describe the observed evolution of the  $^{222}\text{Rn}$  activity concentration during the 2nd distillation run (phases V–VII) using our model Eq. (2.13). We will solve the differential equation stepwise, according to the situation during the corresponding operational phase of the detector system. The reduction capability of the RRS  $R$  and the emanation rates of type I and type II radon sources are fit parameters of the model. For better comparison to data (e.g., to Figure 4.11), we will express the emanation rate as  $^{222}\text{Rn}$  activity concentrations  $c_1$  and  $c_2$ , i.e., normalized to the detector's liquid xenon mass.

In section 4.4.2, we will have a closer look into the data from the 1st distillation run. However, due to larger uncertainties and our limited data, the obtained results are only interpreted as a consistency check.

#### 4.4.1. 2nd distillation run

The 2nd distillation run is of particular interest due to the use of the auxiliary radon emanation source. From its position in the purification loop it is classified as a type II source but unique with regard to the possibility to be switched on/off. In order to distinguish from the constant type II emanation rates we extend Eq. (2.13) to

$$\frac{dN(t)}{dt} = k_1 - f \cdot N(t) - \lambda \cdot N(t) + \frac{k_2 + k_s + f \cdot N(t)}{R} , \quad (4.9)$$

where  $k_s$  is referred to as the emanation rate of the auxiliary radon source. Similar as we did in section 2.4.1, we define for convenience

$$K_s = k_1 + \frac{k_2 + k_s}{R} \quad (4.10)$$

$$K = k_1 + \frac{k_2}{R} \quad (4.11)$$

$$\Lambda = [\lambda + f \cdot (1 - 1/R)] . \quad (4.12)$$

For our fit model we need to solve Eq. (4.9) for the corresponding starting conditions during the phases  $V - VII$ . At the beginning of phase VI, e.g., we had a constant emanation rate form all sources ( $k_1$ ,  $k_2$  and  $k_s$ ). For the solution during phase VII, on the other hand, we need to consider that the auxiliary radon source was closed. Residual radon originating from the source, however, was still present but got reduced by radioactive decay. We obtain for the number of  $^{222}\text{Rn}$  atoms

$$N_V(t) = (k_1 + k_2 + k_s) \cdot \lambda^{-1} = \text{const.} \quad (4.13)$$

$$N_{VI}(t) = \frac{K_s}{\Lambda} + \left( N_V(t_{VI}) - \frac{K_s}{\Lambda} \right) \cdot e^{-\Lambda \cdot (t - t_{VI})} \quad (4.14)$$

$$N_{VII}(t) = \frac{K}{\Lambda} + \left( N_{VI}(t_{VII}) - \frac{K}{\Lambda} \right) \cdot e^{-\Lambda \cdot (t - t_{VII})} , \quad (4.15)$$

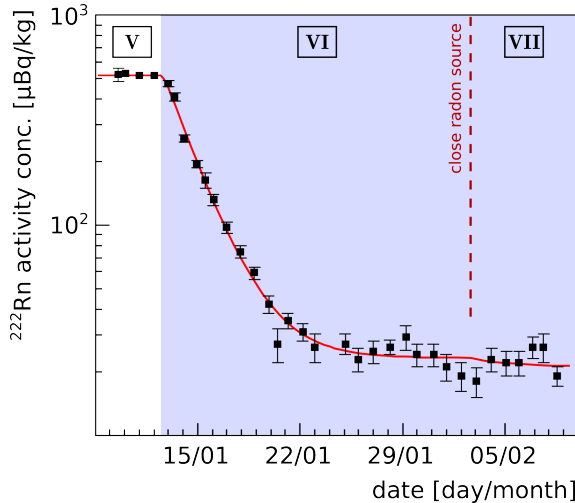
where the times  $t_{VI}$  and  $t_{VII}$  are the starting times of phases VI and VII, respectively. Fit parameters are the emanation rates  $k_1$ ,  $k_2$  and  $k_s$ <sup>5</sup>, the reduction factor  $R$  and the flow parameter  $f$ .

#### Unconstrained fit:

In a first step, we apply our fit model, Eqs. (4.13) to (4.15), to the data without setting any constraints on the fit parameters. The result is shown in Figure 4.15 and Table 4.5. For the type I emanation we find the corresponding activity concentration of  $c_1 = (48 \pm 7) \mu\text{Bq/kg}$ . This value is higher than the total concentration obtained during phase IV

---

<sup>5</sup>As we explained above, we will fit the corresponding activity concentrations  $c_1$ ,  $c_2$  and  $c_s$ .



Fit value	
$c_1$	$(48 \pm 7) \mu\text{Bq}/\text{kg}$
$c_2$	$(230 \pm 70) \mu\text{Bq}/\text{kg}$
$c_s$	$(240 \pm 70) \mu\text{Bq}/\text{kg}$
$R$ best fit	47
$R$ limit	$> 7.8$ (95% C.L.)
$f$	$(3.16 \pm 0.18) \cdot 10^{-6} \text{ s}^{-1}$
$\chi^2/\text{ndf}$	37.73/28

**Figure 4.15 & Table 4.5:** Best fit parameters for the 2nd distillation run without setting any parameter constraints. The lower limit for the reduction factor  $R$  has been determined by means of a  $\chi^2$ -scan shown in Figure 4.16.

indicating that there are additional emanation sources in the extended purification loop including the RRS gas interface. The type II sources,  $c_2 = (230 \pm 70) \mu\text{Bq}/\text{kg}$  and  $c_s = (240 \pm 70) \mu\text{Bq}/\text{kg}$ , are not well determined by the fit. This is explained by the flat  $^{222}\text{Rn}$  activity concentration in phases VI and VII. Since no clear closing-source signature is visible in data, we cannot distinguish between the permanent type II sources of the detector and the auxiliary emanation source. As a result, the fitted source strength is evenly distributed between  $c_2$  and  $c_s$ .

For the flow parameter we find  $f = (3.16 \pm 0.18) \cdot 10^{-6} \text{ s}^{-1}$ . Using the total amount of xenon inside the detector,  $M_{Xe} = (158 \pm 3) \text{ kg}$  (excluding the liquid reservoir inside the distillation column), we calculate for the recirculation speed

$$F_{fit} = \frac{f \cdot M_{Xe} \cdot 60}{\rho_{GXe}} = (5.2 \pm 0.4) \text{ slpm} \quad . \quad (4.16)$$

This value is significantly larger than the mass flow  $F = (4.50 \pm 0.05) \text{ slpm}$ , measured by means of the mass flow controllers in XENON100's gas loop. We conclude that instead of the total xenon mass  $M_{Xe}$  only a fraction of  $(87 \pm 5)\%$  takes part of the gas purification and is looped through the RRS.

For the reduction factor of the RRS, we obtain a best fit value of  $R = 47$  (minimal value of  $\chi^2$ ). Since the uncertainties are large, we wanted to quote a lower limit. Starting at  $R = 1$  (i.e., no reduction), we increased the reduction factor stepwise. For each value of the reduction factor, we repeated the fit, keeping  $R$  fixed and recorded the reduced  $\chi^2$  as a function of  $R$ . We refer to this procedure from now on as  $\chi^2$ -scan. The result is shown in Figure 4.16 (Left). Reduction factors in the range of  $R = 1$  to  $R = 5$  are strongly disfavored by the fit. At about  $R = 10$ , the goodness of fit stays constant at a level

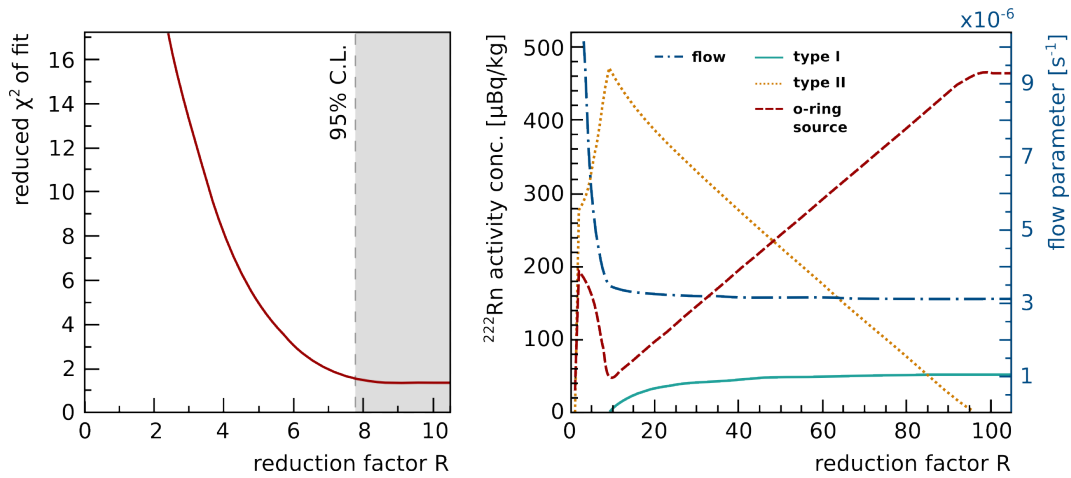


**Figure 4.16.:** (Left) The  $\chi^2$ -minimum as a function of the reduction factor  $R$  as it has been obtained in a  $\chi^2$ -scan. (Right) Evolution of the unconstrained fit parameters as a function of the fixed reduction factor  $R$ .

of  $\chi^2/ndf = 1.35$ . From Figure 4.16, we determine a limit of  $R > 7.8$  at a confidence level of 95%. This limit seems to be surprisingly low given the observed radon reduction inside XENON100 by a factor of  $D_2 = (22.4 \pm 0.8)$ . Thus, we want to have a closer look into the fit values of the other parameters obtained by the  $\chi^2$ -scan. The result is summarized in Figure 4.16 (Right). The sum of all emanation sources is well determined due to the plateau in phase V. Their distribution into type I, type II and the auxiliary radon source differs depending on  $R$ . In order to achieve the observed reduction factor  $D$  even at small values for  $R$ , the type I sources are pushed to 0. Type II sources, on the other hand, are more effectively removed by the RRS and even small  $R$ s can achieve a significant radon reduction inside the detector.

Closing the auxiliary radon source in phase VII triggers the evolution of  $c_s$  in Figure 4.16. The expected decrease of the  $^{222}\text{Rn}$  activity concentration would be maximal for small  $R$  and large  $c_s$ . Since we did not observe significant changes of the radon concentration, the fit pushes  $c_s$  towards small values and thus also allows for small reduction factors. For larger  $R$ , on the other hand,  $c_s$  is preferred with respect to  $c_2$ . In order to achieve a large radon reduction with small values of  $R$ , a large flow parameter  $f$  is favored. For  $R > 10$ , the flow parameter is stable at  $f = 3.2 \cdot 10^{-6} \text{ s}^{-1}$ . It is constraint by the decreasing  $^{222}\text{Rn}$  activity concentration observed in phase VI.

#### Fit using constraint $c_s$ :

Based on our monitoring of the  $\alpha$ -activity while opening the auxiliary emanation source, we motivate a constraint on the fit parameter  $c_s$ . From Figure 4.12 we conclude that about 80% of the increased activity concentration can be assigned to the radon source. This justifies a lower limit of  $c_s > 400 \mu\text{Bq}/\text{kg}$ .

The result of the constraint fit is shown in Figure 4.17 and Table 4.6. The red line

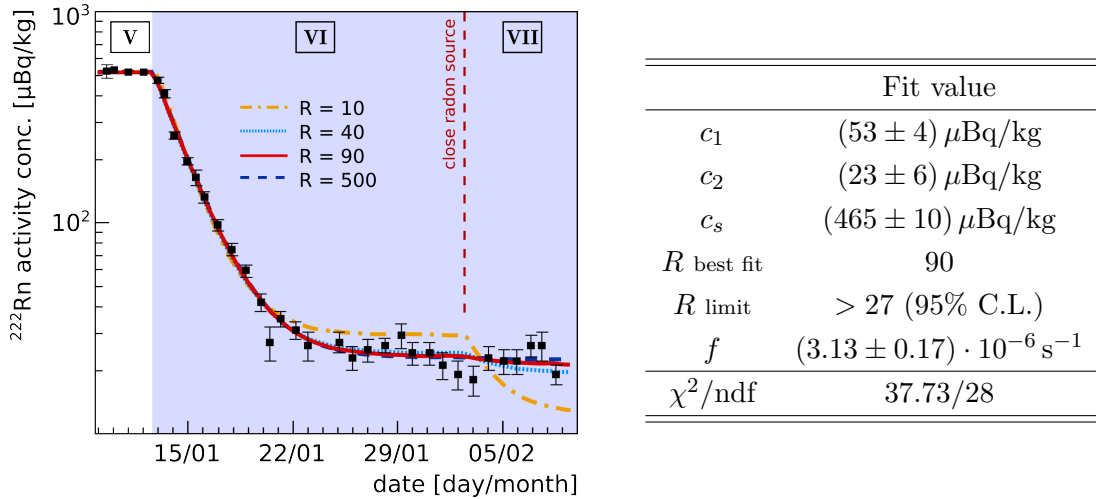


**Figure 4.17 & Table 4.6:** Best fit parameters for the 2nd distillation run. In this fit, we constraint the contribution of the auxiliary emanation source to  $c_s > 400 \mu\text{Bq}/\text{kg}$ .

is our model using the best fit parameters. The value obtained for type I sources,  $c_1 = (53 \pm 4) \mu\text{Bq}/\text{kg}$ , is in agreement with the results from the unconstrained fit. The same is true for the flow parameter  $f = (3.13 \pm 0.17) \cdot 10^{-6} \text{ s}^{-1}$ . In case of the type II sources, we find  $c_2 = (23 \pm 6) \mu\text{Bq}/\text{kg}$  for the permanent type II emanation and  $c_s = (465 \pm 10) \mu\text{Bq}/\text{kg}$  assigned to the auxiliary emanation source. The total permanent emanation rate is given by  $c_1 + c_2 = (76 \pm 7) \mu\text{Bq}/\text{kg}$ , significantly higher than the emanation rate during phase IV where the purification loop has been operated in the standard loop. This might be explained by emanation sources located in the RRS gas interface or in the distillation column which both have been bypassed during phase IV.

The best fit value for the reduction factor is  $R = 90$  (minimum  $\chi^2$ -value). Due to the large uncertainties of  $R$  we performed another  $\chi^2$ -scan which determined a lower limit of  $R > 27$  at 95% confidence level.

For illustration, we show in Figure 4.17 the fit results when fixing the reduction factor to  $R = 10$ ,  $R = 40$  and  $R = 500$  (the red line  $R = 90$  corresponds to the global best fit value). For  $R = 10$ , we observe a clear mismatch of the model and our data. With an increasing reduction factor, a significant decrease of the activity concentration at the beginning of phase VII (close auxiliary source signature) gets more and more suppressed. Thus, we cannot distinguish between higher reduction factors based on our data and only quote a lower limit of  $R > 27$  (95% C.L.) as our final result.

#### 4.4.2. 1st distillation run

The fact that we don't know the  $^{222}\text{Rn}$  activity concentration without the impact of the RRS makes it hard to analyze the 1st distillation run. During phase I, the purification loop has been operated without the RRS gas interface and the distillation column, similar

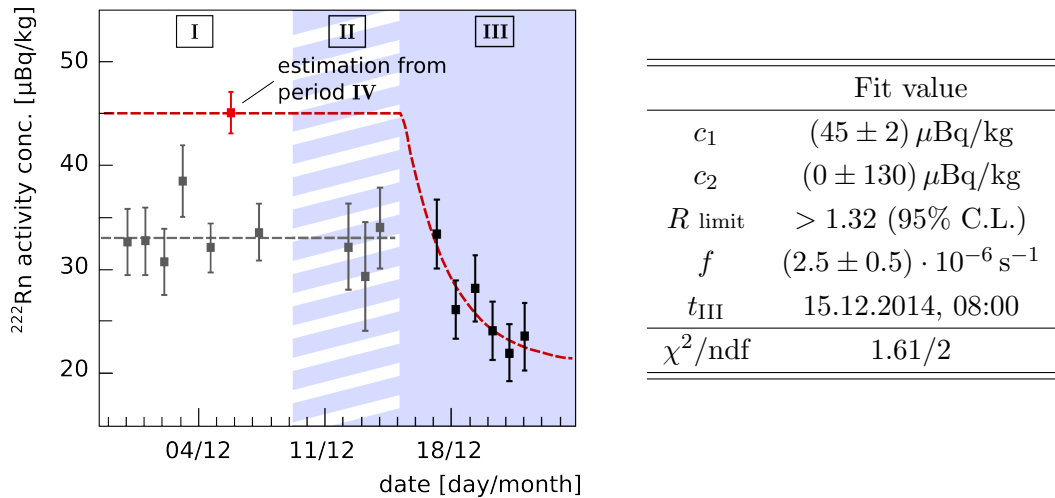


**Figure 4.18 & Table 4.7:** Fit results for the 1st distillation run. In order to estimate the  $^{222}\text{Rn}$  activity concentration without purification, we use the result obtained in phase IV (red data point).

as during phase IV. Nevertheless, we can use the measurement of phase IV as a lower limit for the radon activity concentration without an RRS. For convenience, we thus assume for phases I and II a constant activity concentration of  $c_1 + c_2 = (45.4 \pm 1.4) \mu\text{Bq}/\text{kg}$  (i.e., the phase IV equilibrium activity concentration) instead of the actually measured values. This gives us the fit model

$$N_{\text{I},\text{II}}(t) = k_1 + k_2 = \text{const.} \quad (4.17)$$

$$N_{\text{III}}(t) = \frac{K}{\Lambda} + \left( N_{\text{I}}(t_{\text{III}}) - \frac{K}{\Lambda} \right) \cdot e^{-\Lambda \cdot (t - t_{\text{III}})} . \quad (4.18)$$

During phase II, the RRS was shortly operated (until the pump failure) and stopped again. Thus, the actual start of the 1st distillation run is not well defined and we leave  $t_{\text{III}}$  as a free parameter. In Figure 4.18 and Table 4.7 the fit results are shown. The fact that the contribution from type II sources vanishes, might indicate again that we underestimate the total radon activity concentration without purification. For the reduction factor, we can quote only  $R > 1.32$  at 95% confidence level. The flow parameter  $f$ , on the other hand, is well determined and in agreement with our results obtained for the 2nd distillation run.

## 4.5. Radon removal system for XENON1T

In the last section, we want to discuss the development of an on-line RRS for the XENON1T detector. In principle, the RRS successfully tested at XENON100, can be adopted for the XENON1T experiment. The handling of the high purification flow, necessary for an efficient removal of electronegative impurities and type I radon, is the most

#### 4. Operation of a distillation based radon removal system at XENON100

---

		<b>mBq</b>			<b>mBq</b>
<b>type I</b>			<b>type II</b>		
	250 mm pipe	$9.2 \pm 1.0$		getters	$1.60 \pm 0.10$
	100 mm pipe	$2.64 \pm 0.19$		QDrives II <sup>a</sup>	$7.0 \pm 0.3$
	cryo-system	$2.4 \pm 0.3$			
	procubine	$2.1 \pm 0.3$			
	inner vessel	$1.9 \pm 0.3$			
	TPC	$4.8 \pm 2.2$			
	QDrives I <sup>a</sup>	$7.0 \pm 0.3$			
<b>sum type I:</b>		<b><math>30.0 \pm 2.5</math></b>			<b><math>8.60 \pm 0.32</math></b>

**Table 4.8.:** Distribution of type I and type II radon emanation sources for scenario 1 (see Figure 4.19) for the realization of an RRS for the XENON1T experiment.

<sup>a</sup> We assume an additional set of QDrive pumps needed to flush xenon from the distillation column back into the detector.

challenging task. The distillation column that we used during the XENON100 distillation campaign is suitable for mass flows up to 18 slpm [57]. The purification flow in the XENON1T experiment is required to be in the range of  $F = 50$  slpm to 100 slpm. Thus, the construction of a high-flow radon distillation column is currently under investigation. One possibility is the parallel operation of several smaller distillation columns. This scenario is included when we hereafter talk about high-flow radon distillation columns.

We want to use the results of our  $^{222}\text{Rn}$  emanation measurements, discussed in section 2.2, to study the impact of an RRS on the radon budget in XENON1T. In our first scenario 1, we assume a similar experimental setup as we investigated during the distillation campaign at XENON100, i.e., the RRS is part of the gas purification loop (see Figure 4.19). Xenon from the liquid reservoir is evaporated in the heat exchanger and then pumped from the detector through the getters into the RRS by means of two QDrive pumps (QDrives II<sup>6</sup>) of the XENON1T purification system. In this scenario a second pair of QDrive pumps (QDrives I) is needed to push the purified xenon from the RRS back to XENON1T. We assume that all pumps have the same  $^{222}\text{Rn}$  emanation rate. In Table 4.8, all known emanation sources of scenario 1 are classified regarding type I and type II. Summing up to an emanation of  $(30.0 \pm 2.5)$  mBq, the type I sources clearly dominate the total radon budget. A rate of  $(8.60 \pm 0.32)$  mBq is assigned to type II emanation. In order to estimate the achievable radon reduction, we use Eqs. (2.16). If we assume  $R = 27$  for the high flow RRS which is operated at  $F = 100$  slpm, we find in this scenario a reduction of  $D = 3.1$  for XENON1T. The reduction is strongly limited by the dominating type I sources. Even at infinite reduction  $R = \infty$ , we only reduce the radon concentration inside the detector by about  $D = 3.2$ .

We can increase the impact of our RRS if we manage to transform some of the type I

<sup>6</sup>The roman numeral indicates the emanation type of the pumps.

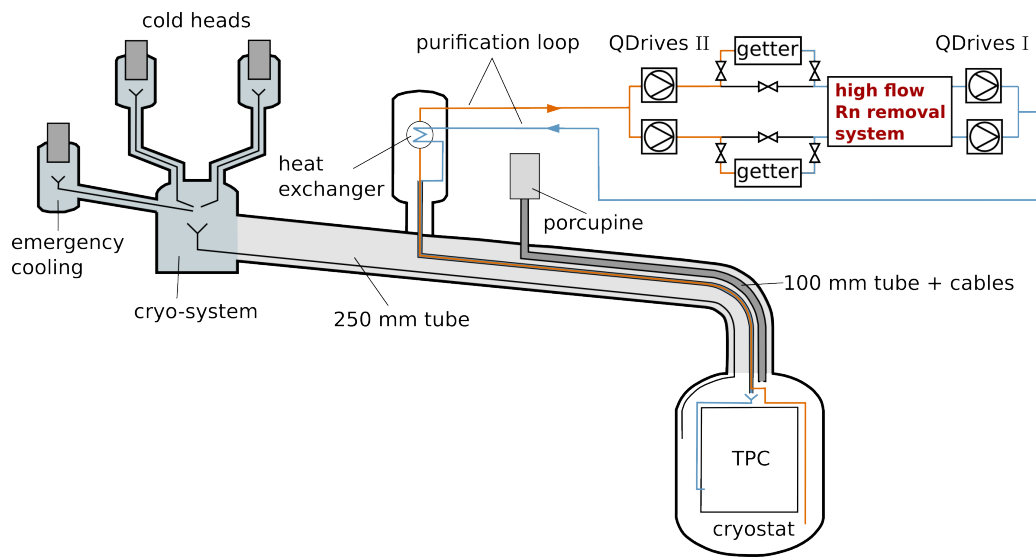


**Figure 4.19.:** In scenario 1 an RRS is included in the main purification loop of XENON1T. Additional QDrive pumps (QDrives I) are necessary to push the purified xenon from the RRS through the getters and back into the detector. In this scenario the RRS is operated at mass flows up to 100 slpm.

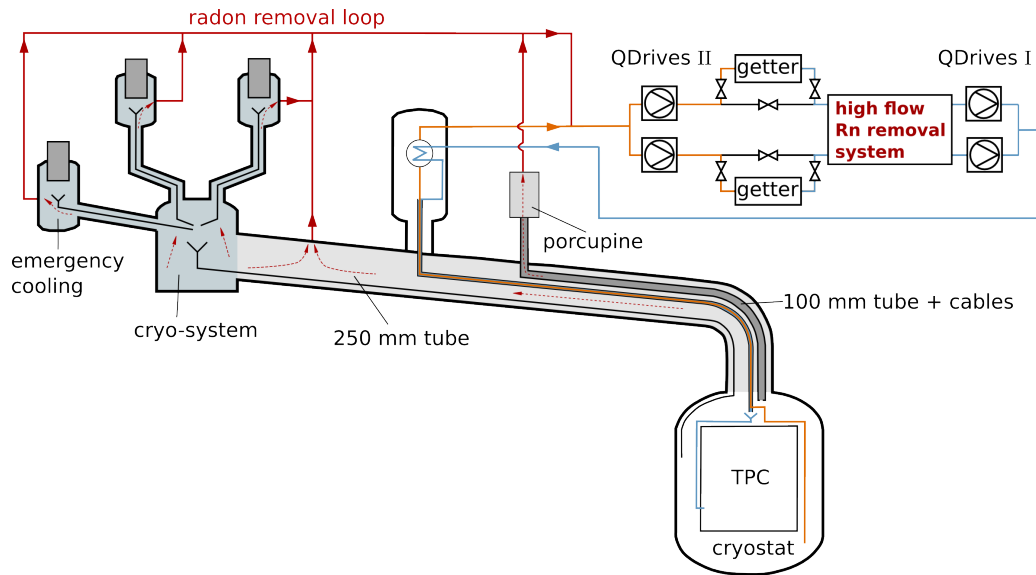


**Figure 4.20.:** In scenario 2 additional gas ports at the detector enable us to transform original type I into type II emanation sources. Via the radon removal loop radon enriched xenon gas is flushed from these gas ports to the gas purification loop and the RRS.

sources into type II, i.e., preventing radon from type I sources to enter the liquid xenon target prior to passing the RRS. In Figure 4.20 we show a possible scenario 2 for the XENON1T detector. Similar as we did for the integral emanation measurement discussed in section 2.3.3, we can make use of several ports to extract radon enriched xenon gas and flush it via a so-called radon removal loop into the RRS. We know that the biggest type I emanation sources are the 250 mm and the 100 mm tube. If we are able to flush out the emanated radon before it can enter the liquid xenon target, it is reclassified as type II emanation. In scenario 2 we assume that only the inner vessel, the TPC and the QDrives I are treated as type I sources. Their combined emanation rate sums up to 13.7 mBq (see Table 4.8). The residual sources have been transformed to type II sources which now dominate the total radon budget with an emanation rate of 24.9 mBq. Assuming  $R = 27$ , the expected reduction in scenario 2 is  $D = 6.3$ .

Both of the previous scenarios require a so-called high flow RRS operated at mass flows up to 100 slpm. As we have pointed out earlier, the cryogenic distillation column used during the radon distillation campaign, however, can process only about 18 slpm at maximum [57]. In scenario 3 we investigate the radon removal potential of such a low flow RRS for XENON1T. As shown in Figure 4.21 we make use of the radon removal loop as introduced in the previous scenario 2. Since this loop is only dedicated to purify the xenon gas in the cryo-system and piping, it can be operated at much smaller flow rates with respect to the main purification loop. Thus, even our existing distillation column is thought to be suitable for its use as a low flow RRS to purify the xenon from the radon removal loop. After purification, the radon clean xenon is circulated via the main purification loop back into the detector. In order to estimate the radon reduction achievable for scenario 3, we classify as type I sources the inner vessel, the TPC but also the QDrive pumps I and the getters which are located after the RRS. Radon emanation from the cryo-system, piping and porcupine is considered as pure type II due to the radon removal loop. Since for the radon loop only small flow rates are required, we use alternative recirculation pumps which are known to have a negligible low emanation rate with respect to the QDrive pumps (e.g., < 0.3 mBq for the XENON100 recirculation pump [62] produced by the KNF company). In this scenario, we thus assign an emanation rate of 15.3 mBq to type I and 16.3 mBq to type II sources. Assuming a reduction capability of  $R = 27$ , we expect a radon reduction of  $D = 4.8$ . This reduction is certainly lower than for the high flow RRS, however, it might be achievable with our existing distillation column.

Figure 4.22 shows the last scenario 4 we want to discuss. Similar as before, radon enriched xenon gas is flushed via the radon removal loop out of the XENON1T detector in order to transform type I into type II sources. In this scenario, we also use a low flow RRS but the purified xenon re-enters the detector via the ports at the cold-heads. The xenon is then liquefied and brought via a pipe directly into the liquid xenon reservoir without getting into contact with radon enriched gas, e.g., in the 250 mm pipe. The advantage of this scenario with respect to scenario 3 is that a stable circulation loop might establishes between the purified liquid xenon dropping downwards and the evaporating xenon from the cryostat which flushes along the pipes upwards towards the RRS. Since

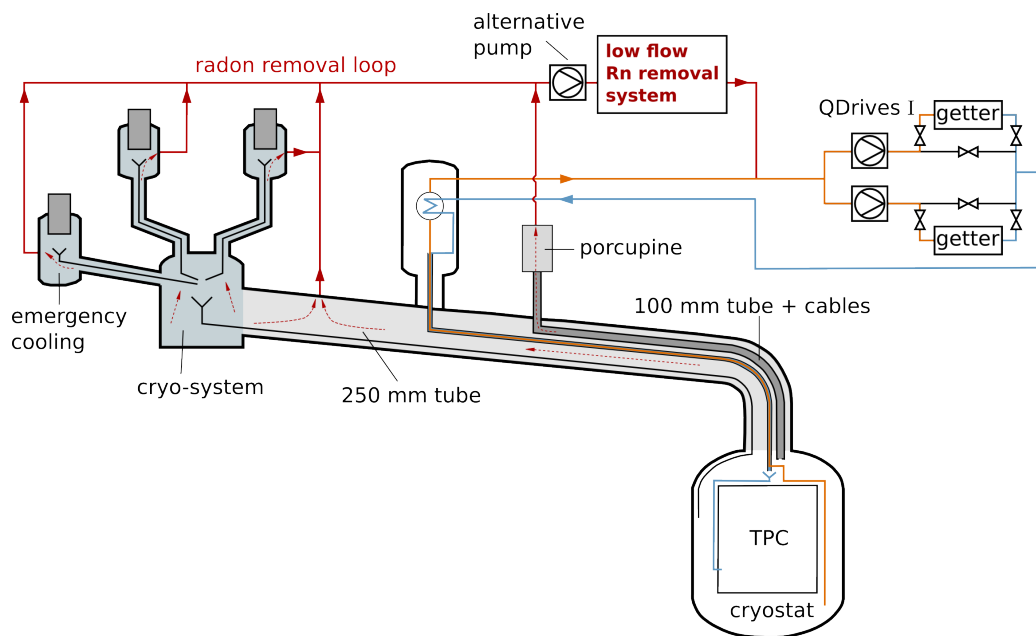


**Figure 4.21.:** In scenario 3 additional gas ports at the detector enable us to transform type I into type II emanation sources. Via the radon removal loop, radon enriched xenon gas is flushed from these gas ports to the gas purification loop and the RRS.

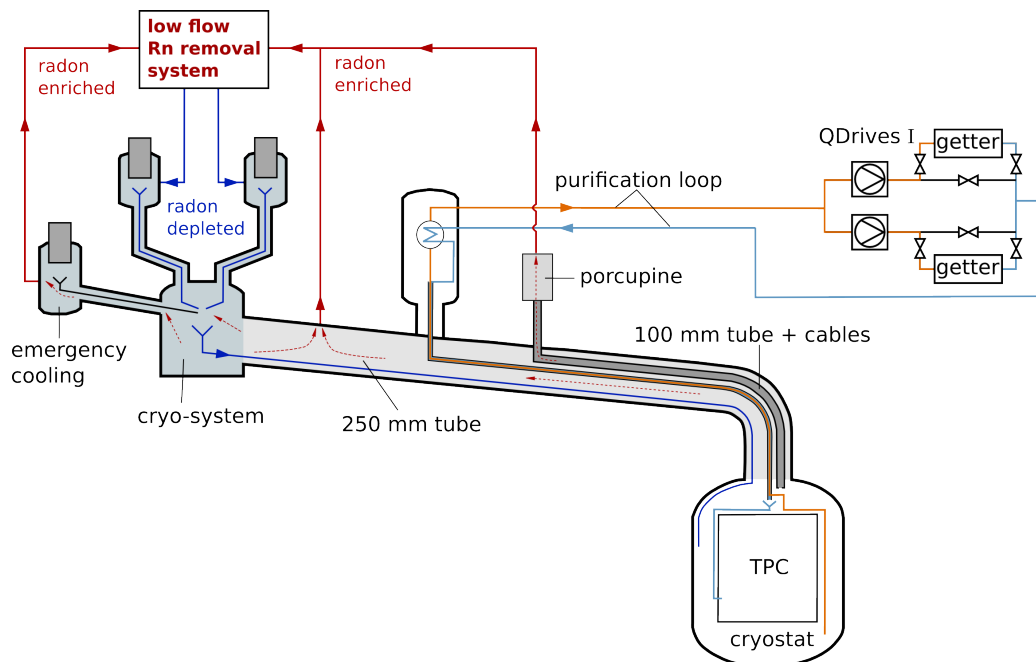


**Figure 4.22.:** In scenario 4 a low flow RRS is used. The purified xenon re-enters the detector at its cold-heads and is flushed into the cryostat after liquefaction. Xenon evaporating at the liquid surface is pushed upwards, transporting the emanated radon towards the RRS.

the distribution of type I and type II sources is identical to the previous scenario (low flow RRS option), we obtain the same reduction factor of  $D = 4.8$  assuming  $R = 27$ .

## 4.6. Summary and conclusions

The goal of this chapter was to proof the suitability of cryogenic distillation to be used in an on-line  $^{222}\text{Rn}$  removal system for liquid xenon detectors. During the XENON100 radon distillation campaign, we extended the detector's gas purification loop by a cryogenic distillation column. The high energetic  $\alpha$ -decays of  $^{222}\text{Rn}$  and its progenies are clearly visible in XENON100 which enabled us to monitor the radon activity concentration with time. In two distillation runs we operated the radon removal system continuously for about one month. We observed a significant reduction of the radon activity concentration in XENON100. In contrast to standard distillation, including the krypton removal from xenon, radon distillation is completely lossless in terms of xenon. Radon disintegration replaces the extraction of highly enriched xenon off-gas from the column. Before the start of the 2nd distillation we increased the  $^{222}\text{Rn}$  activity concentration in XENON100 by means of an auxiliary radon emanation source located in the detector's gas loop. When operating the radon removal system, the  $^{222}\text{Rn}$  activity concentration in the detector decreased by a factor of  $D_2 = (22.4 \pm 0.8)$ . From this, we determined a lower limit for the distillation column's radon reduction capability, expressed by the ratio of the activity concentrations at the gas inlet and outlet of the column, of  $R \equiv c_{in}/c_{out} > 27$  at a confidence level of 95%.

We proofed cryogenic distillation to be a suitable and powerful technique for on-line purification of xenon from radon. We have also seen, however, that the purification gas-flow plays an important role for the radon reduction eventually reached inside the detector. For future experiments, such as XENON1T and XENONnT, we should follow two general strategies for an efficient radon removal system: high exchange rate of the liquid xenon target through the radon removal system and preventing the radon from reaching the liquid xenon target, e.g., by extra purge flows of detector components having a high emanation rate by means of a dedicated radon removal loop. Then, our scenarios show that a radon reduction by a factor of  $D > 4$  is achievable.

# Chapter 5

## Summary and conclusions

In the last decade, an increasing number of experiments have been developed and launched in order to detect dark matter which is thought to make up about 27% of our Universe's total energy content. WIMPs, i.e., weakly interacting massive particles, are one dark matter candidate well motivated by theory. So-called direct detection experiments search for the rare interactions of WIMPs with the nucleons of the detector's target material. Liquid xenon is a powerful detection medium due to its scintillation properties, its large atomic mass and the absence of short-lived radioactive isotopes. At the time, experiments based on liquid xenon have set the most stringent limits for the spin-independent WIMP-nucleon cross-section for WIMP masses above  $5 \text{ GeV}/c^2$ , reaching a minimum of  $\sigma = 1.1 \cdot 10^{-46} \text{ cm}^2$  ( $50 \text{ GeV}/c^2$  WIMP mass) [36]. The XENON1T experiment is one representative of liquid xenon based dark matter detectors [42]. It is taking data since October 2016 and aims to increase the sensitivity for the spin-independent WIMP-nucleon cross-section by another order of magnitude with respect to the present state.

In order to reach these high sensitivities, it is essential to mitigate all kind of backgrounds which might mimic WIMP-nucleon interactions. The radioactive noble gas  $^{222}\text{Rn}$  is known to be the dominating background source in XENON1T [42]. Due to trace amounts of the mother isotope  $^{226}\text{Ra}$ ,  $^{222}\text{Rn}$  is permanently produced in the detector's materials and reaches the liquid xenon target by means of emanation. As a noble gas,  $^{222}\text{Rn}$  distributes homogeneously inside the xenon where the subsequent  $\beta$ -decays cause dangerous background for the WIMP search.

In the course of this thesis, we discussed two strategies to mitigate  $^{222}\text{Rn}$  induced background in liquid xenon based dark matter experiments: material selection based on radon emanation measurements and active  $^{222}\text{Rn}$  removal to continuously purify the liquid xenon target.

Before the assembly of the XENON1T, samples of construction materials and whole sub-components of the detector have been measured for their  $^{222}\text{Rn}$  emanation rate using miniaturized proportional counters. These measurements enabled us to search for

## 5. Summary and conclusions

---

alternative materials, having a lower radon emanation rate, but also to identify the location of the individual emanation sources inside the detector. Within the framework of this thesis, we measured the  $^{222}\text{Rn}$  emanation rate of the fully assembled XENON1T detector. As the detector had been exposed to xenon, the large out-gassing prevented us from using proportional counters. Instead, we employed electrostatic radon monitors which have been calibrated and characterized within this thesis. We found an emanation rate of  $(19.3 \pm 2.1) \text{ mBq}$  for the entire XENON1T detector (excluding the purification system). By comparing this result with previous measurements, we found an emanation rate of  $(4.8 \pm 2.2) \text{ mBq}$  for the detector's fully assembled TPC (time projection chamber). Furthermore, we identified the cryogenic pipe, connecting the detector's cryostat to the cryogenic system, as the largest radon emanation source in XENON1T.

Since radon preferentially enters the liquid xenon target, no common shielding method can reduce its background contribution. However, a permanent (on-line) purification of the xenon target from radon could eventually achieve further mitigation. In this thesis we followed the idea of a radon removal system (RRS) integrated into the detector's gas purification loop as proposed in [70]. Therein, the authors plan to use radon adsorption in an activated carbon filled column at cryogenic temperatures as a purification technique. According to [62], however, an adsorption based RRS implicates several challenges, e.g., the radon emanation of the activated carbon or high xenon adsorption.

In this thesis, we investigated the suitability of cryogenic distillation to be used in an on-line operated RRS. As a first step, we demonstrated the  $^{222}\text{Rn}$  depletion in xenon boil-off gas with respect to the corresponding liquid xenon reservoir. In multiple runs, we filled and liquefied radon enriched xenon into a cryostat (HeXe setup). Then, we emptied the cryostat again by continuously extracting the boil-off gas while simultaneously measuring its radon concentration. In all runs, we measured a  $^{222}\text{Rn}$  reduction by a factor  $\gtrsim 4$ , independent on the probed radon concentrations in the liquid xenon reservoir and extraction mass flows (recuperation flow). Since our setup is understood as a single stage distillation, our measurements demonstrated for the first time that cryogenic distillation is suitable to separate radon from xenon even at concentrations down to the  $10^{-15} \text{ mol/mol}$  level. Our main results have been published in [77].

During a radon distillation campaign employing the XENON100 detector, we realized an on-line RRS based on cryogenic distillation at a running dark matter experiment. In preparation of the campaign, we extended XENON100's gas purification loop by a distillation column which originally was designed for krypton removal at the XENON1T experiment [57]. For the column's usage as an RRS, only minor changes were necessary [91]. In two distillation runs, we could demonstrate for the first time the operation of an on-line radon removal for liquid xenon based detectors. Since the trapped radon decays inside the distillation column, we could operate the radon distillation without any xenon losses. We found for the RRS a radon reduction power, defined as the ratio of the radon concentration at the inlet and outlet of the RRS, of  $R > 27$  (95% C.L.). Depending on the position of the radon emanation sources within the detector and its purification loop, i.e., how fast the emanated radon could be transported into the RRS,

---

their contribution to the total emanation was reduced up to the determined factor  $R$ . We have published our main results also in [85].

In principle, the RRS tested at XENON100 can be upscaled for its use at the XENON1T experiment. However, since the liquid xenon reservoir to be purified is more than a factor of 10 larger, also the gas circulation speed through the RRS needs to be increased with respect to the XENON100 test. At the time of writing, cryogenic distillation columns which can purify xenon with the required process speed and at the required low concentrations are not available. As described in this thesis, we therefore propose to make use of our knowledge about the locations of the different radon emanation sources within the XENON1T detector. By means of dedicated purge flows, it should be possible to prevent parts of the radon to enter the detector's liquid xenon phase. The radon enriched xenon is instead directly flushed into the RRS where it gets purified. This would enable us to achieve a significant radon reduction while operating the distillation column at currently achievable process speeds. Both options, cryogenic distillation at process speeds up to 100 slpm and dedicated radon purge flows, are the subject of ongoing studies relevant for XENON1T but also for the upcoming successor, the XENONnT experiment.

# Appendices

# Appendix A

## Gas analytics for radon monitor measurements

The quadrupole mass spectrometer (QMS) used in this work has been characterized in [92]. After the 2nd integral emanation measurement, we analyzed a gas sample from the extracted gas taken directly from the HP-RaMon radon monitor. The result is shown in Figure A.1. Since we used nitrogen as a carrier gas  $N_2$  is clearly visible in the mass spectrum. There are also peaks assigned to double and triple ionized  $N_2$ . Furthermore, we identify the xenon isotopes  $^{129}\text{Xe}$ ,  $^{131}\text{Xe}$ ,  $^{132}\text{Xe}$ ,  $^{134}\text{Xe}$  and  $^{136}\text{Xe}$  (only double ionization peaks are shown). The mass spectrum indicates also argon and carbon dioxide. Not identified are the peaks at masses  $m = 29$  and  $m = 30$ .

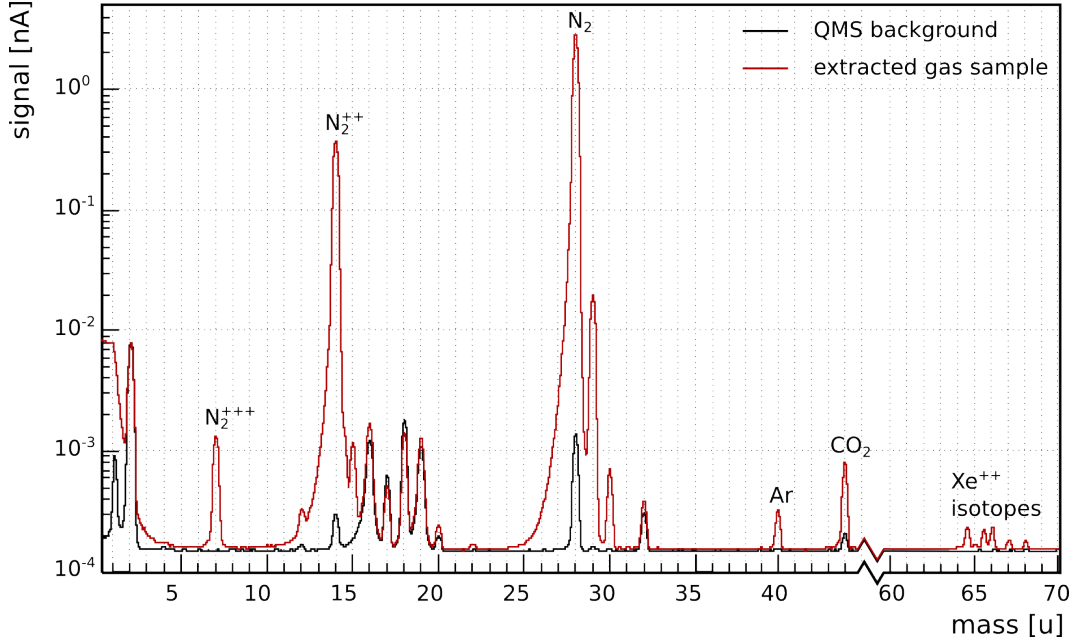


**Figure A.1.:** Analysis of a gas sample extracted for the integral emanation measurement of XENON1T.

# Appendix B

## Derivation of the boil-off reduction factor from Raoult's law

We assume a liquid reservoir of a xenon/radon binary mixture. The boil-off gas phase above the liquid is in its equilibrium and also a binary gas mixture according to the xenon/radon vapor pressures. The mole fractions in the liquid phase are referred to as  $x_{Xe}$  (xenon) and  $x_{Rn}$  (radon), respectively. For the gas phase, we similarly introduce the mole fractions  $y_{Xe}$  (xenon) and  $y_{Rn}$  (radon). In both phases

$$x_{Xe} + x_{Rn} = 1 \quad (B.1)$$

$$y_{Xe} + y_{Rn} = 1 , \quad (B.2)$$

must be fulfilled. In section 2.4.2, the radon reduction factor achieved by a single stage distillation was referred to as  $R$ . In the context of Eq. (B.1), we can write

$$R = \frac{x_{Rn}}{y_{Rn}} . \quad (B.3)$$

According to Dalton's law of partial pressures, the gas pressure  $P(t)$  above the liquid reservoir, i.e., the vapor pressure of the binary mixture, is given by

$$P(t) = p_{Xe}(t) + p_{Rn}(t) , \quad (B.4)$$

where  $p_{Xe}(t)$  and  $p_{Rn}(t)$  are the partial vapor pressures of xenon and radon, respectively. Using Raoult's law, we can write the partial vapor pressures (at a defined temperature) as a function of the liquid mole fraction as

$$p_{Xe} = x_{Xe} \cdot p_{Xe}^* \quad (B.5)$$

$$p_{Rn} = x_{Rn} \cdot p_{Rn}^* , \quad (B.6)$$

---

where  $p_{Xe}^*$  and  $p_{Rn}^*$  are the saturation vapor pressures of pure xenon and pure radon, respectively. Similarly as we did in section 2.4.2, we define the volatility as

$$\alpha \equiv \frac{p_{Xe}^*}{p_{Rn}^*} . \quad (\text{B.7})$$

Using Eq. (B.1) and Raoult's law Eq. (B.5) we can write

$$p_{Xe} = (1 - x_{Rn}) \cdot p_{Xe}^* . \quad (\text{B.8})$$

Starting with Dalton's law, we find

$$P = p_{Xe} + p_{Rn} = (1 - x_{Rn}) \cdot p_{Xe}^* + x_{Rn} \cdot p_{Rn}^* ,$$

and thus

$$x_{Rn} = \frac{1}{\alpha - 1} \cdot \left( \frac{P}{p_{Xe}^*} - 1 \right) . \quad (\text{B.9})$$

For the pressure  $P$  we find on the other hand

$$P = p_{Xe} + p_{Rn} = (1 - x_{Rn}) \cdot p_{Xe}^* + y_{Rn} \cdot P , \quad (\text{B.10})$$

where we made use of the relation  $p_{Rn} = y_{Rn} \cdot P$ . Thus, we find for the pressure

$$P = \frac{(1 - x_{Rn}) \cdot p_{Xe}^*}{1 - y_{Rn}} . \quad (\text{B.11})$$

Eqs. B.9 and B.11 and the definition of R B.3 give the relation

$$R = \alpha - y_{Rn} \cdot (\alpha - 1) . \quad (\text{B.12})$$

In the limit of negligible  $y_{Rn}$ , above equation simplifies to  $R = \alpha$  as we discussed in section 2.4.2.



## Bibliography

- [1] Teresa Marrodn Undagoitia and Ludwig Rauch. Dark matter direct-detection experiments. *J. Phys., G43*, 2016.
- [2] Jaan Einasto. Dark Matter. *Braz. J. Phys.*, 43:369–374, 2013.
- [3] Katherine Garrett and Gintaras Duda. Dark Matter: A Primer. *Adv. Astron.*, 2011:968283, 2011.
- [4] M. Milgrom. A modification of the Newtonian dynamics as a possible alternative to the hidden mass hypothesis. *Astrophys. J.*, 270, 1983.
- [5] K. G. Begeman et al. Extended rotation curves of spiral galaxies - Dark haloes and modified dynamics. *Mon. Not. Roy. Astron. Astrophys. J.*, 638, 1991.
- [6] V. C. Rubin et al. Extended rotation curves of high-luminosity spiral galaxies. IV - Systematic dynamical properties, SA through SC. *Astrophys. J.*, 225, 1978.
- [7] Matthias Bartelmann and Peter Schneider. Weak gravitational lensing. *Phys. Rept.*, 340:291–472, 2001.
- [8] Dragan Huterer. Weak lensing, dark matter and dark energy. *Gen. Rel. Grav.*, 42:2177–2195, 2010.
- [9] Douglas Clowe, Marusa Bradac, Anthony H. Gonzalez, Maxim Markevitch, Scott W. Randall, Christine Jones, and Dennis Zaritsky. A direct empirical proof of the existence of dark matter. *Astrophys. J.*, 648:L109–L113, 2006.
- [10] Raphael Gavazzi, Tommaso Treu, Jason D. Rhodes, Leon Ve Koopmans, Adam S. Bolton, Scott Burles, Richard Massey, and Leonidas A. Moustakas. The Sloan Lens ACS Survey. 4. The mass density profile of early-type galaxies out to 100 effective radii. *Astrophys. J.*, 667:176–190, 2007.
- [11] Scott W. Randall and Maxim Markevitch and Douglas Clowe and Anthony H. Gonzalez and Marusa Bradac. Constraints on the Self-Interaction Cross Section of Dark Matter from Numerical Simulations of the Merging Galaxy Cluster 1E 065756. *The Astrophysical Journal*, 679(2):1173, 2008.

## Bibliography

---

- [12] Felix Kahlhoefer, Kai Schmidt-Hoberg, Mads T. Frandsen, and Subir Sarkar. Colliding clusters and dark matter self-interactions. *Mon. Not. Roy. Astron. Soc.*, 437(3):2865–2881, 2014.
- [13] Richard Massey, Thomas Kitching, and Johan Richard. The dark matter of gravitational lensing. *Rept. Prog. Phys.*, 73:086901, 2010.
- [14] G. Hinshaw et al. Nine-Year Wilkinson Microwave Anisotropy Probe (WMAP) Observations: Cosmological Parameter Results. *Astrophys.J.Suppl.*, 208, 2013.
- [15] P. A. R. Ade et al. Planck 2015 results. XIII. Cosmological parameters. *Astron. Astrophys.*, 594:A13, 2016.
- [16] P. A. R. Ade et al. Planck 2013 results. I. Overview of products and scientific results. *Astron. Astrophys.*, 571:A1, 2014.
- [17] Andrew R. Liddle. An Introduction to cosmological inflation. In *Proceedings, Summer School in High-energy physics and cosmology: Trieste, Italy, June 29-July 17, 1998*, pages 260–295, 1999.
- [18] Fabio Iocco, Gianpiero Mangano, Gennaro Miele, Ofelia Pisanti, and Pasquale D. Serpico. Primordial Nucleosynthesis: from precision cosmology to fundamental physics. *Phys. Rept.*, 472:1–76, 2009.
- [19] Volker Springel, Carlos S. Frenk, and Simon D. M. White. The large-scale structure of the Universe. *Nature*, 440:1137, 2006.
- [20] C. Alcock et al. The MACHO project: Microlensing results from 5.7 years of LMC observations. *Astrophys. J.*, 542:281–307, 2000.
- [21] R. D. Peccei and Helen R. Quinn. CP Conservation in the Presence of Instantons. *Phys. Rev. Lett.*, 38:1440–1443, 1977.
- [22] K. N. Abazajian et al. Light Sterile Neutrinos: A White Paper. 2012.
- [23] Gerard Jungman, Marc Kamionkowski, and Kim Griest. Supersymmetric dark matter. *Phys. Rept.*, 267:195–373, 1996.
- [24] Oskar Klein. Quantum Theory and Five-Dimensional Theory of Relativity. (In German and English). *Z. Phys.*, 37:895–906, 1926. [Surveys High Energ. Phys.5,241(1986)].
- [25] Graciela Gelmini and Paolo Gondolo. DM Production Mechanisms. 2010.
- [26] Jan Conrad. Indirect Detection of WIMP Dark Matter: a compact review. In *Interplay between Particle and Astroparticle physics (IPA2014) London, United Kingdom, August 18-22, 2014*, 2014.
- [27] Patrick J. Fox, Roni Harnik, Joachim Kopp, and Yuhsin Tsai. Missing Energy Signatures of Dark Matter at the LHC. *Phys. Rev.*, D85:056011, 2012.

- [28] Farinaldo S. Queiroz. Dark Matter Overview: Collider, Direct and Indirect Detection Searches. 2016.
- [29] Riccardo Catena and Piero Ullio. A novel determination of the local dark matter density. *JCAP*, 1008:004, 2010.
- [30] Katherine Freese, Mariangela Lisanti, and Christopher Savage. Colloquium: Annual modulation of dark matter. *Rev. Mod. Phys.*, 85:1561–1581, 2013.
- [31] Anne M. Green. Astrophysical uncertainties on direct detection experiments. *Mod. Phys. Lett.*, A27:1230004, 2012.
- [32] J. D. Lewin and P. F. Smith. Review of mathematics, numerical factors, and corrections for dark matter experiments based on elastic nuclear recoil. *Astropart. Phys.*, 6:87–112, 1996.
- [33] R. Bernabei et al. Final model independent result of DAMA/LIBRA-phase1. *Eur. Phys. J.*, C73:2648, 2013.
- [34] G. Angloher et al. Results on light dark matter particles with a low-threshold CRESST-II detector. *Eur. Phys. J.*, C76(1):25, 2016.
- [35] R. Agnese et al. New Results from the Search for Low-Mass Weakly Interacting Massive Particles with the CDMS Low Ionization Threshold Experiment. *Phys. Rev. Lett.*, 116(7):071301, 2016.
- [36] D. S. Akerib et al. Results from a search for dark matter in the complete LUX exposure. 2016.
- [37] Andi Tan et al. Dark Matter Results from First 98.7 Days of Data from the PandaX-II Experiment. *Phys. Rev. Lett.*, 117(12):121303, 2016.
- [38] E. Aprile and others (XENON Collaboration). XENON100 Dark Matter Results from a Combination of 477 Live Days. 2016.
- [39] E. Aprile and others (XENON Collaboration). Search for Electronic Recoil Event Rate Modulation with 4 Years of XENON100 Data. *in progress*, 2017.
- [40] J. Angle et al. First Results from the XENON10 Dark Matter Experiment at the Gran Sasso National Laboratory. *Phys. Rev. Lett.*, 100:021303, Jan 2008.
- [41] E. Aprile et al. (XENON Collaboration). The XENON100 Dark Matter Experiment. *Astropart. Phys.*, 35:573–590, 2012.
- [42] E. Aprile et al. (XENON Collaboration). Physics reach of the XENON1T dark matter experiment. *Journal of Cosmology and Astroparticle Physics*, 2016, 2016.
- [43] E. Aprile and T. Doke. Liquid xenon detectors for particle physics and astrophysics. *Rev. Mod. Phys.*, 82:2053–2097, Jul 2010.

## Bibliography

---

- [44] Alain Lansiart, Alain Seigneur, Jean-Luc Moretti, and Jean-Pierre Morucci. Development research on a highly luminous condensed xenon scintillator. *Nuclear Instruments and Methods*, 135(1):47 – 52, 1976.
- [45] Guillaume Plante. *The XENON100 Dark Matter Experiment: Design, Construction, Calibration and 2010 Search Results with Improved Measurement of the Scintillation Response of Liquid Xenon to Low-Energy Nuclear Recoils*. PhD thesis, Columbia University, New York, 2012.
- [46] M. Ambrosio et al. Vertical muon intensity measured with macro at the gran sasso laboratory. *Phys. Rev. D*, 52:3793–3802, Oct 1995.
- [47] M. Yamashita, T. Doke, K. Kawasaki, J. Kikuchi, and S. Suzuki. Scintillation response of liquid xe surrounded by PTFE reflector for gamma rays. *Nuclear Instruments and Methods in Physics Research Section A: Accelerators, Spectrometers, Detectors and Associated Equipment*, 535(3):692 – 698, 2004.
- [48] George Bakale, Ulrich Sowada, and Werner F. Schmidt. Effect of an electric field on electron attachment to sulfur hexafluoride, nitrous oxide, and molecular oxygen in liquid argon and xenon. *The Journal of Physical Chemistry*, 80(23):2556–2559, 1976.
- [49] E. Aprile et al. (XENON Collaboration). Analysis of the XENON100 Dark Matter Search Data. *arXiv:1207.3458 [astro-ph.IM]*, 2012.
- [50] E. Aprile and others (XENON Collaboration). Dark Matter Results from 225 Live Days of XENON100 Data. *Phys. Rev. Lett.*, 109:181301, 2012.
- [51] E. Aprile and others (XENON Collaboration). First Axion Results from the XENON100 Experiment. *Phys. Rev.*, D90(6):062009, 2014.
- [52] E. Aprile and others (XENON Collaboration). Exclusion of Leptophilic Dark Matter Models using XENON100 Electronic Recoil Data. *Science*, 349(6250):851–854, 2015.
- [53] E. Aprile and others (XENON Collaboration). Lowering the radioactivity of the photomultiplier tubes for the XENON1T dark matter experiment. *Eur. Phys. J.*, C75(11):546, 2015.
- [54] E. Aprile and others (XENON Collaboration). Material radioassay and selection for the XENON1T dark matter experiment. *in prep.*, 2017.
- [55] E. Aprile and others (XENON Collaboration). Conceptual design and simulation of a water Cherenkov muon veto for the XENON1T experiment. *JINST*, 9:11006, 2014.
- [56] Constanze Hasterok. *in Preparation*. PhD thesis, University of Heidelberg.
- [57] E. Aprile and others (XENON Collaboration). Removing krypton from xenon by cryogenic distillation to the ppq level. 2016.

- [58] Laboratoire National Henri Becquerel. Recommended data of radionuclide, 2016.
- [59] J. Sulkimo et al. (GEANT4). Geant4-a simulation toolkit. *Nucl. Instrum. Methods Phys. Res. Sect. A*, 506, 2003.
- [60] S. A. Bruenner. Study of radon adsorption on activated carbon for a purification system in XENON1T. Master's thesis, University of Graz, 2013.
- [61] Marc Weber. *Gentle Neutron Signals and Noble Background in the XENON100 Dark Matter Search Experiment*. PhD thesis, University of Heidelberg, 2013.
- [62] Sebastian Lindemann. *Intrinsic  $^{85}\text{Kr}$  and  $^{222}\text{Rn}$  Backgrounds in the XENON Dark Matter Search*. PhD thesis, University of Heidelberg, 2013.
- [63] R. Wink et al. The miniaturized proportional counter HD-2(Fe)/(Si) for the GALLEX solar neutrino experiment. *Nucl. Instrum. Methods Phys. Res. Sect. A*, 329, 1993.
- [64] Natascha Margarita Rupp. On the detection of  $^{222}\text{Rn}$  with miniaturized proportional counters: background, sensitivity studies and results for XENON1T. Master's thesis, University of Heidelberg, 2015.
- [65] J. Kiko. Detector for  $^{222}\text{Rn}$  measurements in air at 1 mBq/m<sup>3</sup> level. *Nucl. Instrum. Methods A*, 460, 2001.
- [66] J. Porstendorfer P. Pagelkopf. Neutralisation rate and the fraction of the positive  $^{218}\text{Po}$ -clusters in air. *Atmospheric Environment*, 37, 2003.
- [67] Leander Fischer. Investigation of Material Coatings in order to Reduce the Emanation of Radon. Bachelor's Thesis, University of Heidelberg, 2016.
- [68] Tomasz Skwarnicki. *A study of the radiative CASCADE transitions between the Upsilon-Prime and Upsilon resonances*. PhD thesis, Cracow Instiute of Nuclear Physics, DESY, 1986.
- [69] F. Mamedov et al. Development of an ultra-sensitive radon detector for the SuperNEMO experiment. *JINST*, 6, 2011.
- [70] K. Abe et al. (XMASS Collaboration). Radon removal from gaseous xenon with activated charcoal. *Nuclear Instruments and Methods in Physics Research A*, 2012.
- [71] D. S. Akerib et al. Chromatographic separation of radioactive noble gases from xenon. 2016.
- [72] K. Abe et al. (XMASS Collaboration). XMASS detector. *Nucl. Instr. and Meth.*, 716, 2013.
- [73] Simon Stemmle. Untersuchung der Adsorption von Radon und Xenon an verschiedenen Adsorbensien. Bachelor's Thesis, University of Heidelberg, 2013.

## Bibliography

---

- [74] J. Klomfar O. Sifner. Thermodynamic Properties of Xenon from the Triple Point to 800 K with Pressures up to 350 MPa. *Journal of Physical and Chemical Reference Data*, 23, 1994.
- [75] L. Q. Lobo A. G. M. Ferreira. On the vapour pressure of radon. *J. Chem. Thermodynamics*, 39, 2007.
- [76] W. Wagner. New vapour pressure measurements for argon and nitrogen and a new method for establishing rational vapour pressure equations. *Cryogenics*, 13, 1973.
- [77] S. Bruenner, D. Cichon, S. Lindemann, T. Marrodn Undagoitia, and H. Simgen. Radon depletion in xenon boil-off gas. *Eur. Phys. J.*, C77(3):143, 2017.
- [78] Robert Whytlaw Gray and William Ramsay. Some physical properties of radium emanation. *J. Chem. Soc. Trans.*, 95:1073–1085, 1909.
- [79] Alois F. Kovarik Ph.D. D.Sc. On the behaviour of small quantities of radon at low temperatures and low pressures. *The London, Edinburgh, and Dublin Philosophical Magazine and Journal of Science*, 4(26):1262–1275, 1927.
- [80] L. Wertenstein. Vapour pressure and condensation of radon at low temperatures. *Proceedings of the Royal Society of London A: Mathematical, Physical and Engineering Sciences*, 150(870):395–410, 1935.
- [81] Daniel R. Stull. Inorganic compounds. *Industrial & Engineering Chemistry*, 39(4):540–550, 1947.
- [82] Gerald L. Pollack. Extension of the law of corresponding states to rare-gas solids. *Phys. Rev. A*, 2:38–42, 1970.
- [83] K. Abe et al. Distillation of Liquid Xenon to Remove Krypton. *arXiv:0809.4413v3 [physics.ins-det]*, 2009.
- [84] Wang et al. Zhou. Design and construction of a cryogenic distillation device for removal of krypton for liquid xenon dark matter detectors. *Rev. Sci. Instrum.*, 85, 2014.
- [85] E. Aprile and others (XENON Collaboration). Online  $^{222}\text{Rn}$  removal by cryogenic distillation in the XENON100 experiment. 2017.
- [86] Dominick Cichon. Identifying Rn-222 decay chain events in liquid xenon detectors. Master’s thesis, University of Heidelberg, 2015.
- [87] E. Aprile et al. (XENON Collaboration). XENON100 Internal Backgrounds. In Preparation.
- [88] E. Aprile et al. (XENON Collaboration). Results from a Calibration of XENON100 Using a Source of Dissolved Radon-220. *arXiv:1611.03585*, 2016.

- [89] A. Bradley et al. (LUX Collaboration). Radon-related Backgrounds in the LUX Dark Matter Search. *Physics Procedia*, 61, 2015.
- [90] Stephan Rosendahl. *Gas purification of the XENON dark matter search*. PhD thesis, University of Muenster, 2015.
- [91] Michael Murra. *in preparation*. PhD thesis, University of Muenster, 2017.
- [92] Veronica Pizzella. Purity control of the XENON1T gas inventory prior to initial filling and studies of mixing properties of impurities in gaseous xenon. Master's thesis, Universita di Roma, 2016.



## List of Figures

1.1.	Galaxy rotation curves . . . . .	2
1.2.	Gravitational lensing and dark matter . . . . .	3
1.3.	CMB temperature fluctuations . . . . .	4
1.4.	Direct detection strategies . . . . .	7
1.5.	Status of direct dark matter detection searches . . . . .	8
1.6.	TPC working principle . . . . .	10
1.7.	XENON100 TPC and shielding . . . . .	12
1.8.	XENON100 gas handling . . . . .	14
1.9.	Fiducialization and band separation . . . . .	15
1.10.	XENON100 dark matter results . . . . .	16
1.11.	XENON1T TPC . . . . .	18
1.12.	XENON1T experimental setup . . . . .	18
1.13.	XENON1T schematic drawing . . . . .	20
1.14.	Sensitivity of XENON1T/XENONnT . . . . .	22
2.1.	Radon decay chain . . . . .	24
2.2.	$^{220}\text{Rn}$ and $^{222}\text{Rn}$ induced background in XENON1T . . . . .	25
2.3.	XENON1T radon screening results . . . . .	26
2.4.	Schematics of radon monitor . . . . .	28
2.5.	Radon monitor $\alpha$ -spectrum . . . . .	30
2.6.	Radon monitor detection efficiency pressure dependence . . . . .	32
2.7.	Radon monitor detection efficiency versus polonium isotope ratio . . . . .	33
2.8.	Radon monitor sensitivity . . . . .	35
2.9.	XENON1T emanation measurement extraction ports . . . . .	36
2.10.	XENON1T emanation measurement radon monitor data . . . . .	39
2.11.	Schematics of a radon purification loop . . . . .	41
2.12.	Differential equation describing number of radon atoms in XENON1T . . . . .	42
2.13.	Impact of radon removal system in XENON1T . . . . .	44
2.14.	Saturation vapor pressures of xenon and radon . . . . .	46
3.1.	The HeXe cryostat . . . . .	49
3.2.	The HeXe gas system . . . . .	50
3.3.	HRadon enrichment for boil-off measurements . . . . .	51

3.4. Typical data of boil-off reduction run . . . . .	55
3.5. Constant reduction fit . . . . .	56
3.6. Boil-off reduction xe_run1 . . . . .	59
3.7. Boil-off reduction xe_run2 . . . . .	61
3.8. Boil-off reduction xe_run3 overview . . . . .	62
3.9. Boil-off reduction xe_run3 results . . . . .	63
3.10. Boil-off reduction xe_run4 overview . . . . .	65
3.11. Boil-off reduction xe_run4 result . . . . .	66
3.12. Boil-off reduction xe_run5 overview . . . . .	67
3.13. Boil-off reduction xe_run6 overview . . . . .	68
3.14. Boil-off reduction xe_run5 and xe_run6 . . . . .	69
3.15. Radon depletion in argon boil-off gas . . . . .	70
3.16. Vapor pressure of radon . . . . .	72
4.1. $\alpha$ -events in XENON100 before corrections . . . . .	76
4.2. $\alpha$ -events in XENON100 after corrections . . . . .	77
4.3. $^{222}\text{Rn}$ $\alpha$ selection . . . . .	78
4.4. BiPo-event characteristics . . . . .	80
4.5. Spatial distribution of $^{210}\text{Po}$ events . . . . .	81
4.6. $^{210}\text{Po}$ energy spectrum . . . . .	82
4.7. $^{210}\text{Po}$ evolution during distillation campaign . . . . .	83
4.8. Experimental setup for XENON100 radon distillation . . . . .	84
4.9. Picture of XENON100 experimental site during distillation campaign . . . . .	85
4.10. The O-ring auxiliary emanation source . . . . .	85
4.11. Evolution $^{222}\text{Rn}$ activity concentration during distillation campaign . . . . .	87
4.12. $\alpha$ -rate after opening o-ring source . . . . .	91
4.13. Rad7 monitoring of radon concentration in ambient air . . . . .	93
4.14. Correlation of radon concentrations in ambient air and in XENON100 . . . . .	95
4.15. Unconstrained fit to 2nd distillation run data . . . . .	98
4.16. $\chi^2$ -scan of unconstrained fit to 2nd distillation run data . . . . .	99
4.17. Constraint fit to 2nd distillation run data . . . . .	100
4.18. Fit results of 1st distillation run . . . . .	101
4.19. XENON1T radon removal system scenario 1 . . . . .	103
4.20. XENON1T radon removal system scenario 2 . . . . .	103
4.21. XENON1T radon removal system scenario 3 . . . . .	105
4.22. XENON1T radon removal system scenario 4 . . . . .	105
A.1. Mass spectrum of carrier gas from XENON1T emanation measurement .	111

## List of Tables

2.1.	XENON1T radon screening results . . . . .	27
2.2.	Fit results for the radon monitor $\alpha$ -spectrum . . . . .	31
2.3.	Detection efficiency of radon monitors . . . . .	32
2.4.	Overview of XENON1T emanation measurements . . . . .	38
2.5.	XENON1T radon emanation results . . . . .	40
3.1.	Overview HeXe measurements . . . . .	53
3.2.	Summary boil-off reduction results . . . . .	74
4.1.	$\alpha$ identification in XENON100 . . . . .	79
4.2.	$^{222}\text{Rn}$ activity concentration in XENON100 over time . . . . .	89
4.3.	$^{222}\text{Rn}$ reduction due to on-line radon removal in XENON100 . . . . .	90
4.4.	Correlation of radon concentrations in ambient air and in XENON100 . . . . .	95
4.5.	Unconstrained fit to 2nd distillation run data . . . . .	98
4.6.	Constraint fit to 2nd distillation run data . . . . .	100
4.7.	Fit results of 1st distillation run . . . . .	101
4.8.	Type I and type II emanation sources in XENON1T . . . . .	102



## Danksagung

Es ist nun schon ein ganze Weile her, dass ich zum ersten Mal das MPIK betreten habe. In einem von der Zugfahrt zerknittertem Hemd stand ich, die schwitzenden Hände kneidend, vor dem Büro von Prof. Dr. Manfred Lindner um für das XENON Projekt vorstellig zu werden. Nun, da ich die letzten Sätze meiner Doktorarbeit schreibe, möchte ich auf meine Zeit am MPIK zurückblicken und mich bei all jenen bedanken deren Hilfe und Beistand diese Arbeit erst möglich gemacht hat.

Dank sagen will ich Prof. Dr. Manfred Lindner, der mich nach erwähntem Vorstellungsgespräch in die XENON Gruppe aufgenommen und mir damit die Möglichkeit geboten hat in einem wunderbaren und fassettenreichen Experiment mitzuarbeiten. Ihm, wie auch Prof. Dr. Loredana Gastaldo möchte ich auch für die Begutachtung meiner Doktorarbeit meinen Dank aussprechen.

In besonderer Weise möchte ich mich bei Dr. Hardy Simgen bedanken. Mein gesamtes Doktorat über war er nicht nur mein Betreuer und direkter Ansprechpartner alle Radonfragen betreffend, sondern auch ein großartiger Kollege und eine unerwartete Insel des österreichischen Liedguts in Deutschland.

Ein großes Danke geht auch an Dr. Teresa Marrodán Undagoitia für ihre ungezwungene und motivierende Art die mich, ohne es zu merken, mitreißt und selbst zu unliebsamen Arbeiten anzutreiben vermag.

Dr. Sebastian Lindemann war ohne Zweifel der wichtigste Lehrmeister auf meinem Werdegang zum Experimentalphysiker und guter Freund. Ihm danke ich für unzählige Stunden des Diskutierens; ob im Labor oder auch beim Lauftraining zwischen MPIK und Königsstuhl wo sicher ein Gutteil dieser Arbeit entstanden ist.

*Haben Sie das LNGS schon bei Nacht gesehen? Haben Sie das schon erlebt?* Allen die die zahlreichen Nachtschichten im Rahmen dieser Arbeit mit mir überlebt haben möchte ich meinen Dank aussprechen. Insbesondere sei hier Michael Murra von der Uni Münster erwähnt, Leidensgenosse während der Radon-Destillations Kampagne. Vielen Dank an der Stelle aber auch an meine Kollegen Natascha Rupp, Ludwig Rauch, Dominick Cichon, Alex Fieguth, Dr. Jochen Schreiner und Dr. Hardy Simgen, die auch Destillations-Shiften übernommen haben.

Ein weiterer LNGS Nachschichtler, diesmal während der XENON1T Emanationsmessungen, war Dr. Guillaume Eurin. Lachend blicke ich eine 'The meaning of Life' Diskussion zurück. Geführt, völlig übermüdet, neben einem rote Stühle hassenden Radon Monitor in der Heidelberg-Moskau Hütte.

Auch die zeitintensiven 'Boil-off' Messungen wären ohne die Unterstützung von Kollegen nicht möglich gewesen. Hier möchte ich besonders Dominick Cichon nochmals danken für die erforderlichen Nachtwachen in der Sizintillatorhalle.

Ich habe es immer als Privileg angesehen, eng mit unseren Werkstätten und Technikern zusammen zu arbeiten. Zum einen gab und gibt es viele Dinge für mich zu lernen, zum anderen durfte ich großartige Kollegen kennenlernen. Besonders bedanken möchte ich mich dabei bei Michael Reißfelder und Jonas Westermann, die mich auch nach Italien begleitet haben für Orbitalschweiß-Lektionen und Emanationsmessungen. Vielen Dank auch an Reinhard Hofacker für seine elektronische Unterstützung, insbesondere bei den Vorbereitungen der 'Boil-off'-Messungen, und Steffen Form der unzählige Male meine Signal-Verstärkerboxen reparieren musste.

Viele Kollegen und Freunde haben zum Gelingen dieser Arbeit beigesteuert auch wenn wir nicht täglich im Labor zusammenstanden. Besonders danken möchte ich hier Constanze Hasterok und Ludwig Rauch, (ehemaligen) Bürokollegen und beständige Diskussionspartner in ziemlich allen Belangen. Vielen Dank auch an Natascha Rupp, Veronica Pizzella, Luisa Hötzsch, Oliver Wack und Florian Jörg aus der XENON-Gruppe und Victoria Wagner und Julia Haser. Ihr alle seid mitverantwortlich, dass mir meine Doktorats-Zeit am MPIK in großartiger Erinnerung bleibt.

Den größten Dank möchte ich meiner Familie aussprechen; insbesondere meinen Eltern Roswitha und Augustin. Ohne eure beständige und bedingungslose Unterstützung jeglicher Art wäre mein gesamter Werdegang nicht denkbar.

Heidelberg, 07.04.2017

Stefan A. Brünner



